Results and Discussion

Chapter 4

4. Results and Discussion

4.1. Chemistry involved in the synthesis of the first series of compounds

A novel synthetic route towards developing **FA** derivatives has been optimized, as shown in schemes 1 and 2. In scheme 1 (page # 55), we developed a novel method for the synthesis of 2-amino-N-phenyl substituted acetamides (**3a**-**3q** and **6a**-**6b**) from 2-chloro-N-phenyl substituted acetamides (**2a**-**2q**) which are the key intermediates for the target compounds (**4a**-**4q** and **7a**-**7b**). In our initial attempts, the reaction between glycine and substituted aniline in organic solvents did not work well due to the poor solubility of glycine. So, we switched to the conversion of substituted amines into the corresponding 2-chloro-N-phenyl substituted acetamides followed by reflux with aqueous ammonia. Commercially available substituted anilines **1a**-**1q**, 5-aminoindole**,** and 6-aminoquinoline underwent a nucleophilic acyl substitution reaction with chloroacetylchloride in dichloromethane and K_2CO_3 as a base to give 2-chloro-N-phenyl substituted acetamides **2a**-**2q,** and **5a**-**5b**. The synthesis of 2-amino-N-phenyl substituted acetamides **3a**-**3q,** and **6a**-**6b** using *tert*-butyloxycarbonyl (BOC)-protected glycine has been reported in the literature.[155-158] However, these methods are not viable due to the limited commercial availability of the BOC-protected substrates, the requirement of functional group transformations with several reagents and solvents. Therefore, we developed direct and efficient routes towards the synthesis of 2-amino-N-phenyl substituted acetamide derivatives **3a**-**3q** and **6a**-**6b** under mild conditions in environmentally friendly aqueous media in a single step with good-to-high yields. 2-chloro-N-phenyl substituted acetamides **2a**-**2q,** and **5a**-**5b** were refluxed at 60°C in aqueous ammonia (NH_3) to afford precursor 2-amino-*N*-phenyl substituted acetamides **3a**-**3q** and **6a**-**6b** in good-to-excellent yields without purification. Finally, the target compounds **4a**-**4q** and **7a**-**7b** were generated using a standard amide coupling reaction of the 2-amino-*N*-phenyl substituted acetamide with ferulic acid in high yield.

Next, in scheme 3 (page # 56), we introduced a piperazine moiety in order to impart rigidity and provide a site for protonation to help improve the solubility and ability to cross the blood-brain barrier (BBB). The arylamines, **8a-8g,** underwent a nucleophilic substitution reaction (S_N2) with bis(2-chloroethyl) amine hydrochloride to give the substituted phenyl piperazines **9a-9g**, following the literature method, [159] which were further reacted with ferulic acid to afford the target compounds **10a-10g**. The structures of the synthesized molecules were confirmed with the help of ^{1}H-NMR, ^{13}C-NMR, and high-resolution mass spectrometry.

4.2. Biological evaluation of the first series of compounds

4.2.1. *In-vitro* cholinesterases inhibition (AChE, and BChE) studies

The deficiency of brain acetylcholine (ACh) and other related neurotransmitters is one of the major factors in the progression of AD. Clinically, it is well explored that cholinesterase inhibitors are effective in improving behavior and slowing down cognitive decline in patients with AD [160]. Thus, the inhibitory activity of the newly synthesized compounds against human AChE and *equine* BChE was measured by using the spectroscopic method of Ellman *et al*. [161] and expressed as IC_{50}, *i.e.*, the inhibitor concentration that reduces the cholinesterase activity by 50%. In this study, DPZ served as the reference drug, and **FA** was used as the negative control.

The crystal structure analysis of AChE revealed the location of the active site at the bottom of a deep and 20 Å long narrow gorge. The choline part of the substrate, ACh, binds into the anionic subsite of the active site surrounded by Trp86, Tyr337, and Phe338 while the esteric moiety interacts with the catalytic triad composed of Ser203, Glu334, and His447of the esteratic site. A docking study with the R enantiomer of DPZ on AChE (PDB ID: #4EY7) was carried out, as shown in figure 4.1. The binding mode analysis of DPZ involves residues that span the length of the active site gorge and multiple key interactions with critical residues thought to be important in the enzyme mechanism. The benzyl ring stacks against Trp86 in the active site while the indanone ring formsπ-π interactions with Trp286 in the peripheral anionic site. The carbonyl group of DPZ binds with Phe295 while the piperidine nitrogen makes hydrogen bonding to Trp86, Tyr337, and Phe338.

It is evident from the literature that **FA** is a poor inhibitor of AChE. We carried out molecular docking studies followed by AChE inhibition studies for **FA** and compared the results with those for the reference drug DPZ. As expected, in both the studies **FA** exhibited significantly poorer interactions compared to DPZ (IC_{50}, μM = 0.03 ± 0.007 for DPZ, and 15.19 ± 0.59% inhibition of AChE at 20 μM for **FA**). Given the nature of the long active site of AChE and the relatively short structure of **FA**, it was expected that docking studies would be helpful for predicting which structural modifications should be carried out to improve the binding of **FA** to AChE. The overlay of docked DPZ and co-crystallized DPZ are shown in figure 4.2. It demonstrates that the docking method works well because of the close agreement between the two poses of DPZ. Interestingly, the docking studies of **FA** (Figure 4.1B) with AChE revealed that the majority of the interactions with the critical amino acids are missing as compared to DPZ (Figure 4.1A). It is noteworthy that the presence of acid and phenol functional groups in **FA** provides scope for possible structural modifications to develop novel analogs. Two of the major goals behind our design of the novel **FA** analogs were to improve the AChE inhibition and improve the clogP values in this first generation of **FA**-derived compounds. The structural modifications are centered on the acid functional group of **FA**.

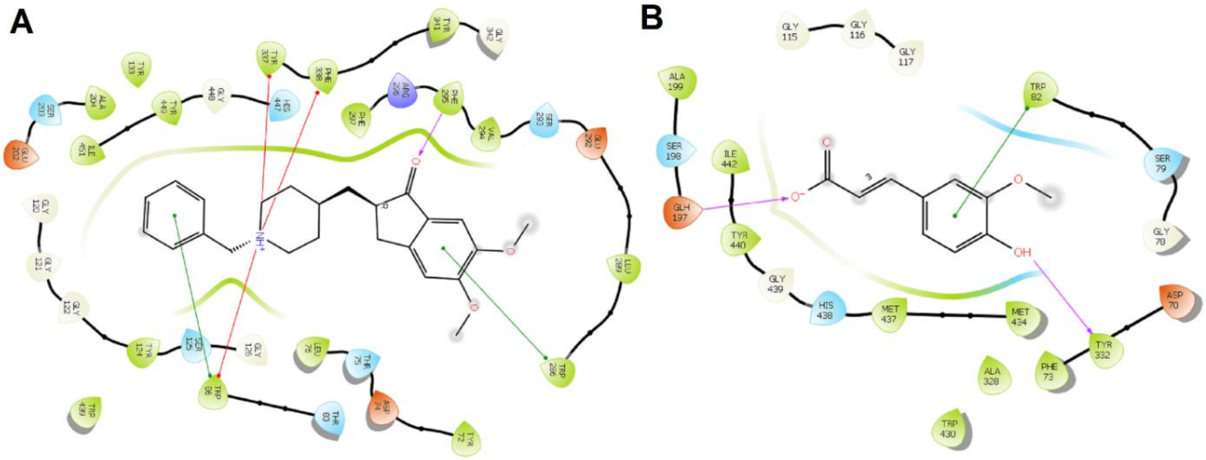

Figure 4.1. 2D interaction diagram of (**A**) DPZ and (**B**) **FA** with various amino acids of the AChE (PDB ID: #4EY7) cavity.

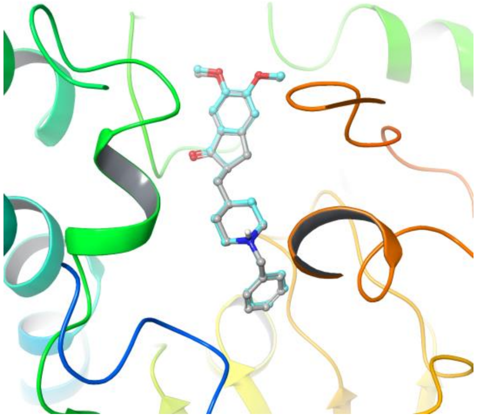

Figure 4.2. Overlay of docked donepezil and co-crystallized DPZ.

We started with the introduction of an amide linker followed by aromatic features into the designed molecules, as shown in figure 4.3 to reach the active site of the enzymes. The aromatic features also improved the lipophilicity and helped the analogs to be able to interact with the essential hydrophobic residues. The presence of an amide bond near the aromatic substitutions on the right-hand side of the molecule could allow H-bonding with Phe295.

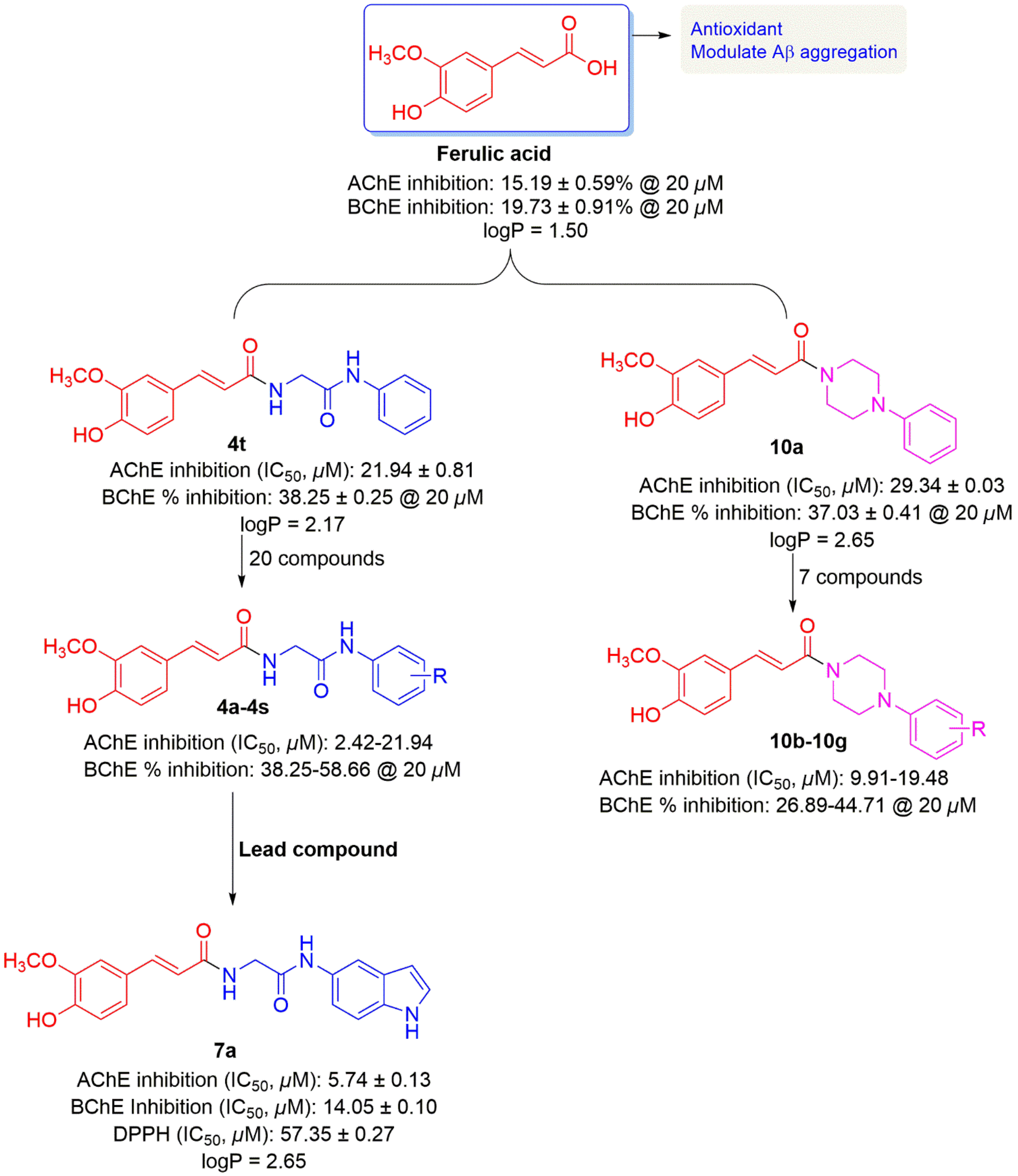

Figure 4.3. Schematic pipeline toward the development of novel ferulic acid derivatives with favorable properties.

Our first goal was to find out if the peripheral phenyl ring could be tolerated at the enzyme sites. Therefore, compound **4a** was designed, synthesized, and evaluated for enzyme inhibition.

Interstingly, in the enzyme inhibition studies, **4a** was found to be a potent inhibitor of AChE. The significant improvement in AChE inhibition as compared to **FA** was observed (**4a**, IC_{50} = 21.94 ± 0.81 μM for AChE, while **FA** exhibited only 19.73 ± 0.91% inhibition of AChE at 20 μM) as shown in Table 4.1. This result indicated that novel amide compounds with aromatic features are well tolerated on the enzyme sites. Further, the methyl group was introduced at various positions of the phenyl ring located on the right-hand side of the molecule. Compounds **4b-4d** were designed, synthesized, and evaluated for enzyme inhibition. In the AChE inhibition assay, **4d** bearing a methyl group in the *p*-position of the phenyl ring turned out to be the most potent in comparison to the *ortho*-or *meta*-substituted compounds **4b** and **4c** (IC_{50}, AChE, 16.27 ± 0.62, 18.9 ± 0.17, and 12.62 ± 0.05 μM for **4b**, **4c,** and **4d**, respectively) (Table 4.1). Interestingly, **4d** was found to be approximately 1.5 times more potent compared to unsubstituted **4a** ($IC_{50,}$ AChE (μM) 21.94 ± 0.81 vs. 12.62 ± 0.05 for **4a** and **4d**, respectively). However, in the BChE inhibition assay, no such significant difference in the enzyme inhibition was observed among the compounds developed so far (% inhibition at 20 μM 36.82 ± 1.10, 36.12 ± 0.22, 35.60 ± 0.84 and 38.25 ± 0.25 for **4b**, **4c**, **4d,** and **4a**, respectively). It is noteworthy that **4b** and **4a** are twice as potent in BChE inhibition compared to **FA** (BChE inhibition at 20 μM = 19.73 ± 0.91 for **FA**).

For the next set of compounds, monomethoxy or monochloro functional groups were introduced at various positions of the distal phenyl ring of the earlier developed **4a**, which led to the generation of **4e-4g**, and **4h-4j**, respectively. Interestingly, compounds **4f** and **4j** showed the maximum inhibition for AChE among all the synthesized derivatives of this class (IC_{50}, AChE (μM)**, 4f** = 2.42 ± 0.32, **4j** = 3.43 ± 0.03, BChE (μM), **4f** = 15.29 ± 0.14, **4j** = 19.54 ± 0.01, respectively) (Table 4.1). This result may suggest that the introduction of electron-withdrawing groups on the phenyl ring at the *para*-position or electron-donating groups at the *meta*-position could improve

AChE and BChE inhibition. This may be due to strong hydrogen bonding with Tyr124 and Arg296, and aromatic-π interaction with Tyr337 and Phe338 of **4f** (Figure 4.4A and Figure 4.4B). We further introduced electron-withdrawing groups on various positions of the terminal phenyl ring to find out the role played by electronic features on the inhibition of the enzymes. The introduction of *o*-CF_3, *m*-CF_3, and *p*-CF_3 led to development of compounds **4k-4m** with IC_{50}, AChE (μM), **4k** = 15.15 ± 0.31, **4l** = 9.31 ± 0.03, **4m** = 8.23 ± 0.12, (Table 4.1). These results suggested that the introduction of electron-withdrawing groups on the phenyl ring could significantly improve the AChE inhibitory activity compared to **FA**. However, in the BChE inhibition assay, no such significant difference was observed among the developed compounds (% inhibition at 20 μM 43.22 ± 0.10, 34.92 ± 0.05, and 37.25 ± 0.07 for **4k-4m**, respectively).

Finally, the introduction of small and large electron-withdrawing groups onto the phenyl ring to explore the combined effect of electronic and steric features was carried out. This modification produced compounds **4n-4q**, bearing *m*-nitrile, *p*-nitrile, *p*-fluoro, and *p*-bromo, at the indicated positions of the terminal phenyl ring. Interestingly, the enzyme inhibition studies indicated the small EWG on the phenyl ring did not have much influence on AChE and BChE inhibitory properties (IC_{50}, AChE (μM), 16.01 ± 0.35, 17.43 ± 0.07, 12.93 ± 0.40, and 10.24 ± 0.14; % inhibition, BChE, 31.58 ± 0.69, 35.67 ± 0.27, 42.25 ± 0.56, and 39.28 ± 0.14 for **4n-4q**, respectively).

The next goal of our study was to replace the aromatic phenyl ring with the heterocyclic moieties with an aim to introduce additional aromatic feature for aromatic-π interactions (indole or quinolone) in order to improve potency and target selectivity. This modification resulted in the synthesis of compounds **7a** and **7b** with IC_{50}, AChE (μM) 5.74 ± 0.13 and 4.89 ± 0.37, for **7a** and **7b,** respectively. The enhanced inhibition may be due to the aromatic-π interaction with Trp286 and Tyr341, and hydrogen bonding with Asp74 and Tyr337 in the case of **7a** (Figure 4.4C & Figure 4.4D). To our surprise, the docking studies exposed two different binding modes of **7a**, as shown in figure 4.5). Pose 1 had the indole ring pointed towards PAS, while Pose 2 had the indole ring shifted towards the active site of substrate AChE. Pose 1 showed higher docking and binding scores and therefore used this docked pose for molecular dynamics (MD) simulations in order to explore further the interactions with the protein.

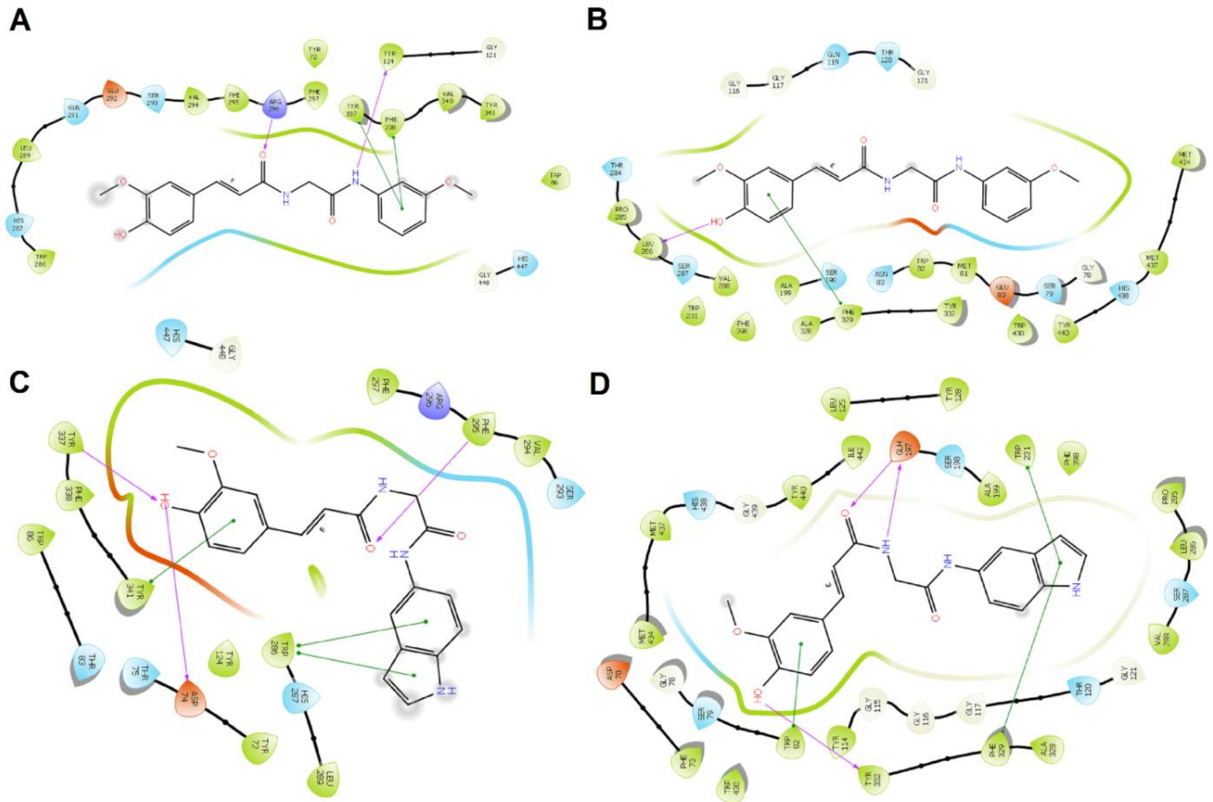

Figure 4.4. 2D interaction diagram of (**A**) **4f** with AChE (PDB #4EY7); (**B**) **4f** with BChE (PDB #4BDS); (**C**) **7a** with AChE; and (**D**) **7a** with BChE.

Introducing a heterocyclic nucleus (indole or quinoline) displayed a better BChE inhibitory activity with IC_{50} (μM), BChE, 14.05 ± 0.10, 14.32 ± 0.04, for **7a** and **7b,** respectively). These results indicated that introducing the indole or quinoline functionalities in place of the simple phenyl ring is well tolerated and could modulate the selectivity towards the target to a significant extent. In our next series of compounds, a piperazine moiety was introduced to impart rigidity and provide a site for protonation to help improve BBB penetration and solubility. Our enzyme inhibition studies with **4a**-**4q** demonstrated that compounds having *m*-methoxy, *p*-chloro, fluoro, or methyl substitutes are comparatively potent enzyme inhibitors over the other developed **FA** analogs.

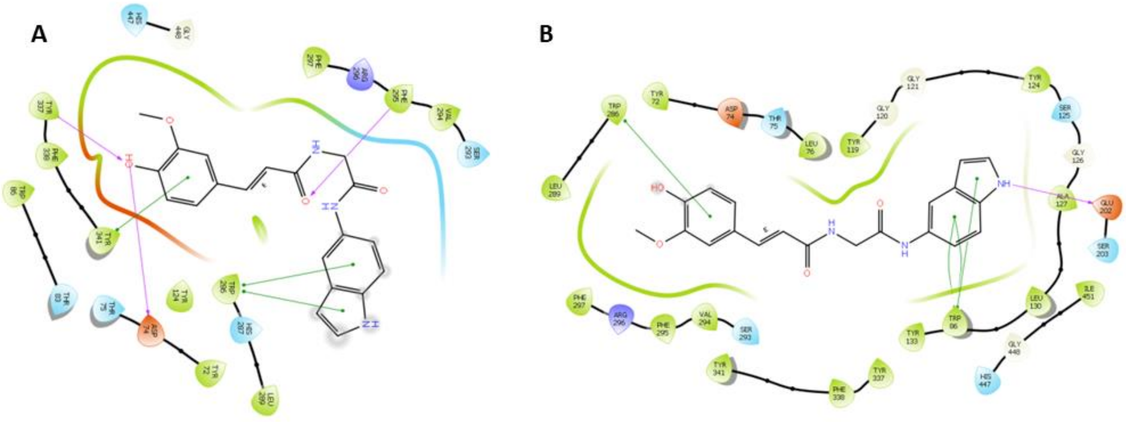

Figure 4.5. Binding interactions (2D) of **7a (A)** Pose I and **(B)** Pose II with various amino acids of AChE active cavity (two different binding modes).

We specifically incorporated these groups in the development of piperazine-bearing molecules **10a-10g** to investigate the impact of these substitutes on enzymes inhibition. To our surprise, the introduction of the piperazine ring in place of glycine amide to connect the **FA** moiety and phenyl ring apparently led to a mixed impact on the enzyme's inhibition potencies. All the developed molecules were found to be moderate to weak inhibitors of the target enzymes compared to the other structural analogs reported in this work (Table 4.1). Intriguingly, a significant reduction in the enzyme inhibition activities was found in the case of *m*-methoxy or *p*-chloro derivatives, **10b** or **10f** compared to **4f** or **4j** (IC_{50}, AChE (μM), 9.91 ± 0.07, 11.15 ± 0.13 for **10b** and **10f** and BChE inhibition (in %) 26.89 ± 0.20, 33.24 ± 1.56 for **10b** and **10f**, respectively). An increase in AChE inhibition and decrease in BChE inhibition activities were observed in *p*-fluoro or methoxy analogs (IC_{50}, AChE (μM) 11.04 ± 0.06, 12.05 ±1.14 for **10c** and **10e**, % BChE inhibition 26.89 ± 0.20, 33.24 ± 1.56 for **10b** and **10f**, respectively). This may be due to the complex interaction of these molecules with the enzymes. Binding interactions (2D diagram) of **10b** with amino acid residues of the AChE active cavity are shown in figure 4.6. The SAR on this series has been summarized in figure 4.7.

Table 4.1. Cholinesterase inhibitory activities of the target compounds.

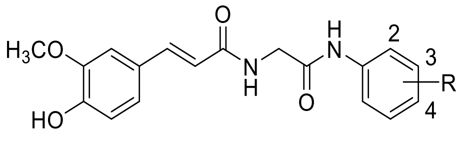

4a-4q

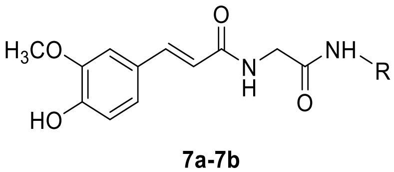

7a-7b

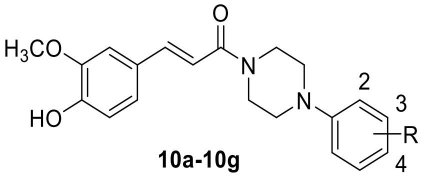

10a-10g

Compd	**R**	hAChE IC_{50}^{a} (μM)	*eq*BChE	
			% inhibition	IC_{50}^{a} (μM)
4a	Hydrogen	21.94 ± 0.81	38.25 ± 0.25	nd
4b	2-methyl	16.27±0.62	36.82 ± 1.10	nd
4c	3-methyl	18.91 ± 0.17	36.12 ± 0.22	nd
4d	4-methyl	12.62 ± 0.05	35.60 ± 0.84	nd
4e	2-methoxy	5.75 ± 0.24	43.33 ± 1.37	nd
4f	3-methoxy	2.42 ± 0.32	55.38 ± 0.17	15.29 ± 0.14
4g	4-methoxy	17.29 ± 0.07	49.85 ± 0.06	19.54 ± 0.01
4h	2-chloro	5.72 ± 0.03	47.36 ± 0.33	nd
4i	3-chloro	5.68 ± 0.04	48.54 ± 1.29	nd
4j	4-chloro	3.43 ± 0.03	46.85 ± 0.14	nd
4k	2-trifluoro	15.15 ± 0.30	43.22 ± 0.10	nd
4l	3-trifluoro	9.31 ± 0.03	34.92 ± 0.05	nd
4m	4-trifluoro	8.23 ± 0.12	37.25 ± 0.07	nd
4n	3-cyano	16.01 ± 0.35	31.58 ± 0.69	nd
4o	4-cyano	17.43 ± 0.07	35.67 ± 0.27	nd
4p	4-fluoro	12.93 ± 0.40	42.25 ± 0.56	nd
4q	4-bromo	10.24 ± 0.14	39.28 ± 0.14	nd
7a	5-aminoindolyl	5.74 ± 0.13	58.66 ± 0.17	14.05 ± 0.10
7b	6-aminoquinolinyl	4.89 ± 0.37	57.73 ± 0.21	14.32 ± 0.04
10a	Hydrogen	29.34 ± 0.03	37.03 ± 0.41	nd
10b	3-methoxy	9.91 ± 0.07	26.89 ± 0.20	nd

10c	4-fluoro	11.04 ± 0.06	27.66 ± 0.39	nd
10d	3-nitro	23.43 ± 1.98	37.92 ± 0.57	nd
10e	4-methoxy	12.05 ± 1.14	44.71 ± 0.05	nd
10f	4-chloro	11.15 ± 0.13	33.24 ± 1.56	nd
10g	4-methyl	19.48 ± 0.12	38.14 ± 0.12	nd
FA[c]	-----	n.a.	19.73 ± 0.91	nd
DPZ[d]	-----	0.03 ± 0.007	65.68 ± 0.01	2.89 ± 0.02

[a] IC_{50} = 50% inhibitory concentration (means ± SD of 2 to 3 independent experiments)

[b] Inhibition was determined at 20μM inhibitor concentration (in triplicate)

[c] **FA** (Ferulic acid) = used as negative control

[d] **DPZ** (Donepezil) = used as positive control

n.a.: less than 10% inhibition at 20μM

nd: not determined

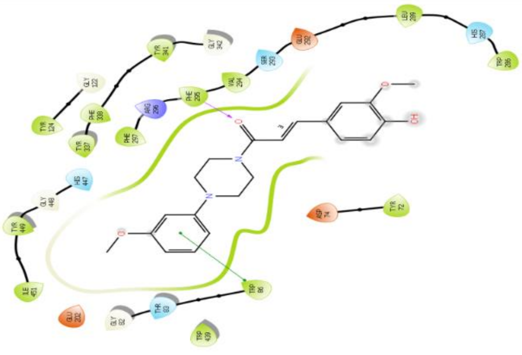

Figure 4.6. Binding interactions (2D) of **10b** with various amino acids of AChE active cavity.

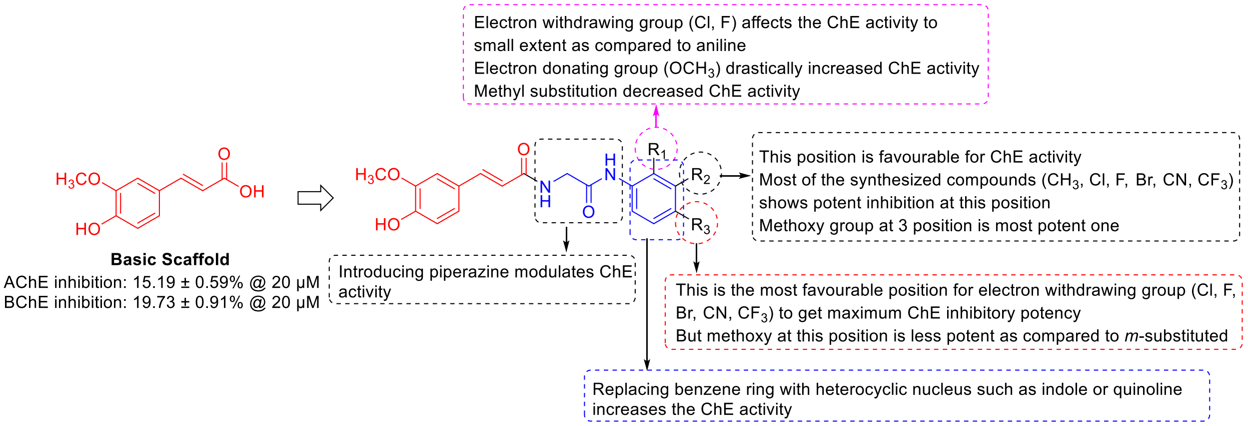

Electron withdrawing group (Cl, F) affects the ChE activity to small extent as compared to aniline
Electron donating group (OCH_3) drastically increased ChE activity
Methyl substitution decreased ChE activity

This position is favourable for ChE activity
Most of the synthesized compounds (CH_3, Cl, F, Br, CN, CF_3) shows potent inhibition at this position
Methoxy group at 3 position is most potent one

Basic Scaffold
AChE inhibition: 15.19 ± 0.59% @ 20 μM
BChE inhibition: 19.73 ± 0.91% @ 20 μM

Introducing piperazine modulates ChE activity

This is the most favourable position for electron withdrawing group (Cl, F, Br, CN, CF_3) to get maximum ChE inhibitory potency
But methoxy at this position is less potent as compared to *m*-substituted

Replacing benzene ring with heterocyclic nucleus such as indole or quinoline increases the ChE activity

Figure 4.7. Structural optimization and a summary of SAR with **FA** analogs.

4.2.2. Evaluation of antioxidant activity

Oxidative stress plays a major role in the progression of AD by the generation of excess reactive oxygen species (ROS), which impair multiple cellular functions, including causing loss of synaptic activity and finally can lead to neurodegeneration. Thus, reducing oxidative stress is an important aspect of designing a new drug candidate for AD. **FA** probably exerts its antioxidant effect through free radical scavenging activity by transferring a hydrogen atom to its substrate [162]. The molecules exhibiting promising cholinergic inhibition were subjected to this study. The antioxidant property of the synthesized molecules **4f**, **4g**, **4i**, **4j**, **7a**, **7b,** and **10b** was evaluated by the 2,2-diphenyl-1-picrylhydrazyl (DPPH) method and compared with that of the parent molecule **FA**. Antioxidant activity is expressed as IC_{50} value, defined as the concentration of an antioxidant species required to reduce 50% of the DPPH radical concentration in a solution. All tested compounds demonstrated moderate antioxidant activity compared to **FA** (Figure 4.8, Table 4.2).

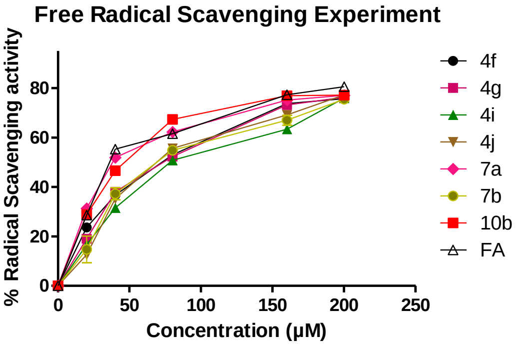

Figure 4.8. Percent radical scavenging activity of **4f**, **4g**, **4i**, **4j**, **7a**, **7b**, **10b,** and **FA**. Each point represents a value from the experiment done in triplicate and is expressed as the mean ± SEM.

We hypothesize that loss in the free radical quenching ability of the majority of the developed molecules compared to **FA** is probably due to the absence of the free acid functional group. Notably, we could compensate for this loss in the antioxidant property of developed analogs in the indole-bearing molecule **7a** and the piperazine derivative **10b**. The proposed mechanism for free radical quenching is shown in figure 4.9. The free acid group on **FA** was found to be crucial to the radical scavenging ability. The compounds **7a** and **10b** presented moderate antioxidant activity, with IC_{50} of 57.35 ± 0.27 and 61.98 ± 0.30 μM, respectively (Table 4.2).

Table 4.2. Antioxidant activity (DPPH assay) of **4f**, **4g**, **4i**, **4j**, **7a, 7b, 10b,** and **FA**.

	Antioxidant activity (DPPH assay)	
Compd	% Radical scavenging[a]	IC_{50}[b] (μM)
4f	19.06 ± 0.20	94.29 ± 0.19
4g	23.64 ± 0.07	91.24 ± 0.61
4i	12.66 ± 0.92	107.73 ± 0.93
4j	16.66 ± 0.08	101.21 ± 0.85
7a	31.33 ± 0.14	57.35 ± 0.27
7b	18.59 ± 0.12	77.61 ± 0.58
10b	28.82 ± 0.18	61.98 ± 0.30
FA[c]	28.56 ± 0.02	56.49 ± 0.62
AA	66.12 ± 0.13	-------

[a] All the values were obtained at a compound concentration of 20 μM.

[b] IC_{50}: 50% inhibitory concentration (mean ± SD of three experiments).

[c] **FA** (ferulic acid) = used as a negative control.

[d] **AA** (Ascorbic acid) = reference compound [215].

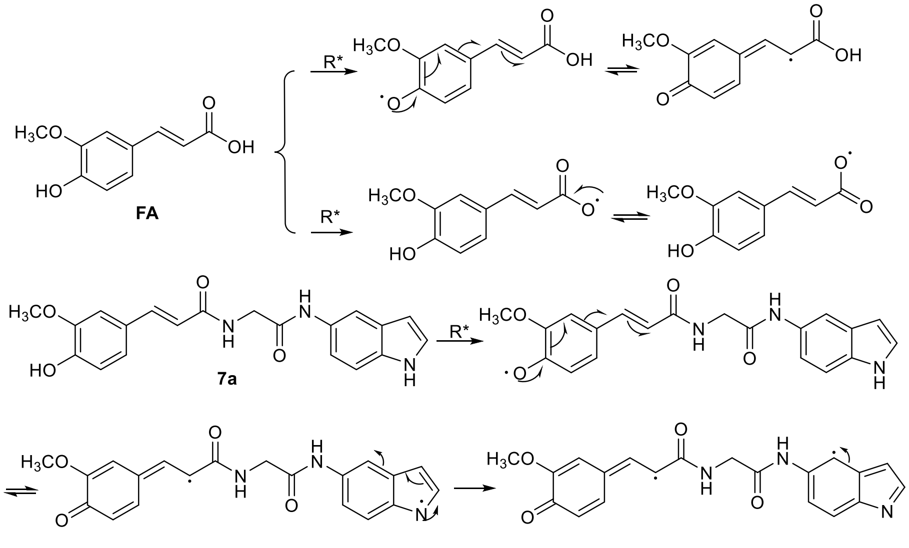

Figure 4.9. Proposed mechanism of **FA** and **7a** radical scavenging activity.

4.2.3. *In*-vitro cholinesterases (AChE, and BChE) inhibition kinetic studies with the lead molecule

On the basis of ChE inhibitory studies, lead compound **7a** was selected for AChE and BChE inhibition kinetics studies. Three fixed concentrations of inhibitor **7a** were selected for this study, and for each concentration, the velocity [V] of the substrate hydrolysis was measured at six different substrate [S] concentrations. For each inhibitor concentration, the reciprocal of the initial velocity (1/[V]) was plotted with respect to the reciprocal of the substrate concentration (1/[S]). As described in figure 4.10A and 4.10B, the double reciprocal (Lineweaver–Burk) plot showed a non-competitive inhibition pattern for compound **7a** in the case of AChE, and mixed type inhibition in the case of BChE.

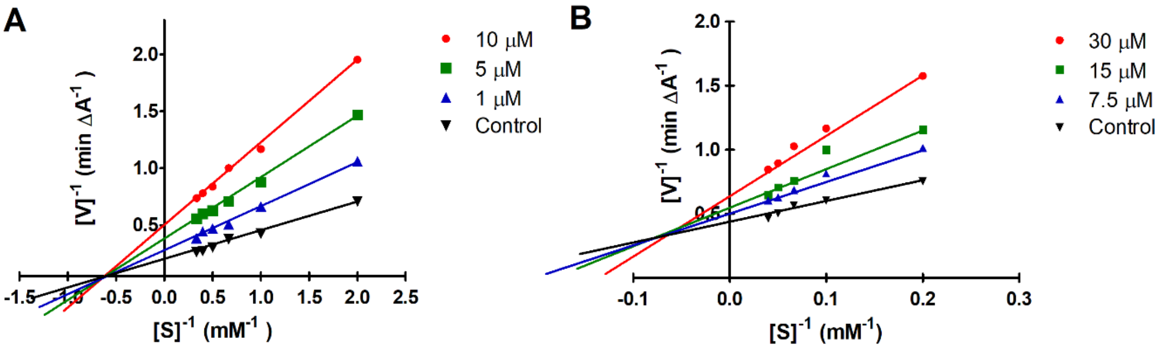

Figure 4.10. Kinetics study on the mechanism of ChE inhibition by compound **7a**. (**A**) Overlaid Lineweaver–Burk reciprocal plots based on the *h*AChE initial velocity at increasing substrate concentration (0.5-3.0 mM) in the absence or presence of **7a** (1, 5, and 10 μM) are shown. [S] = concentration of acetylthiocholine; [V] = initial velocity rate. (**B**) Merged Lineweaver–Burk reciprocal plots of *eq*BChE initial velocity with increasing substrate concentration (5, 10, 15, 20 and 25 mM) in the absence or presence of **7a** (7.5, 15 and 30 μM) [S] = concentration of butyrylthiocholine; [V] = initial velocity rate. Lines were derived from a weighted least-squares analysis of data points. The experimental data are the means ± SD of two independent experiments.

4.2.4. Measurement of propidium iodide displacement from the peripheral anionic site (PAS) of AChE

Enzyme kinetics study indicated that **7a** is a noncompetitive inhibitor of *h*AChE. To further gain insight and to assess whether **7a** has an affinity towards the PAS of AChE, a propidium iodide displacement assay was designed and performed. Propidium iodide is a specific ligand for the peripheral site of AChE that exhibits a 10-fold higher fluorescence when bound to AChE [163]. The decrease in the propidium iodide fluorescence in the presence of **7a** can be interpreted as propidium displacement from the PAS. DPZ, the marketed drug for AD, which is known to bind to the PAS site of the enzyme, served as a reference drug in this assay. The results obtained in this study clearly indicated that compound **7a** could effectively displace propidium iodide (9.06% to 28.53%) in comparison to **FA** 0.12 to 8.65% (Table 4.3). The reference drug DPZ gave 10.14% to 30.88% of propidium iodide displacement in this assay.

Table 4.3. Displacement of propidium iodide from the peripheral anionic site of AChE by **7a**, **FA** and DPZ at the indicated concentrations.

Compd	5 μM	10 μM	20 μM	50 μM
7a	9.06 ± 0.16	11.78 ± 2.17	18.47 ± 0.55	28.53 ± 0.18
FA	0.12 ± 0.35	2.22 ± 0.37	5.10 ± 0.19	8.65 ± 0.25
DPZ	10.14 ± 0.24	13.95 ± 0.25	21.65 ± 0.35	30.88 ± 0.53

[a] Results are the mean ± SEM for two independent experiments.

4.2.5. Evaluation of iron chelation of novel compounds

Oxidative stress, metal dyshomeostasis, and aging are presumably the common factors that play a major role in the onset of AD. It has been shown in the literature that metal-derived ROS, especially those from iron and copper, are the major culprits responsible for the inhibition of mitochondrial respiration and the promotion of Aβ aggregation in the form of intracellular neurofibrillary plaques and tangles [49]. Given the fact that metals play a critical role in AD, metal chelating therapy is under investigation to see if it can be used to develop disease-modifying agents [52]. Therefore, the most potent compounds **4f** and **7a** were investigated for their chelating metal property by UV-vis spectroscopy with wavelengths ranging from 200 to 700 nm. In figure 4.11A and figure 4.11B, UV-vis spectra of **7a** and **4f** with increasing Fe^{3+}concentration are shown. The absorbance peaks of **7a** and **4f** shifted from 306.5 to 446 nm, and in case of **4f** new peaks were observed at 454 and 620.5 nm, respectively. The increased absorbance indicated that there was an interaction between Fe^{3+} and compounds **4f** and **7a.**

To further confirm the complex formation, MS-MS analysis of the solutions used in the UV analysis was carried out. As shown in figure 4.11C, the presence of molecular ion peaks corresponding to **7a**−Fe^{3+} (m/z = 420.35 and 421.23) demonstrated the metal chelating ability of **7a**. Interestingly, the appearance of peaks at m/z = 411.35 and 413.25 in the MS-MS spectrum of **4f**−Fe^{3+} indicated the interaction of **4f** with Fe^{3+} (Figure 4.11D). These results supported the pH-dependent UV-vis spectroscopy metal complexation study.

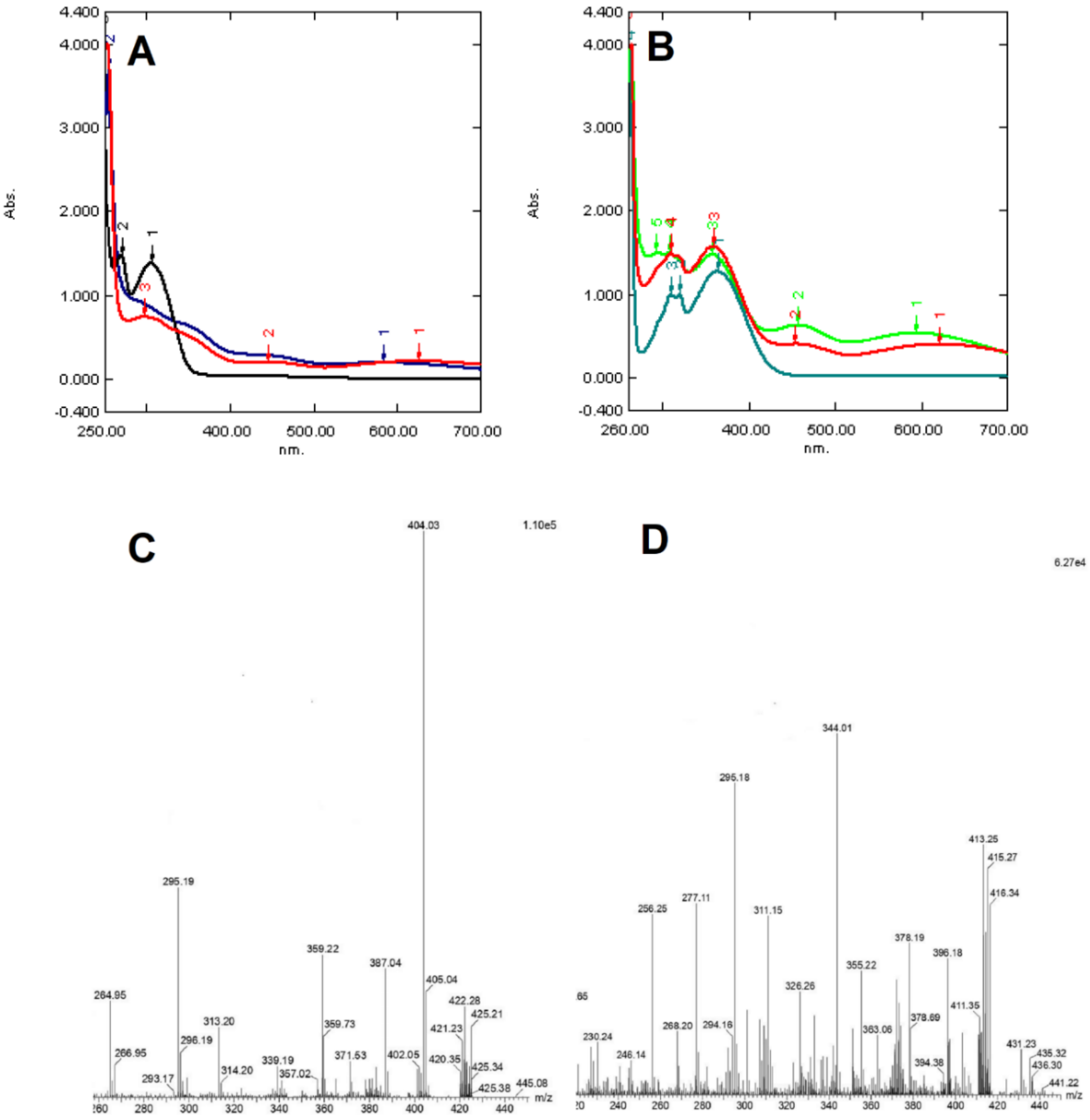

Figure 4.11. UV absorbance spectrum of compounds **7a** and **4f** alone and in the presence of $FeCl_3$ in water at various pH. (**A**) **7a** alone (300 μM) (black), **7a** (600 μM) + $FeCl_3$ (600 μM) at pH 4.2 (red) and **7a** (600 μM) + $FeCl_3$ (600 μM) at pH 7.4 (blue). (**B**) **4f** (300 μM) (dark gray), **4f** (600 μM) + $FeCl_3$ (600 μM) at pH 4.2 (red) and **4f** (600 μM) + $FeCl_3$ (600 μM) at pH 7.4 (green). (**C**) Molecular ion peaks of complex formed from **7a** and $FeCl_3$ at pH 7.4. Peaks at m/z 420.35 and 421.23 correspond to **7a**–Fe^{3+} complex with 1:1 stoichiometry. (**D**) Molecular ion peaks of complexes formed from **4f** and $FeCl_3$ at pH 7.4. Peaks at m/z 411.35 and 413.25 correspond to **4f**–Fe^{3+} complex with 1:1 stoichiometry.

4.2.6. Evaluation of Aβ_{1-42} aggregation modulation activity of the lead molecule

AD is mainly associated with the deposition of self-aggregating Aβ peptide. The accumulation of Aβ_{1-42} induces the formation of toxic Aβ oligomers and fibrils, which cause the impairment of synapses and neurons [164]. Aβ_{1-42} aggregates were generated with a goal to evaluate the effect of the lead molecule on the aggregation process. In this experiment, Aβ_{1-42} aggregates were formed to yield aggregated structures that were detected by atomic force microscopy (AFM). To achieve this, we incubated Aβ_{1-42} (0.39 μM) with mechanical shaking for 20 days. The main objective of this experiment was to find out the time point at which Aβ_{1-42} monomers get converted into aggregated structures. The AFM image analysis (Figure 4.12C and 4.12D) revealed the aggregates generated at 10 days had clearly formed fibril structures and were different from the samples on day 20 (Figure 4.12E and 4.12F). The control sample Aβ_{1-42} (0.39 μM) at 10 days showed the presence of fibril structures bigger in size compared to protein alone at t = 0 (Figure 4.12A and 4.12B), and only a few characteristic monomer structures were observed in the sample of Aβ_{1-42}. We selected 10 days time point as the incubation time for further studies. Based on the enzyme inhibition studies and antioxidant property evaluation, **7a** was chosen as the lead molecule to monitor the Aβ_{1-42} aggregation modulation property. The reference drug DPZ and **FA** were also incubated with Aβ_{1-42} for comparison. AFM images demonstrated the absence of a significant amount of fibril Aβ samples incubated in the presence of **7a** (Figure 4.12G and 4.12H) and **FA** (Figure 4.12I and 4.12J). Aβ_{1-42} incubated in the presence of DPZ exhibited distinct morphology (Figure 4.12K and 4.12L) compared to **7a** or **FA**-treated samples. These results indicate the potential interaction between **7a** and Aβ_{1-42}, which would thereby modulate the formation of Aβ_{1-42} aggregates. The reference drug DPZ failed to confer significant structural changes in the aggregated form of Aβ_{1-42}, compared to **7a** or **FA**.

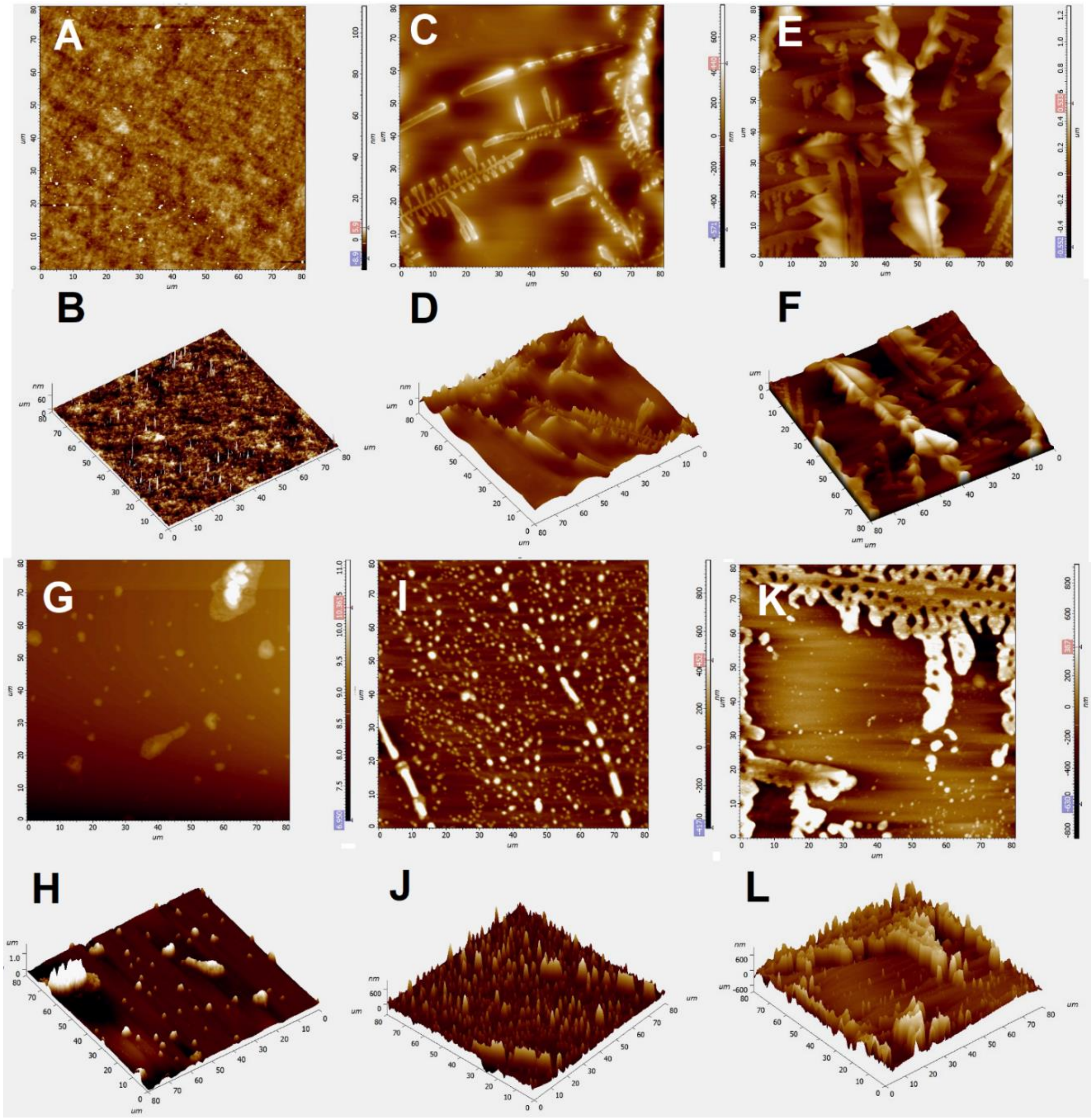

Figure 4.12. Inhibition of self-induced $A\beta_{1-42}$ aggregation in the presence of **7a, FA,** and DPZ. (AFM images). (**A** and **B**) Fresh $A\beta_{1-42}$ at t = 0 time point (0.39 μM). (**C** and **D**) $A\beta_{1-42}$ alone (0.39 μM) after 10 days of shaking at 37 °C. (**E** and **F**) $A\beta_{1-42}$ alone (0.39 μM) after 20 days of shaking at 37 °C. (**G** and **H**) $A\beta_{1-42}$(0.79 μM) + **7a** (1.58 μM) after 10 days of shaking at 37 °C. (**I** and **J**) $A\beta_{1-42}$ (0.79 μM) + **FA** (1.58 μM) after 10 days of shaking at 37 °C. (**K** and **L**) $A\beta_{1-42}$ (0.79 μM) + **7a** (1.58 μM) after 10 days of shaking at 37°C.

4.2.7. Molecular docking study with AChE and BChE

To investigate the binding mode of the compounds with their AChE (PDB ID: 4EY7) and BChE (PDB ID: 4BDS), molecular docking of the most potent compounds **4f** and **7a** was performed using the Schrödinger software. As mentioned in figure 4.4 (page # 65), compound **4f** formed two hydrogen bonds with Tyr124, Arg296, and two π-π stacks with Tyr337 and Phe338, resulting in its good inhibitory activity against AChE. However, in the case of BChE, **4f** formed only one hydrogen bond and one π-π stack with Leu286 and Phe329. This might be the reason for the reduced potency of **4f** against BChE (Figure 4.4B). As depicted in figure 4.4C, in the case of **7a,** we observed binding at both the enzymatic catalytic active site (CAS) with Asp74, Tyr337, and Tyr341 and at the PAS with Trp286 and Phe295. This means that replacing the phenyl with indole could intensify AChE inhibitory activity. Further, in the case of BChE, **7a** formed three π-π stacks with Trp82, Trp321, Phe329, and hydrogen bonds with Glu197 and Tyr332 (Figure 4.4D**)**.

The double reciprocal plot (Lineweaver–Burk) of enzyme kinetic inhibition showed a non-competitive inhibition pattern for compound **7a.** So, we aligned the X-ray crystal structure of mouse acetylcholinesterase complex with acetylcholine (PDB ID: 2HA4) (% identity with 4EY7 = 87 and % similarity = 92) and our docked complex of **7a** with AChE, manually shifted acetylcholine to the **7a**-AChE complex, and energy minimized the complex using the Prime minimization module of Schrödinger [165]. Interestingly, we found that acetylcholine can still be accommodated in the active site of AChE in the presence of **7a** (Figure 4.13A), which supports the non-competitive inhibition nature of **7a**. In addition, we also overlaid the docked pose of **7a** with DPZ, the co-crystalized ligand in the X-ray crystal structure of 4EY7, and found that the **7a** indole moiety slightly shifted towards the PAS site, but most of the remaining part of **7a** overlapped with the DPZ pose (Figure 4.13B). Our finding matches well with the results of the propidium iodide displacement assay in which **7a** displaced propidium iodide from the peripheral anionic site (PAS) of AChE (cf. section on measurement of propidium iodide displacement from the peripheral anionic site (PAS) of AChE).

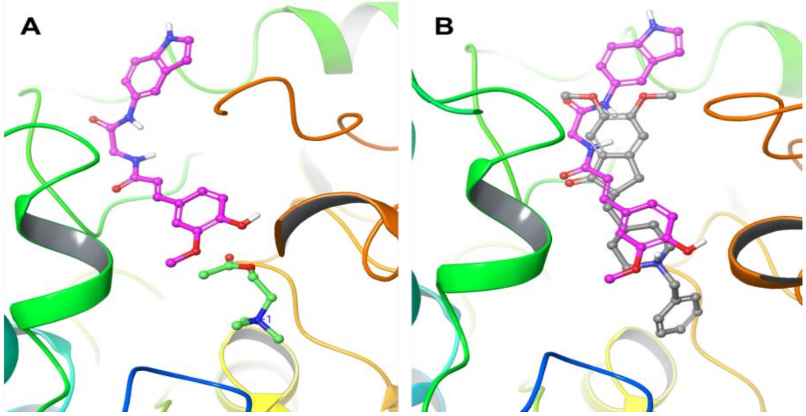

Figure 4.13. (**A**) Docked the pose of **7a** (C in magenta) and acetylcholine (C in green) into the active site of AChE. (**B**) Overlaid docked pose of **7a** (C in magenta) and DPZ (C in grey) into the active site of AChE.

4.2.8. Molecular dynamics (MD) simulations studies with AChE

In an effort to gain a better understanding of the interaction profile and mode of interactions between **7a** with AChE, we proceeded to do molecular dynamics (MD) simulations. MD is an important computational tool to check the thermodynamic stability of docked compounds [166]. We have selected the best-docked ligand (based on docking score) **7a** for the MD simulations. The MD simulations were performed for 30 ns, and the overall stability of the simulation was evaluated using the root mean square deviations (RMSD) of the backbone atoms, which ranged from 0.2 to 1.7 Å (Figure 4.14A). The graph suggests that the RMSD of the protein backbone is stable over the period of the MD simulation and attains equilibrium within 5 ns.

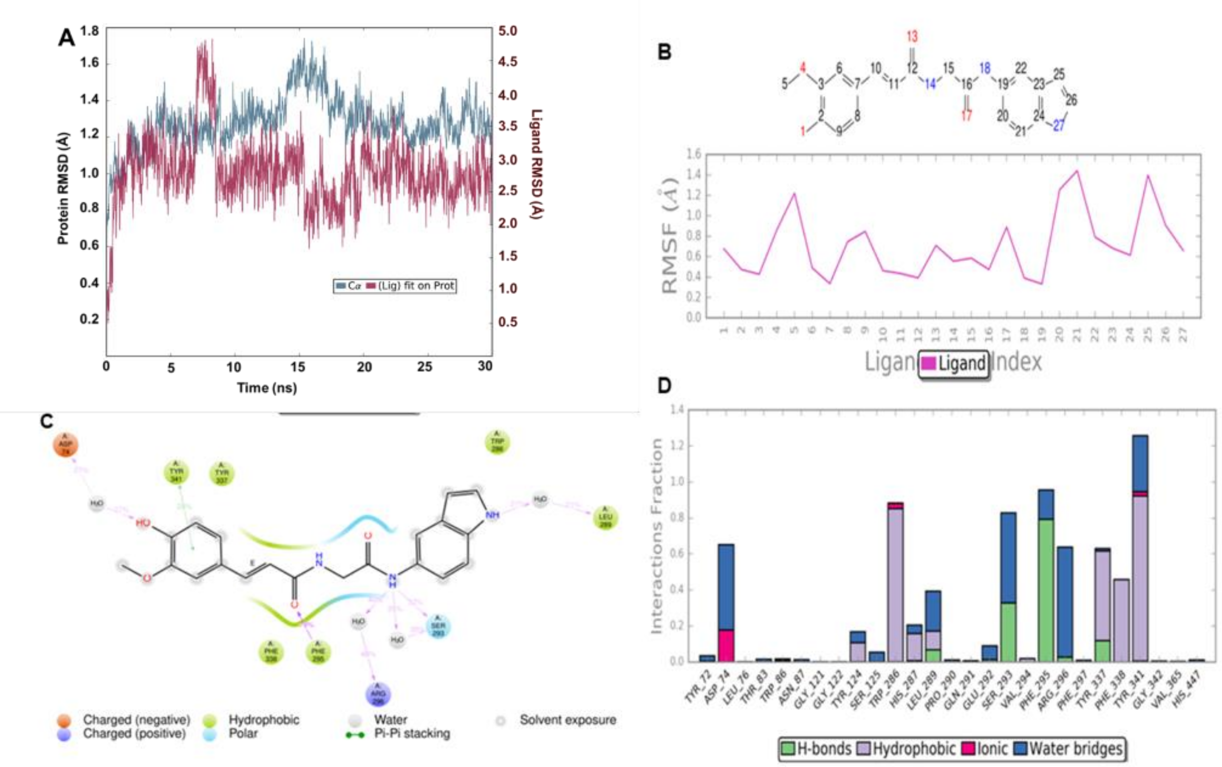

Figure 4.14. (**A**) Protein-ligand RMSD. RMSD protein (left Y-axis); the ligand RMSD (right Y-axis) indicates the stability of ligand 7a with respect to the protein and its active pocket. (**B**) Ligand Root Mean Square Fluctuation (L-RMSF). (**C**) A schematic of detailed 7a atom interactions with the key amino acid residues. **(**D**)** Bar charts of protein interaction with ligand 7a as monitored throughout the simulation (Green- H-bonding; Gray-Hydrophobic; Blue- Water bridges; Pink-Ionic interactions).

The ligand root means square fluctuation **(L-RMSF)** profile indicated ligand fragments interact with the protein and play an entropic role in the binding event (Figure 4.14B). In the graphical snapshot of the binding pattern shown in Figure 4.14C, the amide (NH), ferulic acid (OH), and indole (NH) of compound **7a** interact with water molecules, playing a crucial role in the formation of hydrogen bonds with the amino acid residues Arg296, Ser293, Asp74, and Leu289. The stacked bar diagram indicates the normal interactions over the course of the MD simulations (Figure 4.14D). The stacked bar chart showed four types of ligand-protein interactions, including H-bonding, hydrophobic interactions, ionic, and water bridge.

4.2.9. Molecular dynamics (MD) simulation studies with BChE

Since compound **7a** is active against both AChE and BChE, therefore, we also performed a 30 ns simulation for **7a** with the BChE complex. We used similar settings and protocols for the MD simulation as we used for **7a** with the AChE complex.

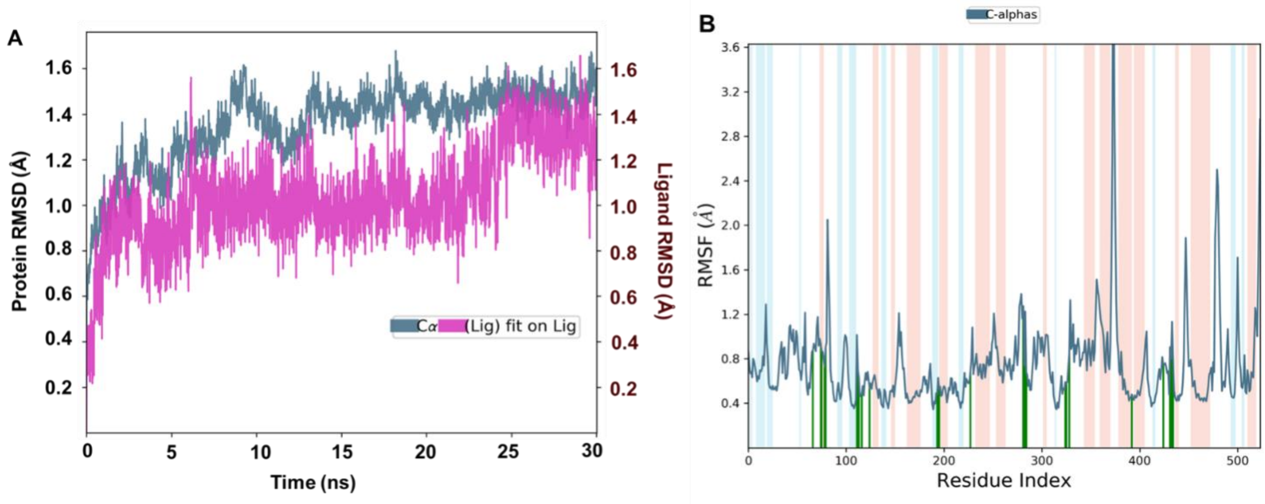

Figure 4.15. (**A**) Protein RMSD (left Y-axis) and ligand RMSD (right Y-axis) indicate the stability of ligand **7a** with respect to BChE and its active pocket. (**B**) RMSF plot based on Cα atoms of BChE for the BChE–**7a** complex. Protein residues that interact with **7a** are marked with green vertical bars. Alpha-helical and beta-strand regions are highlighted in pink and blue backgrounds, respectively.

The RMSD plot of atom location vs. simulation time (Figure 4.15A) indicated that the protein (BChE) and **7a** attained a significantly stable state that was well maintained throughout the final 20 ns of the simulations. The RMSF plot (Figure 4.15B) based on Cα atoms of BChE also showed very low fluctuation in the residues that form the ligand-binding site. The simulation interaction histogram (Figure 4.16) and 2D contact map (Figure 4.17) showed that Gly115, Tyr128 (water-mediated H-bonding, ~60% contributions), Glu197 (H-bonding with carbonyl, 62% contribution), Trp231 (π-π stacking with indole moiety, 41% contribution), Leu286 (H-bonding with indole N-

H, 74% contribution), Ala328 (H-bonding with phenolic hydroxyl, 81% contribution), and Phe329 (π-π stacking with indole moiety, 95% contribution) were the key residues for interactions with **7a** during the course of the simulation. Overall, **7a** maintained strong and stable interactions with BChE during the 30 ns of MD simulation.

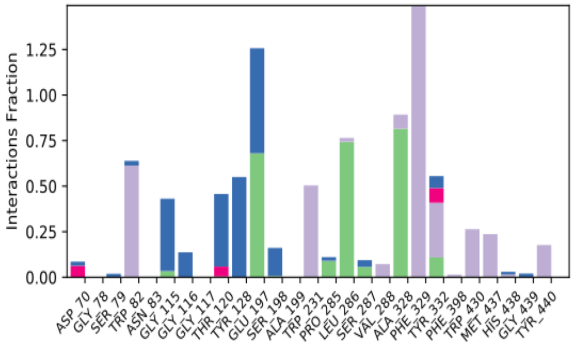

Figure 4.16. The SID plot showing the protein-ligand interactions between the amino acid residues of the BChE binding site and **7a**. The stacked bar charts are categorized as follows: hydrogen bonding (green), hydrophobic interactions (violet), water bridges formed (blue), and ionic interactions (pink).

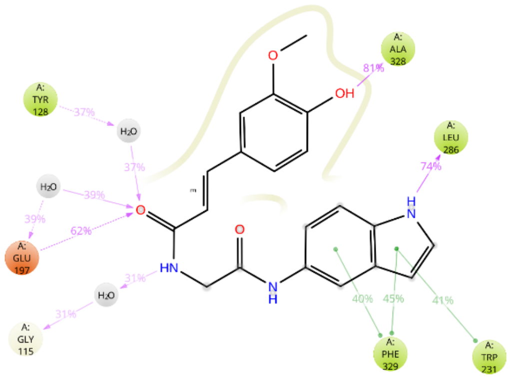

Figure 4.17. Binding interactions (2D) of **7a** with various amino acids of BChE (PDB ID: 4BDS) active site.

4.2.10. Calculation of physicochemical parameters

We used admetSAR and ChemDraw Professional 15.0 software to assess whether our synthesized series of compounds possess the correct parameters to exhibit drug-likeness or not. Compounds that fail the drug-likeness criteria tend not meet the requirements to be an effective clinical candidate due to excessive toxicity, poor bioavailability, or other concerns [167]. We used admetSAR server to predict molecular descriptors such as lipophilicity (LogP), topological polar surface area (TPSA), molecular weight (MW), number of hydrogen bond donors (HBD) and hydrogen bond acceptors(HBA), number of rotatable bonds (RB), blood-brain barrier permeability (BBB) and Caco2 permeability (Table 4.4). According to Lipinski's Rule of Five, a compound is said to be membrane permeable if it matches the following criteria: (a) lipophilicity≤5, (b) molecular weight<500, (c) HBD ≤5 (OH and NH groups), (d) HBA ≤10 (N and O atoms). Compounds violating more than one of these rules could have problems related to bioavailability. All the synthesized compounds follow Lipinski's rule and exhibited significant brain permeability (Table 4.4).

Table 4.4. Theoretical prediction of physiochemical parameters of the developed compounds.

Comp.	Mol.Wt.[†]	logP[a]	TPSA[b]	HBA[c]	HBD[d]	RBs[e]	BBB[f]	Caco-2
4a	326.35	2.17	87.66	4	3	6	+	-
4b	340.38	2.48	87.66	4	3	6	+	-
4c	340.38	2.48	87.66	4	3	6	+	-
4d	340.38	2.48	87.66	4	3	6	+	-
4e	356.38	2.18	96.89	5	3	7	+	-
4f	356.38	2.18	96.89	5	3	7	+	-
4g	356.38	2.18	96.89	5	3	7	+	-
4h	360.79	2.82	87.66	4	3	6	+	-
4i	360.79	2.82	87.66	5	3	7	+	-
4j	360.79	2.82	87.66	5	3	7	+	-
4k	394.11	3.19	87.66	4	3	6	+	-
4l	394.35	3.19	87.66	4	3	6	+	-
4m	394.35	3.19	87.66	4	3	6	+	-

4n	351.36	2.04	111.45	5	3	6	+	-
4o	351.36	2.04	111.45	5	3	6	+	-
4p	344.34	2.31	87.66	4	3	6	+	-
4q	404.25	2.93	87.66	4	3	6	+	-
7a	365.39	2.65	99.69	4	4	6	+	-
7b	377.40	2.72	100.02	5	3	6	+	-
10a	338.41	2.76	53.01	4	1	4	+	+
10b	368.43	2.77	62.24	5	1	5	+	-
10c	356.40	2.90	53.01	4	1	4	+	-
10d	383.40	2.67	104.82	6	1	5	+	-
10e	368.43	2.77	62.24	5	1	5	+	-
10f	372.85	3.62	53.0	5	1	4	+	-
10g	352.43	3.39	53.0	5	1	4	+	-
FA	194.19	1.50	66.76	3	2	3	+	-
DNP	379.50	4.36	111.45	4	0	6	+	+

All values were calculated using online software admetSARexcept TPSA(ChemDraw).

[†]Daltons, [a]Calculated logarithm of the octanol-water partition coefficient, [b]Topological polar surface area, [c]Hydrogen-bond acceptor, [d]Hydrogen-bond donor, [e]Rotatable bonds, [f]Blood brain barrier.

4.2.11. Evaluation of cytotoxicity of the lead molecule

The cytocompatibility, which is one of the important factors in the drug development process, was evaluated using the 3-(4,5-dimethylthiazol-2-yl)-2,5-diphenyltetrazolium bromide (MTT) assay. The MTT assay is based on the reduction of MTT (yellow color) and other tetrazolium dyes and depends upon cellular metabolic activities due to NADPH dependent cellular oxidoreductase enzymes [168]. The healthy and fast-growing cells show increased reduction of MTT to formazan (purple color) and hence have higher absorbance, whereas the dead or inactive cells fail to do so.

The dose-dependent effect of **7a** on cell viability was carried out with SH-SY5Y cells, a widely used neuronal cell line. The cells were treated with different concentrations of **7a** and were quantitatively analyzed by the MTT-assay. As shown in figure 4.18, **7a** showed cytocompatibility with SH-SY5Y cells at all the tested concentrations. At the highest tested concentration of **7a** *i.e.*, 20 μM, 95.61% of cells were viable with 4.39% cytotoxicity as compared to control (100%) (Figure 4.18).

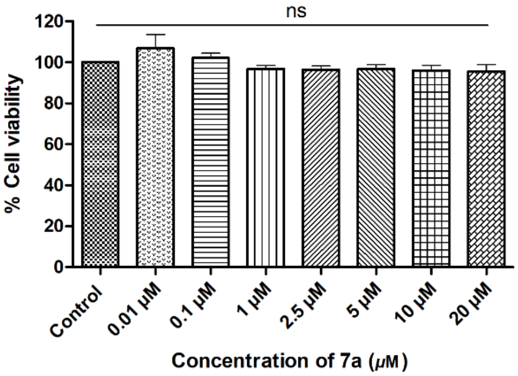

Figure 4.18. Effect of **7a** on cell viability. Cells were treated with different concentrations of **7a** (20, 10, 5, 2.5, 1, 0.1 and 0.01 μM) for 24 hours. Cell percent viability was analyzed using the MTT assay. Data are represented as mean ± SE of three independent experiments done in three replicates.

4.2.12. Neuroprotection studies with 7a (F24) on H_2O_2 induced cell death and morphological alterations

In this experiment, we have employed various concentrations (100 to 800 μM) of the pro-oxidant H_2O_2 (widely acceptable neurotoxin) and found that 600 μM of H_2O_2 can cause ~50 % cell death in SH-SY5Y cells (Figure 4.19A). To further investigate the effect of the duration of H_2O_2 treatment on cell viability, we further increased the treatment duration from 24 h to 48 h of the cells with H_2O_2. It is evident from figure 4.19B that the incubation of the cells for 24h, is toxic to producing close to 50% cell death. After optimizing the concentration of H_2O_2 and the incubation time, we next assessed the neuroprotection ability of **7a** (**F24)** and the reference drug (DPZ) to alter cytotoxicity after co-incubating with H_2O_2. The cells were incubated with various concentrations (1, 2.5, 5, 10, and 20 μM) of **7a** (**F24)** and DPZ for 24 h followed by co-treatment with 600 μM H_2O_2 for an additional 24 h. As shown in figure 4.19C, the MTT assay data indicated that both **7a** (**F24)** and DPZ could significantly ($P < 0.0001$) protect SH-SY5Y cells from H_2O_2 induced neurotoxicity. The significant protection conferred by **7a** and DPZ was exhibited in all tested concentration ranges of 1−20 μM of the drugs. The lower concentrations (1 to 5 μM) were found to be slightly more effective in providing the neuroprotection compared to the higher concentration (20 μM). H_2O_2 can directly react with Michael acceptor or other functional groups such as phenol present in the 7a, thereby, unable to produce the ROS.

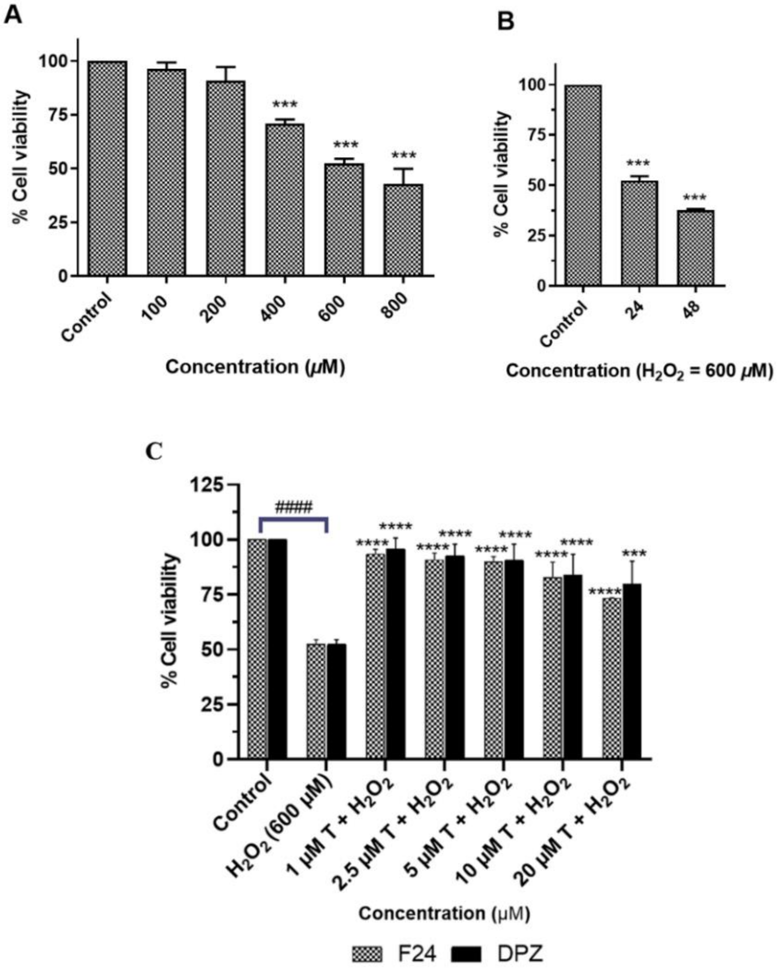

Figure 4.19. Effect of **7a** (**F24)** against H_2O_2 mediated cell death. (**A**) Cell death induced by H_2O_2 at 100, 200, 400, 600, and 800 μM for 24 h. (**B**) Cell death induced by 600 μM H_2O_2 for 24 h and

48 h. (**C**) Neuroprotective effect of treatment (**T**) **7a (F24)** or DPZ against H_2O_2 mediated SH-SY5Y cell death. Cells were pre-incubated with **7a (F24)** or DPZ at 1, 2.5, 5, 10, or 20 μM for 24 h and then further co-incubated with 600 μM H_2O_2 for another 24 h. Cell death was assessed by MTT assay. All values are represented as mean ± SD of at least three independent experiments. $^{***}P < 0.001$ and $^{****}P < 0.0001$ vs H_2O_2-treated group, $^{\#\#\#\#}P < 0.0001$ vs control group.

Based on the promising neuroprotection property conferred upon the pretreatment with **7a** (**F24**) against H_2O_2 induced neurotoxicity, we were next interested in observing the morphological alterations induced in SH-SY5Y cells upon the pretreatment with **7a** (**F24**). Therefore, the cells were seeded into a 96-well plate and preincubated with various concentrations of **7a** (**F24**) (1, 2.5, 5, 10, or 20 μM) for 24 h. After 24 h, the cells were co-treated with 600 μM of H_2O_2 for an additional 24 h, and the morphological alterations were studied under a live-cell imager fluorescence microscope. The results indicated that H_2O_2-treatment caused significant morphological alterations such as loss of adherence causing cells to float in the medium, the loss in their short, fine processes known as neuritis and became round in shape compared to the control (Figure 4.20A and 4.20B). In contrast, the cells pre-incubated with different concentrations of **7a** (**F24**) (Figure 4.20C-4.20G) followed by co-treatment with H_2O_2 showed no signs of morphological changes and appeared similar to control. This observation further supported that **7a** (**F24**) can strongly protect the neuronal cells from oxidative damage induced through H_2O_2.

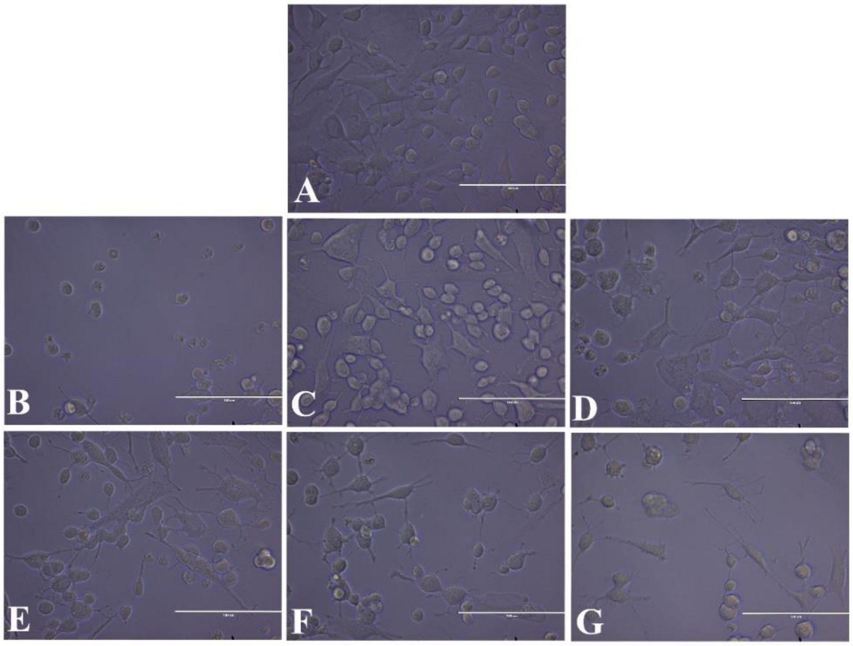

Figure 4.20. Representative images of SH-SY5Y cells morphological alterations induced by H_2O_2 and the effect of **7a (F24)**. (**A**) Control (**B**) H_2O_2 (600 μM) (**C**) H_2O_2 600 μM+ 1 μM of **7a** (**F24**) (**D**) H_2O_2 + 2.5 μM of **7a** (**F24**) (**E**) H_2O_2 + 5 μM of **7a** (**F24**) (**F**) H_2O_2 + 10 μM of **7a** (**F24**). (**G**) H_2O_2 + 20 μM of **7a** (**F24**). SH-SY5Y cells were preincubated with **7a** (**F24**) (1, 2.5, 5, 10, and 20 μM) for 24 h and exposed to 600 μM H_2O_2 for an additional 24 h. The cell morphology was observed using a phase-contrast microscope. The scale bar corresponds to 100 μm.

4.2.13. Intracellular ROS modulation studies with 7a (F24)

MitoSox is a well-explored mitochondria-targeted modified hydroethidine dye used for the detection of intracellular superoxide radical anion, which generate red flouroscent intermediate upon oxidation [169]. The oxidant species [170]. SH-SY5Y cells were pretreated with different concentrations of **7a** (**F24**) or DPZ for 24 h and later co-incubated with 600 μM H_2O_2 for another 24 h. A significant increase in ROS generation was observed following treatment of SH-SY5Y cells with 600 μM H_2O_2 alone compared to control (Figure 4.21). H_2O_2 treatment caused cytotoxicity to the cells by inducing oxidative stress, which resulted in ROS generation. However, the pretreatment of cells with 1 μM and 2.5 μM of **7a** caused a significant reduction of ROS generation (*P < 0.05 and **P < 0.01) in the cells, suggesting the protective effect of **7a** (**F24**) against oxidative stress in cells.

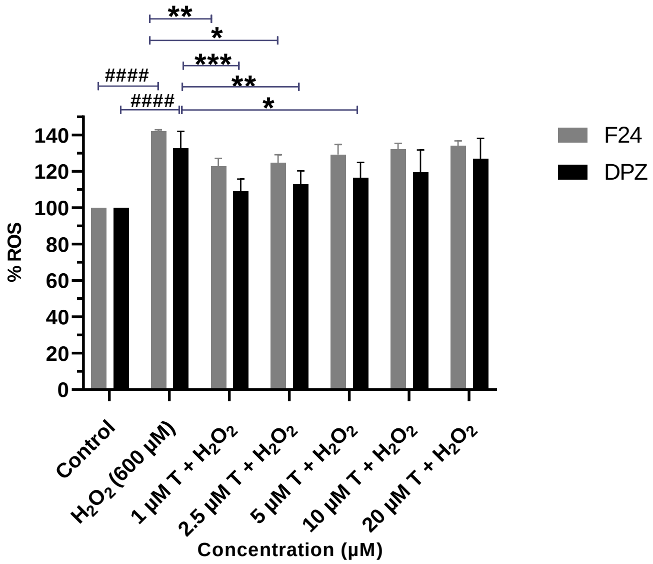

Figure 4.21. Cells were pre-incubated with treatment (**T**) **7a (F24)** or DPZ at 1, 2.5, 5, 10 and 20 μM concentrations for 24 h and further co-incubated with 600 μM H_2O_2 for additional 24 h. Percentage (%) ROS was assessed by using MitoSOX dye. All values are represented as mean ± SD of at least three independent experiments. $^{####}$P < 0.0001 vs control group, *P < 0.05, **P < 0.01 and ***P < 0.001 *vs* H_2O_2-treated group.

4.2.14. Protective effects of 7a (F24) against H_2O_2-induced DNA fragmentation and apoptosis

The extent of apoptosis and DNA strand breaks in the SH-SY5Y cells induced by H_2O_2 was analyzed by the terminal deoxynucleotidyl transferase dUTP Nick End-Labeling (TUNEL) assay. The procedure involved using modified EdUTP nucleotides which got incorporated at the 3’-OH ends of fragmented DNA by terminal deoxynucleotidyl transferase (TdT) enzyme. The detection of apoptosis by this assay is done through click reaction. SH-SY5Y cells were pretreated with **7a (F24)** followed by H_2O_2 for the next 24 h and followed by staining for TUNEL assay. SH-SY5Y cells treated with DNase (positive control) and the cells treated with H_2O_2 alone showed a significant increase in red-stained TUNEL-positive apoptotic cells, indicating apparent DNA frag-

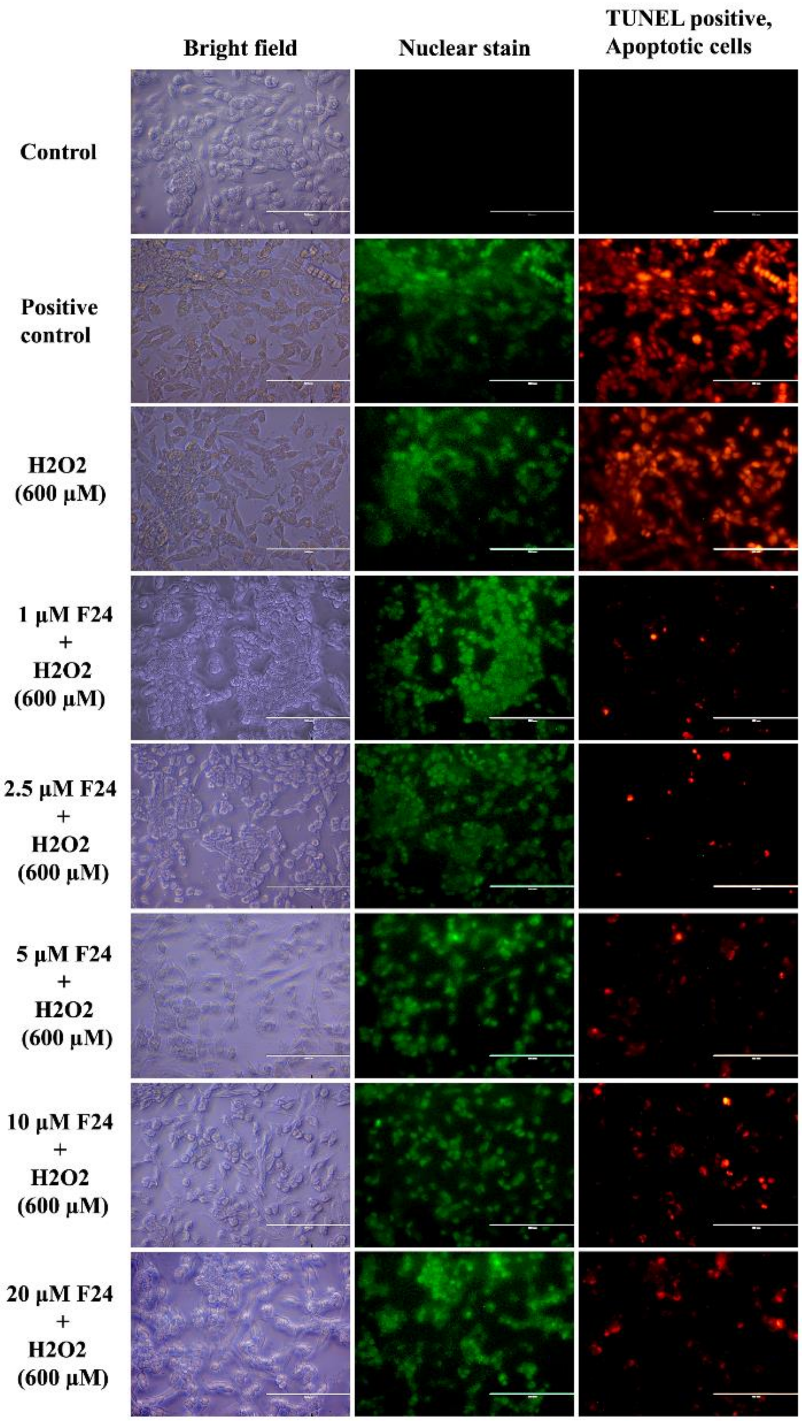

Figure 4.22. Detection of TUNEL-positive apoptotic strand breaks. SH-SY5Y cells were pre-incubated with **7a** (**F24**) at 1, 2.5, 5, 10, and 20 μM concentrations for 24 h and then further incubated with 600 μM H_2O_2 for another 24 h. DNase-treated SH-SY5Y cells are positive control. The cells were observed under a fluorescence microscope at 40X magnification—Green: nuclear stain; Red (TUNEL positive); orange: apoptotic cells.

-mentation apoptotic nuclei as compared to the control cells, which did not show any red stain (Figure 4.22). The number of TUNEL positive SH-SY5Y cells was significantly decreased when treated with different concentrations of **7a** (**F24**) (1, 2.5, 5, 10, and 20 μM), indicating protection against cell apoptosis (Figure 4.22**)**.

4.2.15. Protection against $A\beta_{1-42}$ induced aggregation modulation property of 7a (F24)

Treatment of SH-SY5Y cells with 5 μM $A\beta_{1-42}$ for 55 hrs caused significant (50.56%) loss of cell viability compared to control, evidenced through MTT assay (Figure 4.23). To test the neuroprotection ability of **7a** (**F24**) and DPZ against $A\beta_{1-42}$ induced neurotoxicity, SH-SY5Y cells were pretreated with different concentrations of **7a** (**F24**) and DPZ (5 and 10 μM) for 24 h, followed by co-treatment with $A\beta_{1-42}$ (5 μM) for 55 hrs, followed by cell viability measurement. As shown in figure 4.23B, pretreatment followed by co-treatment with **7a** (**F24**) significantly (23.66 % and 26.55 % with 5 μM, and 10 μM of **7a** (**F24**) respectively) increased the cells' viability compared to $A\beta_{1-42}$alone. Interestingly, DPZ also exhibited significant protection against $A\beta_{1-42}$induced cytotoxicity in all tested concentration ranges.

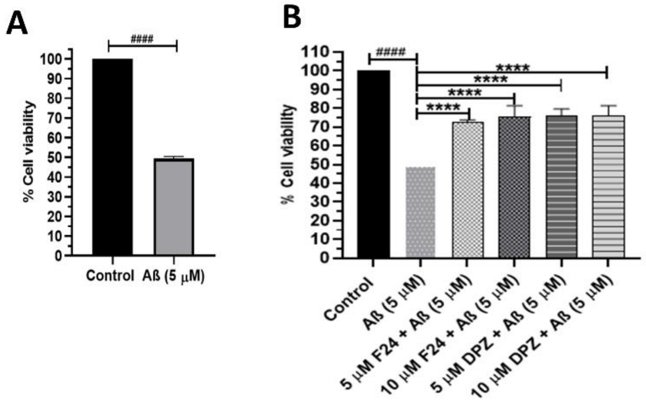

Figure 4.23. Protective effect of **7a** (**F24**) against Aβ induced cell death (**A**) Cell death induced by Aβ at 5 μM for 55 h. (**B**) Neuroprotective effect of **7a** (**F24**) or DPZ against Aβ mediated SH-SY5Y cell death. Cells were pre-incubated with **7a** (**F24**) or DPZ at 5 and 10 μM for 24 h and then further co-incubated with 5 μM Aβ for another 55 h. Cell death was assessed by MTT assay. All

values are represented as mean ± SD of at least three independent experiments. ****P < 0.0001 vs Aβ-treated group, $^{\#\#\#\#}$P < 0.0001 vs control group.

4.2.16. *In-vitro* blood-brain barrier (BBB) permeation study

To further validate the BBB crossing ability of **7a**, we carried out an *in-vitro* parallel artificial membrane permeability assay-BBB (PAMPA-BBB) assay following the manufacturer protocol and as recommended by Di Li *et al.* [171]. By using the PAMPA-BBB assay, the permeability (P_e) values of the commercially available drugs (testosterone, imipramine, corticosterone, hydrocortisone, and DPZ) known for CNS penetration were determined and compared with their reported values (Table 4.5). According to Di Li *et al.*, the permeability values were reported as $P_e > 4.0$ for compounds with high BBB permeability, Pe < 2.0 for compounds with low BBB permeability, and $4.0 > P_e > 2.0$ for compounds with uncertain permeability. From the results presented in table 4.5, it could be concluded that **7a** had a high BBB-permeability by passive diffusion with a P_e value of 6.24 ± 0.55.

Table 4.5. Permeability in the PAMPA-BBB assay for **7a**, testosterone, imipramine, corticosterone, hydrocortisone, and DPZ with their predictive BBB-penetration.

S.No.	compound	P_e (exp)^a	Reference value^b	Prediction^c
1.	**7a (F24)**	6.24 ± 0.55	------	CNS (+)
2.	Testosterone	20.01 ± 1.25	17.0	CNS (+)
3.	Imipramine	17.21 ± 1.21	13.0	CNS (+)
4.	Corticosterone	8.17 ± 1.10	5.1	CNS (+)
5.	Hydrocortisone	3.28 ± 1.03	1.9	CNS (-)
6.	DPZ^d	17.59 ± 1.17	------	CNS (+)

^{a}Data are the mean ± SD of two independent experiments.^{b}Reference values were taken from Di Li *et al.[171]* ^{c}CNS (+), $P_e > 4.0$, high permeability; CNS (-), Pe < 2.0, low permeability; CNS (±), $4.0 > P_e > 2.0$, uncertain permeability.^{d} DPZ (donepezil) reference AChE inhibitor drug.

4.2.17. Evaluation of *in-vivo* efficacy of F24 in the AD model of *Drosophila*

To further evaluate the *in-vivo* efficacy of **7a** (**F24**) against Aβ_{1-42} toxicity, we next assessed **7a** (**F24**) in Aβ_{1-42} dependent toxicity in *Drosophila*. We examined the neuroprotective efficacy of **7a** (**F24**) against eye tissue-specific Aβ induced toxicity in the fruit fly *Drosophila melanogaster*. Wild type (OregonR$^+$) flies grown in normal food media showed absolute healthy eclosion. However, wild-type flies administered with **7a** (**F24**) resulted in near-normal eclosion (65 to 92%) with concentrations ranging from 0.2 to 0.8 mg/ml. Although most of the **7a** (**F24**) treated flies found to be eclosed healthy and near normal to wild type at the concentrations of 0.6 and 0.8 mg/ml, significant lethality in flies was observed at concentrations 1 and 2 mg/ml with poor eclosion rates of 35% and 22%, respectively (Figure 4.24A).

In the case of AD expressing flies, 100% eye phenotypes [both mild (72.2%) and severe (27.8%) together] were observed when grown in normal food media, which is due to Aβ_{42} induced ommatidia death. In contrast, the same flies treated with **7a** (**F24**) showed significant rescue in increasing order with elevating concentrations of **7a** (**F24**) (Figure 4.24B). The AD flies treated with **7a** (**F24**) exhibited dose-dependent increase in rescue percentages of eye phenotypes such as 43% (0.2 mg/ml), 53% (0.4 mg/ml), 60% (0.6 mg/ml) and 68% (0.8 mg/ml), respectively. Thus, a 0.8 mg/ml concentration of **7a** (**F24**) is considered threshold concentration among all doses as it has shown the highest percentage of rescue in Aβ_{42} induced eye phenotypes [Figure 4.24 (B and C). The morphological eyes phenotypes of normal [Figure 4.24C (a)], diseased [Figure 4.24C (b-c)], and **7a** (**F24**) rescued [Figure 4.24C (d)] flies were recorded with the help of a digital camera attached with stereo zoom binocular. Thus, the study suggested a strong protective effect of **7a** (**F24**) against Aβ_{1-42}-induced toxicity in this *in-vivo* model.

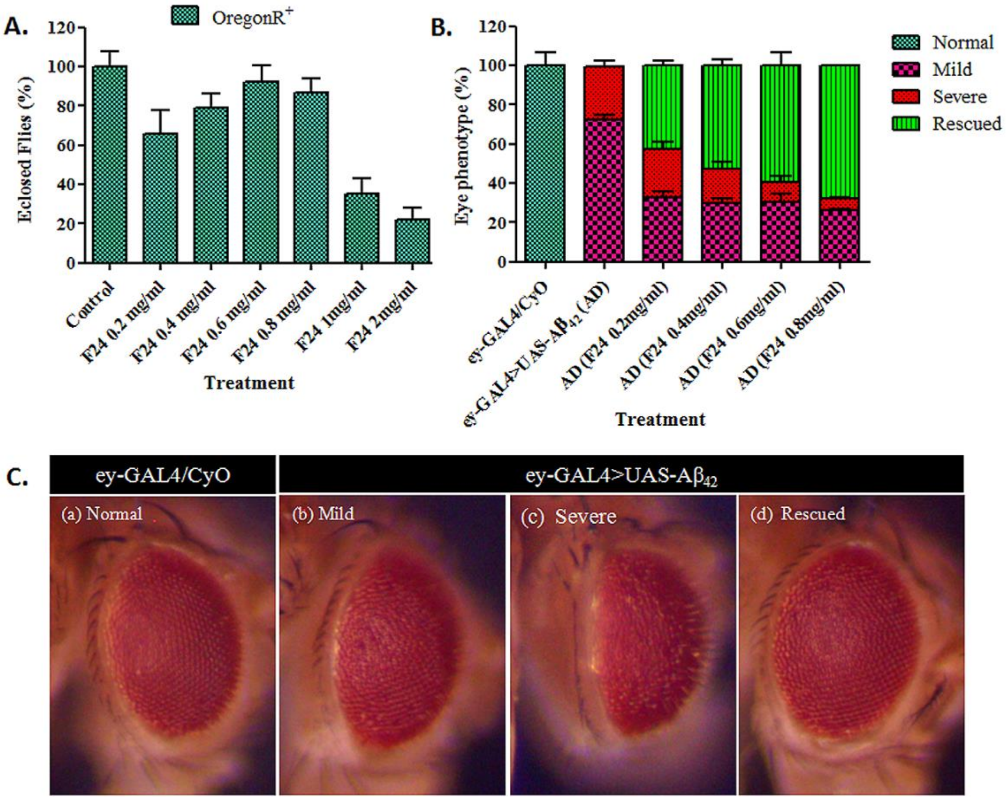

Figure 4.24. The histogram represents the *in-vivo* effects of **7a** (**F24**) on wild type and Aβ_{42} expressing flies. (**A**) Represents the median lethal dose (LD$_{50}$) determination using wild-type flies. (**B**) Quantitative analysis of rescue of eye phenotypes upon **7a** (**F24**) treatment. (**C**) Digital micrographs show a range of eye phenotypes of Aβ_{42} expressing flies (a to c) and its rescue upon F24 treatment (d).

7a (**F24**) improved the eye phenotypes scored in adult *Drosophila* [Figures 4.24 (B and C)]. Fruit flies were raised on a control food medium and food medium treated with different concentrations of **7a** (**F24**). The improvements in rough eye phenotypes of *Drosophila* were scored in a dose-dependent manner. Among all the treated concentrations of **7a** (**F24**), the 0.8 mg/ml **7a** (**F24**) shows a strong rescued percentage in eye tissues of AD flies. Interestingly, the dose dependent protection by **7a** (**F24**) was observed, with the maximum protection at dose of 0.8 mg/ml [Figures 4.24 (B and C)]. The results from the present study *in-vivo* fly model strongly supported our earlier *in-vitro* assay.

4.2.18. Molecular docking and dynamics simulations studies of 7a (F24) with Aβ_{1-42} fibrils

The molecular docking study was carried out to understand the binding site and different types of interactions of small molecule **7a** (**F24**) on Aβ_{1-42} protofibrils (PDB ID # 2BEG) using a customized version of Autodock Vina. Interestingly, **7a** (**F24**) was found to interact with the residues of chains C, D & E of protofibrils with a docking score of -8.1 kcal/mol. This particular binding pocket was found to have the lowest docking score and the highest number of docked conformation in this cluster. It is noteworthy that **7a** (**F24**) fits nicely into a pocket constituted by residues of chains C, D & E of protofibrils (Figure 4.25A and 4.25B). Further, **7a** (**F24**) makes π-π stacking interactions with Phe19 of chain-D of protofibrils. Furthermore, **7a** (**F24**) also forms two hydrogen-bonding interactions with Leu17C and Leu17E of pentameric Aβ_{42} fibrils (Figure 4.25C). Our docking studies showed that **7a** (**F24**) could interact with Aβ_{1-42} protofibrils via hydrophobic and hydrogen bonding and thereby modulate the aggregation of Aβ_{1-42} protofibrils.

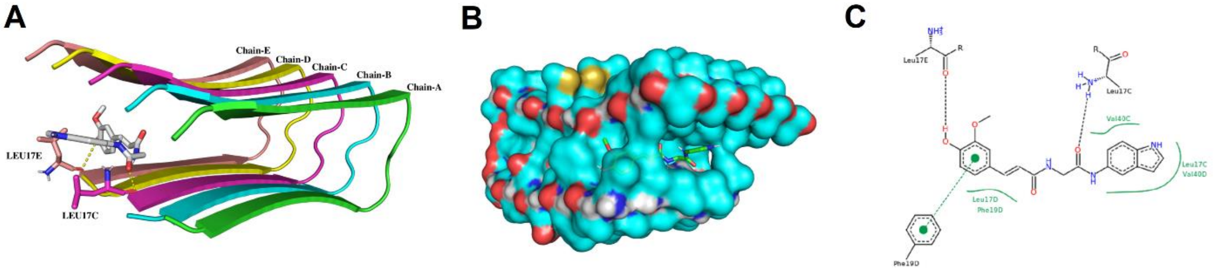

Figure 4.25. (**A**) Interaction of **7a (F24)** with Aβ_{1-42} protofibrils. (**B**) Surface representation **7a** (**F24**) docked into the pocket of Aβ_{1-42} protofibrils. (**C**) 2D interaction diagram of **7a** (**F24**) with Aβ_{1-42} protofibril.

Molecular dynamic simulations of protofibrils and protofibril-**7a** (**F24**) complex were performed for 200 ns at 310K. Binding free energy between **7a** (**F24**) and fibril was calculated using the MM-PBSA method. The binding energies were calculated for the last 10 ns at an interval of 50 ps. The total binding energy for the protofibril-**7a** (**F24**) complex was found to be -104.05 ± 1.45 kJ/mol.

Different components contributing to the final, binding energy of the protofibril-**7a** (**F24**) complex are shown in table 4.6. In terms of individual contribution towards binding energy, van der Waal interactions (-157.34 ± 1.15 kJ/mol) dominate above other interactions. Intriguingly, the unfavorable contribution of polar solvation energy (151.51± 1.42 kJ/mol) in the binding between **7a** (**F24**) and protofibril was greater than that of a favorable contribution of electrostatic interaction (-78.73 ± 1.80 kJ/mol) (Table 4.6). A similar result has been reported in the literature in binding interaction between the Aβ_{40} trimer and dihydromyricetin [172]. The contribution of individual residues towards the total binding energy of protofibril-**7a** (**F24**) complex was calculated, and per residue decomposition, the energy plot is depicted in figure 4.26. It is evident that the residues Leu17, Phe19, Ala21 from chain D and Leu34, Met35, Val18 from chain E are majorly contributing to the binding interaction of **7a** (**F24**) with protofibril. It can also be summarized that the residues from chain C, D & E have contributed more towards the total binding energy than chain A and B of protofibrils.

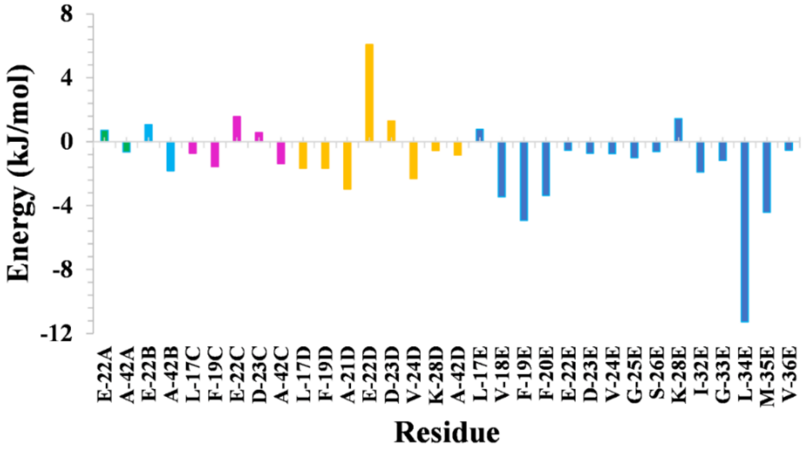

Figure 4.26. Binding free-energy (kJ/mol) contribution of critical individual residues of different chains (highlighted in different colors) in binding **7a** (**F24**) to Aβ_{1-42} protofibril.

Table 4.6. Binding Free Energy between Aβ_{1-42} protofibrils and **7a** (**F24**) in the Last 10 ns MD simulation.

S. No.	Energy components	Protofibril-**7a** (**F24**) complex energy (kJ/mol)
1	Van der Waal energy	-157.34 ± 1.15 kJ/mol
2	Electrostatic energy	-78.73 ± 1.80 kJ/mol
3	Polar solvation energy	151.51 ± 1.42 kJ/mol
4	SASA energy	-19.62 ± 0.09 kJ/mol
5	Binding energy[a]	-104.05 ± 1.45 kJ/mol

[a]Binding energy = polar + nonpolar.

4.2.19. Evaluation of Aβ_{1-42} fibrils disintegration property of 7a (F24) using molecular dynamics simulations

The protofibril and protofibril-**7a** (**F24**) complex's structural stability was investigated by comparing the change in RMSD, RMSF, Rg, and SASA during the whole simulation time. The average RMSD calculated for the last 50 ns of the simulation was found to be 0.87 ± 0.02 nm for protofibril, while the average value for protofibril-**7a (F24)** complex increases to 0.94 ± 0.02 nm (Table 4.7). RMSD plot in figure 4.27A depicts that protofibril-**7a (F24)** complex fluctuates at a higher RMSD value as compared to protofibril. Similarly, the radius of gyration (Rg) is another critical parameter that indicates any change in compactness of protein during the simulation. The average Rg value for protofibril was found to be 1.39 ± 0.01 nm, while it was 1.48 ± 0.01 nm for the protofibril-**7a** (**F24**) complex (Figure 4.27B). The increase in Rg value indicates an overall decrease in protofibrils' compactness in the presence of **7a** (**F24**) (Figure 4.27B). The solvent accessibility surface area (SASA) represents the contact of protein with solvent and is inversely correlated with the compactness of the protein structure. The SASA plot (Figure 4.27C) shows that the SASA values continuously increase with respect to time for the protofibril-**7a** (**F24**) complex compared to the protofibril alone. The average SASA value for protofibril in the absence of ligand was 76.91 ± 2.11 nm^2 while it was 80.86 ± 1.14 nm^2 (Table 4.7) in the presence of **7a** (**F24**). Thus, all computed parameters, *i.e.* increase in RMSD, Rg, and SASA, highlight the destabilization of $A\beta_{42}$ protofibrils in the presence of ligand **7a** (**F24**). A similar decrease in compactness of $A\beta_{42}$ protofibril in the presence of resveratrol and clioquinol hybrid, indicating the destabilization of the protofibril structure, has been reported earlier [173]. Apart from this, RMSF plot shows the fluctuation of individual residues of a particular chain (Figure 4.28). The increase in RMSF values, especially for chain-C, D, and E, also indicates that the **7a** (**F24**) destabilizes the protofibril.

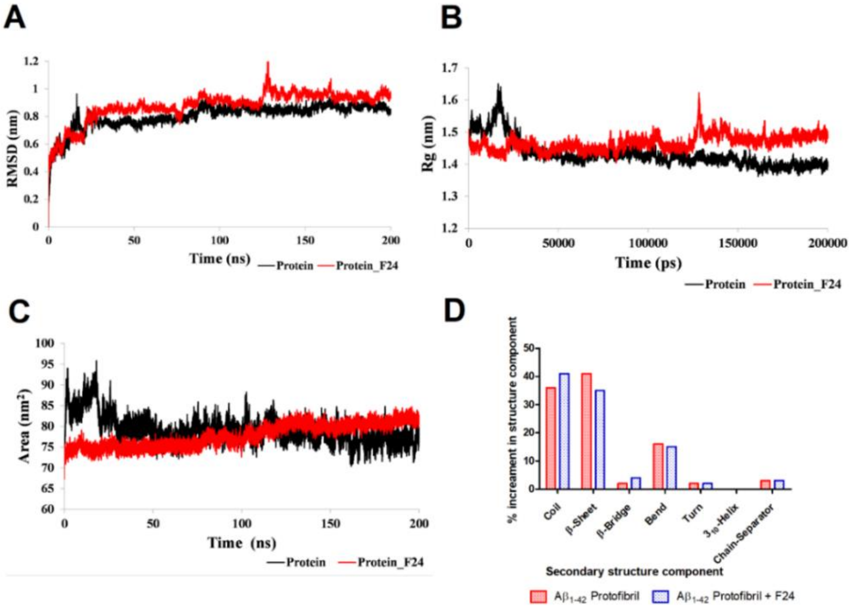

Figure 4.27. (**A**) RMSD (**B**) radius of gyration (**C**) solvent accessibility surface area (**D**) change in secondary structure content of protofibrils and protofibrils-**7a (F24)** complex obtained from molecular dynamics simulation data.

Table 4.7. Time-average and standard deviation of RMSD, Rg, and SASA value along with the sum of Eigenvalues for $A\beta_{1-42}$ protofibril and $A\beta_{1-42}$ protofibril-**7a** (**F24**) Complex.

S.No.	Parameters	$A\beta_{1-42}$ Protofibril	$A\beta_{1-42}$ Protofibril-7a (F24) Complex
1	RMSD (nm)	0.87 ± 0.02	0.94 ± 0.02
2	Rg (nm)	1.39 ± 0.01	1.48 ± 0.01
3	SASA (nm^2)	76.91 ± 2.11	80.86 ± 1.14
4	Sum of Eigen values	227.4	257.55

The change in the secondary structural content of protofibril and protofibril-**7a** (**F24**) complex during the simulation was also computed using the definition of the secondary structure of proteins (DSSP) proposed by Kabsch and Sander [174, 175]. The $A\beta_{1-42}$protofibrils were 41% of β-Sheet while this secondary structure content decreased to 35% in the protofibril-F24 complex. Also, an increase in the coil confirmation from 36% (in protofibril) to 41% (protofibril-**7a** (**F24**) complex) was noted (Figure 4.27D). Thus, the decrease in the percentage of β-Sheet and an increase in the coil content also show that **7a (F24)** decreases protofibrils' preference for β-Sheet conformation.

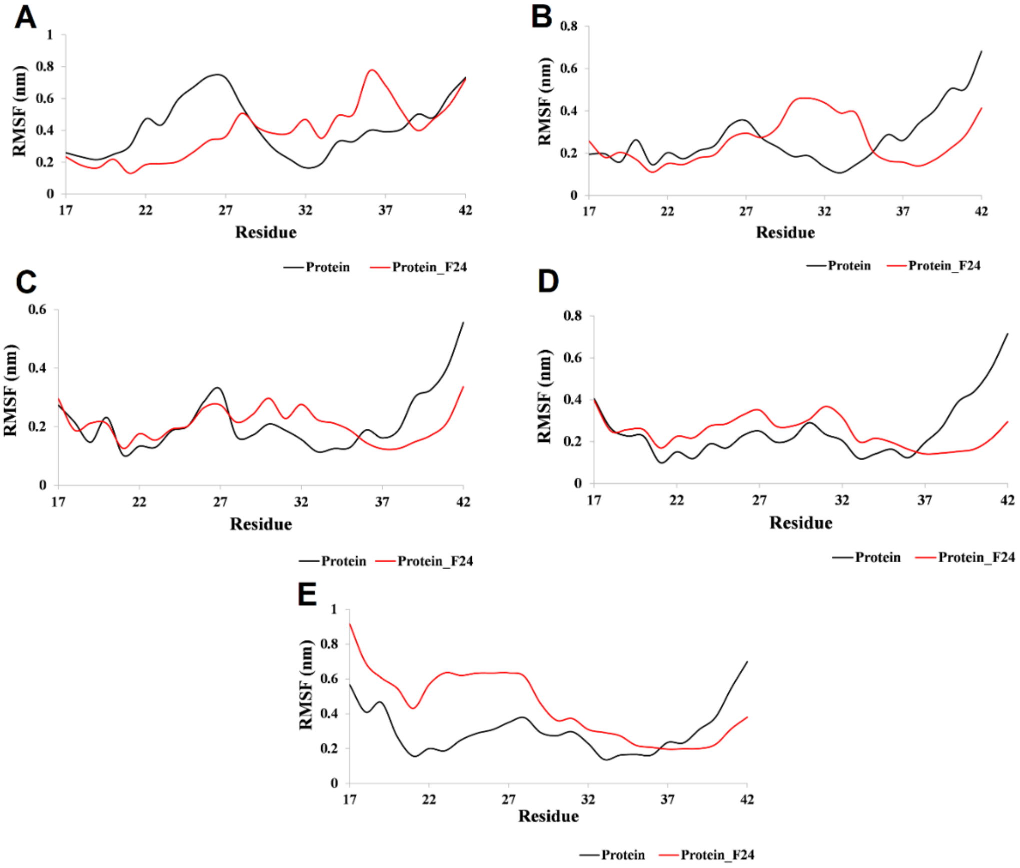

Figure 4.28. Root Mean Square Fluctuation (RMSF) of each residue for $A\beta_{42}$ and $A\beta_{1-42}$-F24 complex where (**A**) represents Chain A (**B**) represents Chain B (**C**) represents Chain C (**D**) represents Chain D and (**E**) represents Chain E of protofibrils.

Further, to investigate the effect of **7a** (**F24**) on the stability of Aβ_{1-42}, the binding energy between the chains was calculated for both protofibril and protofibril-**7a** (**F24**) complex using the MM-PBSA method from the last ten ns of the trajectory at the interval of 50 ps. It was found that the **7a** (**F24**) makes a significant decrease in binding affinity between chain C and D of protofibril. (Table 4.8). This substantial change in binding free energy between the chains of protofibril also suggests the possible destabilization, as previously reported in the literature.

Table 4.8. Average binding free energy along with its individual contributing terms for chain C and D of protofibril in presence and absence of **7a** (**F24**).

S.No.	Energy terms (kJ/mol)	Protofibril	Protofibril-**F24** complex
1	Van der Waal energy	-301.67 ± 1.18	-274.36 ± 18.36
2	Electrostatic energy	15.03 ± 5.73	83.13 ± 54.79
3	Polar solvation energy	276.95 ± 3.34	201.85 ± 37.18
4	SASA energy	-40.70 ± 0.11	-36.99 ± 2.23
5	Binding energy	-50.49 ± 4.04	-26.37 ± 45.99

4.2.20. Principal component analysis (PCA) of protofibril and protofibril-7a (F24) complex

PCA was used to analyze the difference in conformational motion induced by **7a** (**F24**) to protofibrils. The sum of eigenvalues reveals the total motility in the system, and it can be used to compare the flexibility of the protein. The sum of eigenvalues of the protofibril-**7a** (**F24**) complex was found to be considerably higher than the Aβ_{1-42} protofibril (Table 4.7). This shows that the **7a** **(F24)** destabilizes the protofibrils and increases the flexibility of protein to some extent. Our result is in line with the previously observed analysis in terms of structural stability and secondary structure content, which also shows the destabilization of Aβ_{1-42} protofibril in the presence of **7a** (**F24**). The first seven eigenvectors capture the main motion of the protein, accounting for greater than 80% of total motility (Figure 4.29A and 4.29B). The 2D plots of two principal components, *i.e.*, PC1 and PC2 having the largest eigenvalues for the protofibril and protofibril-**7a** (**F24**) complex, are depicted in figure 4.30A**,** and 4.30B. This plot shows the two conformational states represented by the red and blue dot, respectively, and the light blue or light red dot represents the intermediate state among those two conformational states. This plot also shows that the conformational space followed by the A$\beta_{1\text{-}42}$ protofibril is completely different from the protofibril-**7a** (**F24**) complex.

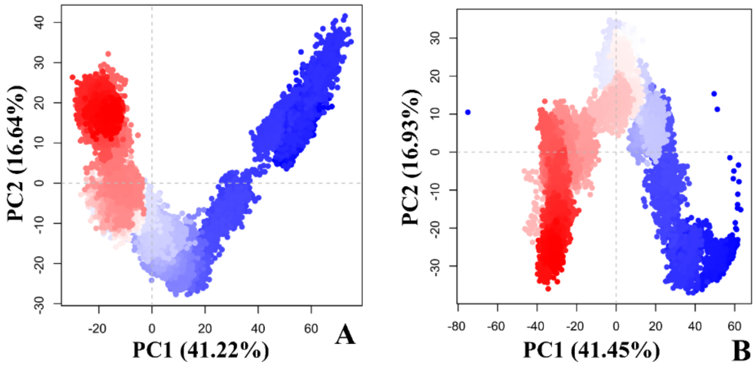

Figure 4.29. Projection of the motion of (**A**) A$\beta_{1\text{-}42}$ and (**B**) A$\beta_{1\text{-}42}$-7a (F24) complex in phase space along the first two principal eigenvectors at 300 K.

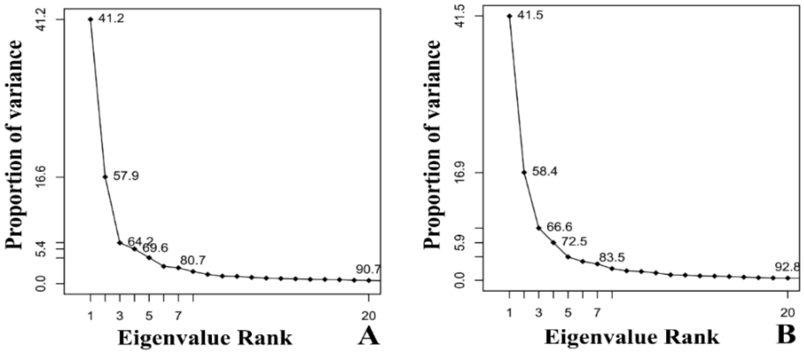

Figure 4.30. The eigenvalue rank along with proportion of variance (%) for (**A**) A$\beta_{1\text{-}42}$ and (**B**) A$\beta_{1\text{-}42}$-**7a** (**F24**) complex.

4.2.21. Acute toxicity studies in mice

In-vivo acute toxicity and hepatotoxicity are two essential criteria in the development of drug candidate. Based on potent enzyme inhibitory activity and other multifunctional properties, compound **7a** (**F24**) was selected for acute toxicity and hepatotoxicity studies (Figure 4.31). The acute toxicity of compound **7a** (**F24**) was determined on healthy male Swiss albino mice (25-30 g), as per the OECD guidelines. Female mice were excluded from the experiment due to the complexicity caused by the estrous cycles. From the first 4 h throughout 14 days after administration of **7a** (**F24**), no acute toxicity symptoms, such as death, abnormal behavior, changes in water or food consumption, or weight loss were observed (Figure 4.31C). All animals were sacrificed on the 14th day after drug administration and microscopically examined for possible damage to the liver (Figure 4.31A and 4.31B). The results showed that the animals treated with compound **7a** (**F24**) did not develop any sign of toxicity and were well-tolerated **7a** (**F24**) at doses up to 500 mg/kg.

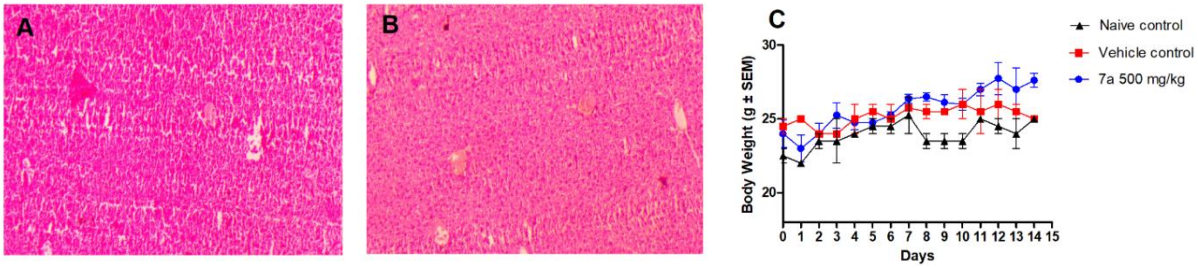

Figure 4.31. Histomorphological appearance of liver of mice. (**A**) no treatment (Naive control); (**B**) **7a** (**F24**)**,** 500 mg/kg. (**C**) Mean daily bodyweight profile of each group of mice during the 14-day drug administration period**.**

4.2.22. Evaluation of *in-vivo* efficacy of 7a (F24) in scopolamine-induced AD mice model

A learning and memory improvement experiment was performed using the Y maze involving daily p.o. administration of compound **7a** (**F24**) to mice suffering from learning and memory dysfunction [176]. Learning and memory impairment in mice can be produced by scopolamine-induced blockage of the muscarinic cholinergic receptor nerve terminals, which is a well-established animal model for AD [177]. In acute toxicity study, we found that upto 500 mg/kg compound **7a** (**F24**) did not develop any toxic symptoms, indicate safety profile of drug upto 500 mg/kg. The test compound (**7a**) was administered daily to healthy male Swiss albino mice at the dose of 6.25, 12.5 and 25 mg/kg, p.o., for 7 days and body weights were analyzed (Figure 4.32A). On the 7th day, the Y maze experiment was performed to assess the spatial working memory in mice after intraperitoneal administration of scopolamine hydrochloride (3.0 mg/kg). The animals were treated with **7a** (**F24**) or **FA** or DPZ 30 min prior to scopolamine administration and spontaneous alterations were calculated 15 min after scopolamine treatment. A significant reduction in spontaneous alternation was observed in the scopolamine hydrochloride (3mg/kg,i.p.) treated group compared to the vehicle control group, which indicated the development of amnesia in the mice (Figure 4.32B, $^{***}p < 0.001$). The DPZ treated group (5.0 mg/kg, p.o.) showed significantly increased spontaneous alternations ($^{\#\#\#}p < 0.001$) compared to the scopolamine treated group. A similar result was observed with **7a** (**F24**) (6.25, 12.5 and 25mg/kg), which showed statistically significant difference in % spontaneous alternations compared to scopolamine and DPZ treated group (Figure 4.32B, $^{\#\#\#}p < 0.001$ vs scopolamine, $^{\pi\pi}p < 0.01$, $^{\pi}p < 0.05$ vs DPZ, ns to DPZ in case of 6.25 mg/kg). On the other hand, **FA** (12.5 and 25 mg/kg) did not show any significant difference in spontaneous alternation compared to scopolamine (Figure 4.32B, p = ns). The mechanism of the spontaneous alternation stimulation in the scopolamine model is likely mediated by the anti-AChE activity of the compound **7a** (**F24**), suggesting that **7a** (**F24**) is a potent cholinesterase inhibitor that can cross the blood-brain barrier effectively. The total arm entries (Figure 4.32C) remained unchanged in all treated groups, indicating that scopolamine did not affect the locomotor activity in mice. The overall results of the scopolamine-induced amnesia model suggested that **7a** (**F24**) showed significant potential for improving spatial and immediate memory in mice.

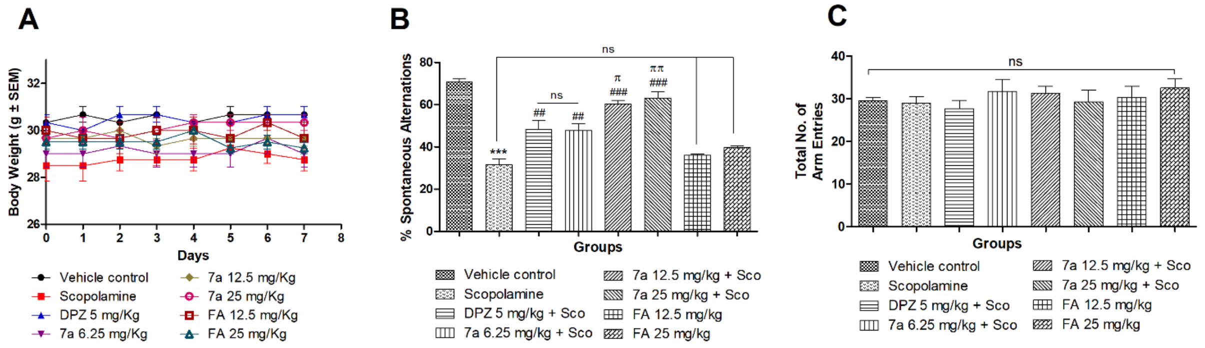

Figure 4.32. Scopolamine-induced memory deficit in mice. (**A**) Mean daily bodyweight profile of each group of mice during the 7-day drug administration period. (**B**) Effect of **7a** (**F24**) on scopolamine-induced memory deficit in the Y-maze test. Compound **7a** (**F24**) (6.25, 12.5, and 25 mg/kg, p.o.), **FA** (12.5, and 25 mg/kg, p.o.), DPZ (5 mg/kg, p.o.) were given for 7 days. On the 7th day, the mice were treated with scopolamine (3mg/kg, i.p.) and subjected to the Y-maze test after 15 min of scopolamine administration. (**C**) Number of arm entries in the Y-maze test. Data are expressed as the mean ± SEM (n = 5),***$p < 0.001$ vs vehicle control; $^{###}p < 0.001$, $^{##}p < 0.01$vs scopolamine; $^{\pi\pi}p < 0.01$, $^{\pi}p < 0.05$ vs DPZ; ns = nonsignificant (One-way ANOVA followed by Tukey's multiple comparison test).

4.2.23. *Ex-vivo* neurochemicals estimation and antioxidant property evaluation

To investigate levels of AChE, BChE and antioxidant effect of **7a**, *ex vivo* studies were performed with the treated animals. AChE, and BChE levels in the brain were assessed by Ellman's colorimetric method with slight modifications. As described in figure 4.33A and figure 4.33B, scopolamine significantly elevates AChE and BChE levels compared to the vehicle control group, while DPZ and **7a** (**F24**) groups showed a significant reduction in elevated AChE and BChE levels. However, a non-significant difference was observed in elevated levels of AChE and BChE in the case of **FA** at 12.5 and 25 mg/kg. These findings suggest that **7a** (**F24**) significantly attenuates the cholinesterase levels in the brain, but **FA** is not able to reverse the scopolamine-induced increase in AChE, and BChE levels. The *ex-vivo* antioxidant property of **7a** (**F24**) was estimated using various biochemical parameters such as superoxide dismutase (SOD), catalase (CAT) and malondialdehyde (MDA). SOD is an enzyme that protects cellular components from oxidation by ROS and eventually reduces cellular damage. It catalyzes the dismutation of the superoxide (O^{2-}) radical into molecular oxygen (O_2) and hydrogen peroxide (H_2O_2). CAT is a common enzyme that catalyzes the decomposition of hydrogen peroxide (H_2O_2) to water and oxygen. MDA (a byproduct of lipid peroxidation) is a marker for oxidative stress. MDA undergoes condensation with thiobarbituric acid to give red fluorescence. As shown in figure 4.33C, the scopolamine-treated mice group showed a significant reduction in SOD levels. Interestingly, the SOD level was noticed to be significantly increased in DPZ (Figure 4.33C) treated animals.

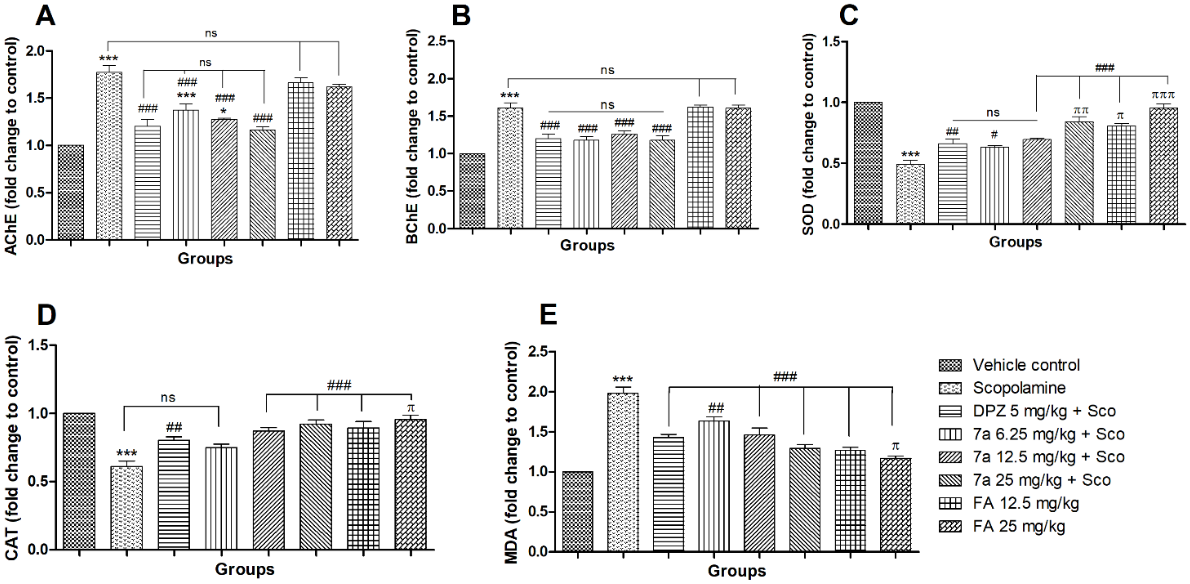

Figure 4.33. The *ex-vivo* AChE, BChE and antioxidant effect of DPZ (5 mg/kg), compound **7a** (**F24**) (6.25, 12.5 and 25 mg/kg), **FA** (12.5, 25 mg/kg) and scopolamine (3 mg/kg). (**A**) Elevated AChE. (**B**) BChE levels by scopolamine treatment were significantly reduced by **7a** (**F24**). (**C**) SOD (Fold change to vehicle control). (**D**) Catalase (CAT) (fold change to vehicle control). (**E**) MDA (fold change to vehicle control). Data are expressed as mean ± SEM (n = 5), ***$p < 0.001$ vs vehicle control; $^{###}p < 0.001$, $^{##}p < 0.01$ and $^{\#}p < 0.05$ vs scopolamine group; $^{\pi\pi\pi}p < 0.001$, $^{\pi\pi}p < 0.01$, $^{\pi}p < 0.05$ vs DPZ; ns = non-significant (One-way ANOVA followed by Tukey's multiple comparison test).

Treatment with the lead molecules **7a** (**F24**) and **FA** could effectively reverse the reduced level of SOD in scopolamine-treated animals. Additionally, significant increases in catalase (CAT) activity in brain supernatant was observed in the DPZ (Figure 4.33D), **7a** (**F24**), and **FA** treatment group, while the MDA contents were correspondingly decreased in DPZ, **7a** (**F24**), and **FA** compared to those of the scopolamine treated group (Figure 4.33E). These findings collectively suggest the potent *in-vivo* ChE inhibitory and antioxidant activities of **7a** (**F24**).

4.2.24. Evaluation of *in-vivo* efficacy of 7a (F24) in scopolamine-induced AD mice in water maze model

The improvement in cognitive impairment is the essential criterion for the successful development of anti-AD agents. The Morris water maze (MWM) test permits the accurate and reproducible study of reference memory, cognitive maps, place learning, spatial learning, and working memory [177]. Therefore, we evaluated the ability of **7a** (**F24**) to improve scopolamine-induced memory impairments in this model. During the experimental period, changes in water or food consumption and body weight were closely observed (Figure 4.34A). The respective drug doses of **7a (F24)** (1 and 2.5 mg/kg) and DPZ (1 mg/kg) were administered *i.p.* 30 min before the administration of scopolamine (1.4 mg/kg) to their respective groups for consecutive 22 days (Figure 4.34B). During the 18-22th (four training and 5th test) days of the treatment period, ELTs were recorded for the different treatment groups. In MWM test, animals in control and vehicle control groups exhibited a reduction of ELT from 60 s (1st training day) to 7.40 ± 2.01 s (5th test day) and 57.66 ± 1.23 s (1st training day) to 7.83 ± 1.86 s (5th test day) ,respectively (Figure 4.34B). From day 18-22nd of the treatment period, scopolamine (1.4 mg/kg, ip) -treated animals exhibited a significant prolongation of ELT from 58.23 ± 1.41 s (1st training day) to 52.57 ± 3.61s (5th test day) compared to the control and vehicle control groups signify the development of amnesia in mice (Figure 4.34B, $p < 0.001$. While DPZ significantly reduced ELT from 60 (1st training day) to 7.50 ± 0.99

s (5th test day) (Figure 4.34B, $p < 0.001$) compared to the scopolamine-treated group. Compound F24 at doses of 1 and 2.5 mg/kg remarkably reduced ELT (Figure 4.34B**,** $p < 0.001$) from 59.07 ± 0.92 s (1st training day) to 9.8 ± 1.15 s, (5th test day) and 58.37 ± 1.16 s (1st training day) to 7.83 ± 1.90 s (5th test day), respectively (Figure 4.34B**,** $p < 0.001$) thereby, significantly attenuate memory impairment (Figure 4.34B). The escape latency time shown by **7a (F24)** at a dose of 2.5 mg/kg was somewhat more efficacious than 1 mg/kg. Thus, the compound **7a (F24)** turned out to be potent in tested doses (1 and 2.5 mg/kg) in this animal model. These outcomes collectively suggested that the animals could retain the previous memory in the MWM experiment. Therefore, we can conclude that **7a (F24)** led to a significant improvement of the spatial and working memory in the scopolamine-induced MWM model.

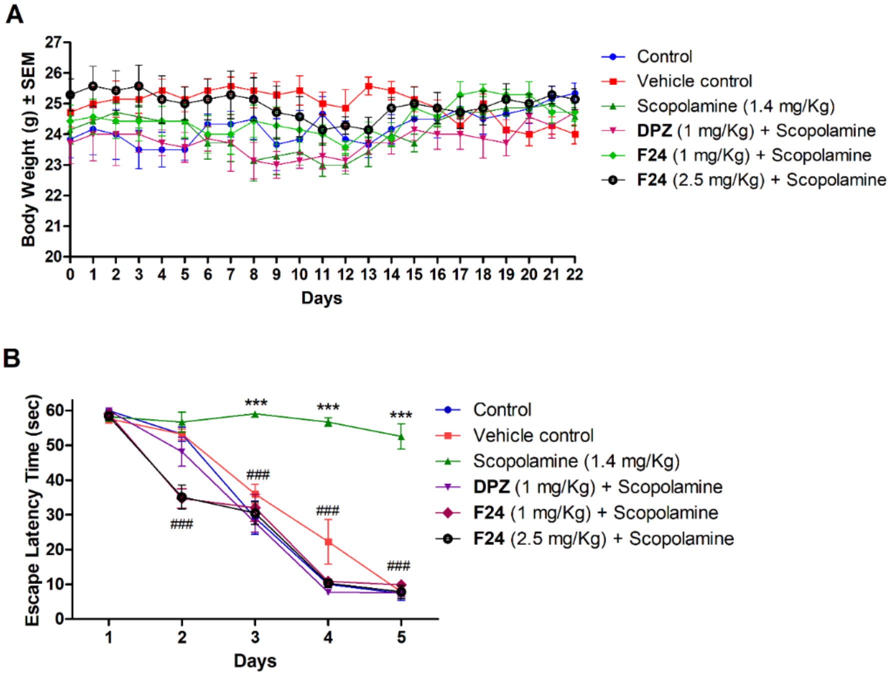

Figure 4.34. Scopolamine-induced memory deficit mice model study. (**A**) Mean daily bodyweight. (**B**) Escape latency time (in second, last five days from 18-22nd day). Data are expressed as mean ± SEM (n = 7). (***) $p< 0.001$, *vs* control group; (###) $p< 0.001$, *vs* scopolamine-treated group.

4.3.1. Chemistry involved synthesizing the second series of compounds

New **FA**-benzyl piperazine hybrids **13a-13p** were obtained as mentioned in scheme 4 (page # 56). The synthesis of target compounds was completed using a well-established synthetic method. Commercially available benzyl halides (**11e-11g, 11i,** and **11m-11o**) underwent nucleophilic substitution reaction (S_N2) with piperazine in ethanol to give compounds **12e-12g, 12i,** and **12m-12o**. The target compounds **13a-13p** were obtained by the reaction of substituted benzylpiperazine (**12a-12p**) with **FA** using the standard amide coupling method (EDCI.HCl, HOBt, and DIPEA). The molecular hybrids of **FA** and substituted amines connected with alanine linker were synthesized by following the reaction steps mentioned in scheme 5 (page # 57). In the first step, *N*-Boc-propanamide derivatives (**16a-16c**) were obtained by standard amide coupling of substituted amines with Boc-alanine. In the next step, *N*-Boc-protected secondary amine groups were then deprotected by ethereal HCl to yield **17a-17c**. Finally, the compounds **18a-18c** were synthesized by the reaction of substituted alanine with **FA** using standard amide coupling. To obtain **FA**-tryptamine-based hybrid analogs (**23a-23c**), we followed the synthetic route depicted in scheme 6 (page # 57). First, the Boc-glycine was reacted with a substituted tryptamine (**20a-20c**) to obtain the desired intermediates **21a-21c**. After Boc deprotection, the final compounds (**23a-23c**) were obtained using standard amide coupling with **FA**. All newly synthesized hybrids were purified by chromatographic techniques and structurally characterized by ^{1}H-NMR,^{13}C-NMR, and high-resolution mass spectrometry (HRMS).

4.3.2. Biological evaluation of the second series of compounds

4.3.2.1. Design of the second series of novel naturally inspired FA analogs

In our continuous efforts to develop naturally inspired multifunctional molecules for AD management, earlier we reported a novel series of **FA** template-based AChE/BChE inhibitors that possess potential antioxidant, Aβ_{1-42} aggregation modulation property, and iron-chelation ability [112]. One of the major goals behind the novel **FA** analogs' design is to improve the AChE inhibition and antioxidant potential of **FA**-derived compounds. One of the findings from our previous SAR studies is that we observe a loss in the free radical quenching ability of most developed molecules compared to **FA**. Intriguingly, the phenyl piperazine derivatives (PPD) **10a**, **10b**, and **10g** (Figure 4.35) have shown promising free radical quenching ability (IC_{50} = 61.98 ± 0.30 μM) for **10b** (Figure 4.35) in DPPH assay with a potency comparable to that of parent natural compound **FA** (IC_{50} = 56.49 ± 0.62 μM). However, we have shown that the coupling of substituted phenyl piperazine moiety with **FA** with glycinamide linker leads to a mixed impact on AChE/BChE inhibition. The developed PPD was found to be moderate to weak inhibitors of the target enzymes (IC_{50}, AChE, 9.91 ± 0.07 to 29.34 ± 0.03 μM, % BChE inhibition, 26.89 ± 0.20 to 44.71 ± 0.05 for **10a**, and **10g**, respectively, Figure 4.35). Given the key role of oxidative stress (OS) in AD pathogenesis and the potent antioxidant potential of the developed PPD, we planned to improve upon the AChE/BChE while maintaining ClogP of the designed molecules in the desired range as per our earlier publication [112]. Based on our studies, we hypothesized that the nature of the long active site of AChE/BChE and the relatively short structure of PPD is probably the reason for their moderate inhibitory activity. Hence, in the 4rd series of SAR studies, we planned to introduce a spacer between phenyl and piperazine ring in the designed molecules. Therefore, the phenylpiperazine ring was replaced with benzylpiperazine. Thus, compounds **13a-13p** were designed and synthesized to improve the AChE/BChE inhibition and antioxidant potential while maintaining ClogP in the desired range (Table 4.9). The addition of hydrophobic features will also help the analogs to be able to interact with the essential hydrophobic residues at the active site of the enzymes. Despite these structural modifications, none of the tested compounds significantly improved in the enzyme inhibition studies compared to the earlier reported PPD. Therefore, to further improve upon the AChE/BChE inhibition, we planned to increase the linker length in our earlier reported potent cholinergic inhibitors glycine amide derivatives **4a, 4f**, and **4j** (Figure 4.35). In our earlier study, we have demonstrated that our **FA** derivatives exhibited the highest potency when the methylene linker length is one (n = 1). In this manuscript, we rationally and selectively synthesized only three molecules (**18a-18c**), as a part of our SAR study, with a linker length two to observe whether this structural modification can further potentiate cholinergic inhibitions. Therefore, to evaluate the effect of a two-methylene linker size connecting **FA** and phenyl ring, 5th series compounds **18a-18c** were designed and synthesized. Intriguingly, none of the developed compounds showed an improved AChE/BChE inhibitory property (Table 4.9) over the earlier reported compounds (**4a, 4f**, and **4j)**. One of the major goals of this study is to improve upon the enzyme inhibition and antioxidant properties of our earlier identified molecules. In our recent publication, we have identified **7a** (Figure 4.35) as a potential multifunctional agent able to provide both symptomatic relief and neuroprotection for the management of AD. Given the significant role played by the presence of indole moiety in **7a** in the interaction with the target enzymes and antioxidant property, the 6th series of compounds where **FA** and tryptamine moieties were joined through optimized glycine amide to improve upon the AChE/BChE inhibition and antioxidant property.

4.3.2.2. Cholinesterases inhibition studies

Given the significant role played by ACh and butyrylcholine (BCh) in memory and cognitive impairment in various stages of AD, therefore, cholinesterase's inhibitory activity of the newly synthesized compounds against human AChE and equine BChE was measured by using the spectroscopic method of Ellman *et al.* [178]. The inhibitory activity is expressed as IC_{50}, i.e., the inhibitor concentration that reduces the cholinesterase activity by 50%. In this study, **DPZ** served as the reference drug, and **FA** was used as the negative control.

In our initial attempt to explore the possible changes in enzyme inhibition properties due to such structural changes, compound **13a** was synthesized and evaluated for ChEs inhibitory activities. In the enzyme inhibition studies, **13a** bearing unsubstituted benzylpiperazine fragment exhibited potent AChE inhibitory property (IC_{50}, AChE (μM) = 13.34 ± 0.28) compared to **10a** (IC_{50}, AChE (μM), = 29.34 ± 0.03). Interestingly, **13a** (Figure 4.35) was approximately twice more potent compared to **10a**). However, in the BChE inhibition assay, **13a** turned out to be equipotent compared to **10a** (% BChE inhibition 45.13 ± 0.61, and 37.03 ± 0.41 for **13a** and **10a,** respectively**)**. This result indicated that benzylpiperazine fragment was well tolerated on the enzyme sites. Further, the methyl group was introduced on various positions of the phenyl ring of benzyl piperazine fragment, leading to the generation of compounds **13b-13d**. Intriguingly, compounds bearing methyl group at different positions of benzylpiperazine fragment showed weak inhibition towards AChE over **13a** (IC_{50}, AChE (μM), >20 for **13b-13d**) over the earlier reported 4-methyl phenylpiperazine derivative **10g** (IC_{50}, AChE (μM) = 19.48 ± 0.12, **10g**, Figure 4.35). Intriguingly, in case of BChE inhibition assay the developed molecules were found to be potent inhibitors over **13a** (IC_{50}, BChE (μM), **13b** = 15.06 ± 0.38, **13c** = 14.69 ± 0.35, and **13d** = 14.75 ± 0.31 μM, and % BChE inhibition 37.03 ± 0.41 for **13a**). It is worth mentioning that in the case of BChE inhibition, substitution of a methyl group on benzylpiperazine was better tolerated over our earlier reported methyl-substituted phenylpiperazine compound **10g** (% BChE inhibition 38.14 ± 0.12). To further validate our previous results on the electron-donating group (EDG), we introduced monomethoxy group onto our parent molecule **13a,** which led to the generation of compounds **13e** (*o*-OCH_3), and **13f** (*p*-OCH_3). In the enzyme inhibition assay, the compounds with monomethoxy group effectively inhibited AChE and were equally potent to **13a** (IC_{50}, AChE (μM), **13e** = 15.18 ± 0.36, and **13f** = 16.39 ± 0.42). However, the introduction of the monomethoxy group on the benzylpiperazine, a significant reduction towards BChE inhibition was observed compared to **13b-13d** (% BChE inhibition 49.12 ± 0.63 and 45.13 ± 0.67, **13e** and **13f,** respectively). These results concur with our previous finding with the PPD where we observed that the introduction of methoxy group could increase the developed molecules inhibitor activity towards AChE.

We further explored various electron-withdrawing groups (EWGs) on benzylpiperazine ring to explore the significance of various electronic features on the AChE/BChE inhibition. Therefore, compounds **13g-13l** were designed, synthesized and evaluated for the enzyme inhibition assays. In this study, **13k** bearing *m*-fluoro turned out to be most potent among all developed molecules so far [IC_{50}, AChE (μM), **13h** (*m*-chloro) = 15.43 ± 0.28, **13k** (*m*-fluoro) = 13.13 ± 0.26, and **13l** (*p*-fluoro) = 14.54 ± 0.65 μM]. Interestingly, all the developed molecules (**13g-13l)** were found to be equipotent inhibitors of BChE [IC_{50}, (μM), **13g** (*o*-chloro) = 15.21 ± 0.29, **13h** (*m*-chloro) = 14.80 ± 0.34, **13i** (*p*-chloro) = 15.86 ± 0.31, **13j** (*o*-fluoro) = 15.89 ± 0.23, **13k** (*m*-fluoro) = 14.03 ± 0.22, and **13l** (*p*-fluoro) = 14.85 ± 0.37 μM]. We further introduced bulky EWGs on the benzylpiperazine fragment in order to explore their effect on enzymes inhibition properties. Therefore, compound **13m-13p** were developed and evaluated for enzymes inhibition. Surprisingly, all developed compounds exhibited weak inhibitory activity towards AChE (IC_{50}, AChE (μM), >20 μM). In contrast, the developed molecules **13m-13p** were found to be potent inhibitors of BChE over **13a** (IC_{50}, BChE (μM), **13m** = 14.89 ± 0.26, **13n** = 14.73 ± 0.31, **13o** = 15.58 ± 0.44, and **13p** = 14.62 ± 0.16 μM, respectively).

Despite these promising results, none of the tested compounds showed significantly improved enzymes inhibition studies than earlier reported phenylpiperazine derivatives. Therefore, to improve upon the AChE/BChE inhibition, compounds **18a-18c** were designed and synthesized. To evaluate the effect of a two-methylene linker size connecting **FA** and phenyl ring, compounds **18a** were designed and synthesized. This compound exhibited slightly more potent activity towards AChE ($IC_{50,}$ AChE (μM) = 14.75 ± 0.42) while significant increase in BChE inhibition ($IC_{50,}$ BChE (μM) = 16.38 ± 0.37) was observed in comparison to **4j** [$IC_{50,}$ AChE (μM) = 21.94 ± 0.81, BChE (% inhibition) = 38.25 ± 0.25]. Our earlier enzyme inhibition studies also demonstrated that compounds with *m*-methoxy and *p*-chloro on the terminal phenyl ring are comparatively potent enzyme inhibitors over the other developed **FA** analogs. We specifically incorporated these groups in the development of molecules **18b-18c** with increased linker length to investigate the impact of linker length on enzyme inhibition. Among the three compounds (**18a-18c**), **18b** exhibited maximum inhibition for AChE (IC_{50}, AChE (μM) = 2.41 ± 0.42). While **18c** was found to be most potent inhibitor towards BChE (IC_{50}, BChE (μM) = 7.13 ± 0.37 μM). Thus, it demonstrates that the optimal methylene linker size is one in a similarly substituted series of **FA** template. These results indicated that the introduction of propenamide linker instead of glycine amide did not improve upon the enzymes inhibitory property (Table 4.9).

The indole moiety played a key role in the interaction of the targets enzymes and could reverse the loss in antioxidant property in **7a**, therefore, tryptamine ring bearing in the third series of molecules were developed and tested. In this series, three compounds were designed, synthesized, and evaluated for enzyme inhibition studies. Interestingly, compounds **23a**-**23c** bearing tryptamine functionality showed significant AChE/BChE inhibition over the earlier reported compounds. The developed molecules were found to be equipotent towards AChE inhibitory activity (IC_{50}, AChE (μM), **23a** = 1.42 ± 0.24, **23b** = 0.96 ± 0.14, and **23c** = 0.84 ± 0.12) (Figure 4.36). Similarly, the developed compounds were found to be potent inhibitor of BChE (IC_{50}, BChE (μM), **23a** = 3.14

± 0.28, **23b** = 1.23 ± 0.23, and **23c** = 1.29 ± 0.22). These results collectively suggested that both EWG or EDG on tryptamine moiety were well tolerated on enzymes. The SAR on this series of all developed molecules is represented in figure 4.37.

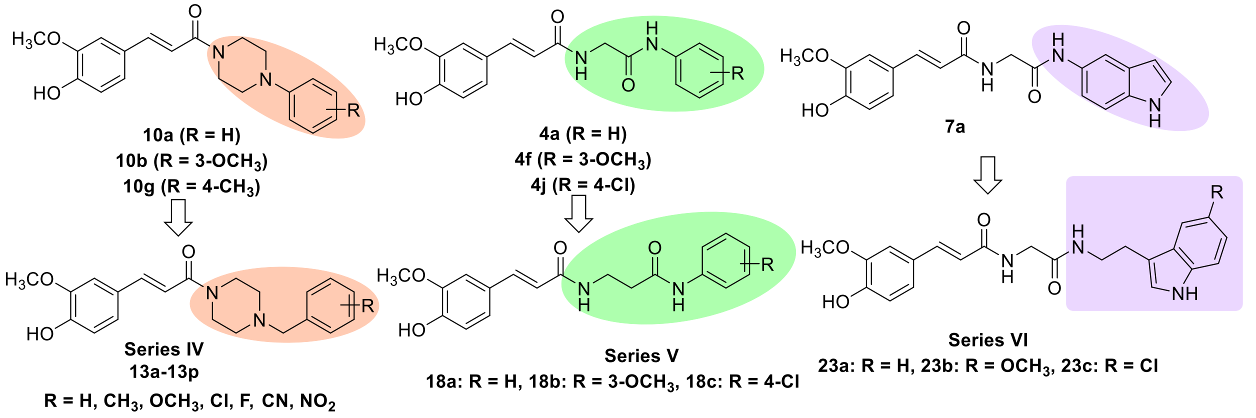

Figure 4.35. Design of the multifunctional ChEs inhibitors by integrating the structural features of ferulic acid (**FA**) derivatives.

Table 4.9. Structures, ChEs inhibitory activities, cLogP, and tPSA of compounds **13a-13p**, **18a-18c** and **23a-23c**.

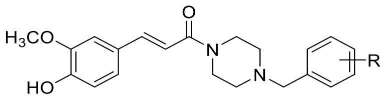

13a-13p

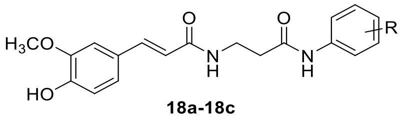

18a-18c

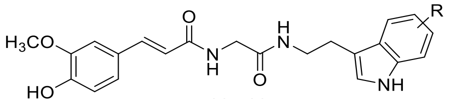

23a-23c

Compd.	R	IC$_{50}$ (μM)^a or % inhibition ^{b}		tPSA^c	cLogP^c
		*h*AChE	*eq*BChE		
13a	Hydrogen	13.34 ± 0.28	45.13 ± 0.61%	53.01	3.22
13b	2-methyl	43.10 ± 0.84%	15.06 ± 0.38	53.01	3.67
13c	3-methyl	45.50 ± 0.86%	14.69 ± 0.35	53.01	3.72
13d	4-methyl	43.16 ± 0.69%	14.75 ± 0.31	53.01	3.72
13e	3-methoxy	15.18 ± 0.36	49.12 ± 0.63%	62.24	3.14
13f	4-methoxy	16.39 ± 0.42	45.13 ± 0.67%	62.24	3.14
13g	2-chloro	46.99 ± 0.87%	15.21 ± 0.29	53.01	3.94
13h	3-chloro	15.43 ± 0.28	14.80 ± 0.34	53.01	3.94
13i	4-chloro	37.26 ± 0.85%	15.86 ± 0.31	53.01	3.94
13j	2-fluoro	34.24 ± 0.78%	15.89 ± 0.23	53.01	3.37

13k	3-fluoro	13.13 ± 0.26	14.03 ± 0.22	53.01	3.37
13l	4-fluoro	14.54 ± 0.65	14.85 ± 0.37	53.01	3.37
13m	2-cyano	45.39 ± 0.67%	14.89 ± 0.26	76.8	2.80
13n	3-cyano	42.41 ± 0.51%	14.73 ± 0.31	76.8	2.66
13o	4-cyano	39.40 ± 0.78%	15.58 ± 0.44	76.8	2.66
13p	3-nitro	38.76 ± 0.52%	14.62 ± 0.16	104.82	2.97
18a	Hydrogen	14.75 ± 0.42	16.38 ± 0.37	87.66	2.26
18b	3-methoxy	2.41 ± 0.42	11.34 ± 0.46	96.89	2.34
18c	4-chloro	5.32 ± 0.31	7.13 ± 0.37	87.66	3.23
23a	Hydrogen	1.42 ± 0.24	3.14 ± 0.28	99.69	2.15
23b	5-methoxy	0.96 ± 0.14	1.23 ± 0.23	108.92	2.17
23c	5-chloro	0.84 ± 0.12	1.29 ± 0.22	99.69	3.03
FA[d]	-----------	15.12 ± 0.36%	17.15 ± 0.29%	66.76	1.42
DPZ[e]	-----------	0.06 ± 0.01	2.16 ± 0.19	38.77	4.59

[a] IC_{50}: 50% inhibitory concentration (mean ± SD of two or three independent experiments).

[b] % inhibition at 20 μM concentration of inhibitor

[c] tPSA (topological polar surface area) and cLogP values are calculated using ChemDraw

[d] **FA** (ferulic acid) = negative control

[e] **DPZ** (donepezil) = reference standard

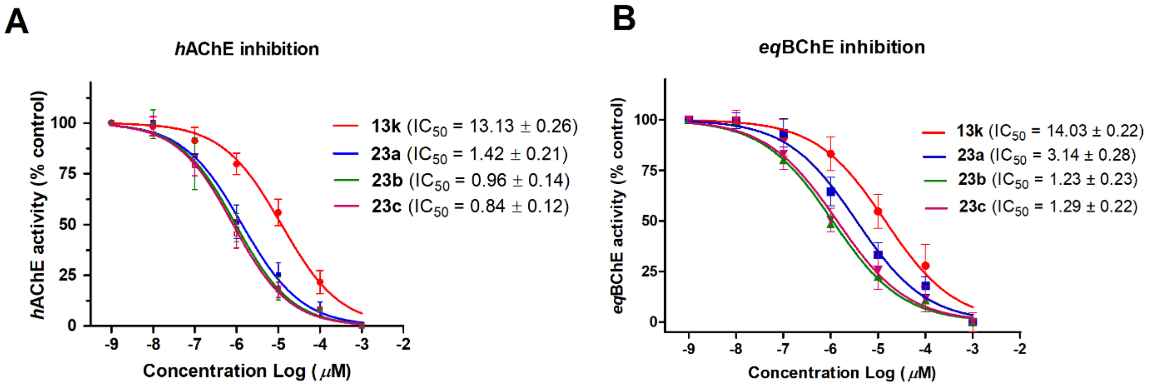

Figure 4.36. ChEs inhibitory activities of selected compounds.

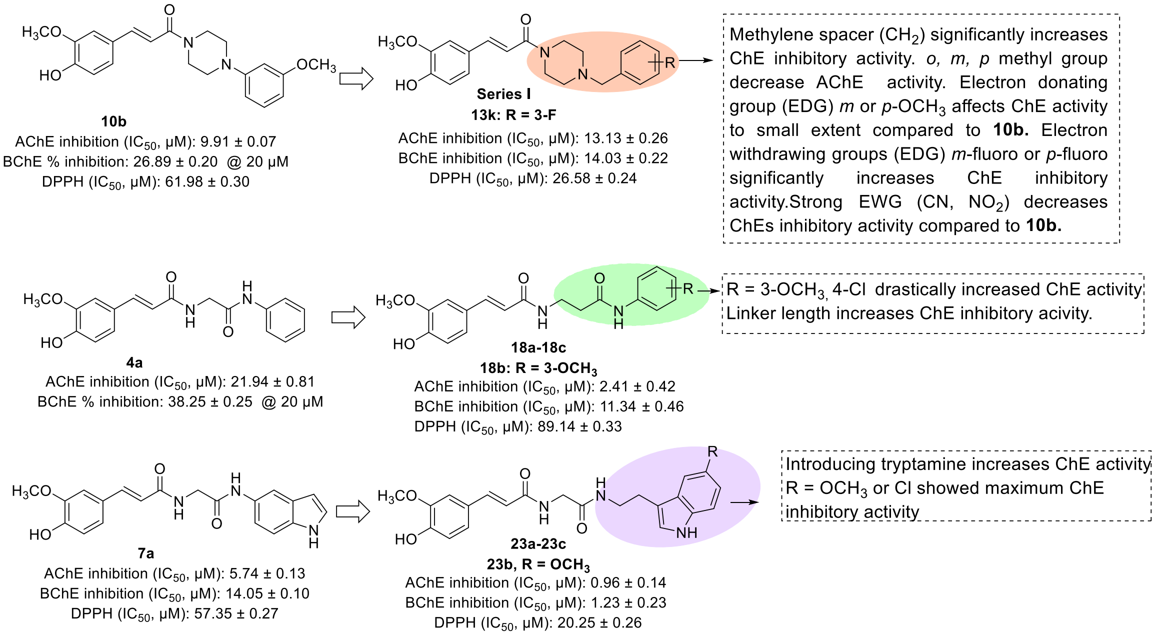

Figure 4.37. A brief summary of structural activity relationship (SAR).

4.3.2.3. Antioxidant activity (DPPH radical scavenging activity)

It is evident from the literature that OS plays a crucial role in the progression of AD. Therefore, inhibition of ChEs along with the ability to reduce oxidative stress would be a more effective approach for the treatment of AD. The antioxidant ability of developed molecules was evaluated by 2,2-Diphenyl-1-(2,4,6-trinitrophenyl) hydrazine (DPPH) assay. To perform DPPH radical scavenging experiment, we have selected thirteen compounds based on ChEs inhibition property. Antioxidant activity is expressed as IC_{50} value, *i.e*, compound concentration required to reduce 50% of the DPPH radical concentration in a solution. All tested compounds exhibited excellent to moderate antioxidant activity with IC_{50} ranging from 20.25 ± 0.26 to 95.59 ± 0.57 μM (Table 4.10). Interestingly, compounds bearing *m*-fluoro (**13k**), and tryptamine (**23a**, **23b**, and **23c**) derivatives showed the maximum radical scavenging activity among all the tested molecules in this series (IC_{50}, **13k** = 26.58 ± 0.24, **23a** = 29.05 ± 0.32, **23b** = 20.25 ± 0.26, and **23c** = 23.57 ± 0.29 μM, respectively) (Figure 4.38). Overall, our study strongly suggested a significant improvement in the antioxidant property in the newly developed molecules compared to earlier reported phenylpiperazine derivatives **10b**, IC_{50} = 61.98 ± 0.30 μM), and the parent molecule **FA** (IC_{50} = 58.31 ± 0.61).

Table 4.10. Antioxidant activity (DPPH assay) of **13a**, **13c**, **13f**, **13h**, **13i**, **13k-13l**, **18a-18c**, **23a-23c** and **FA**.

	Antioxidant activity (DPPH assay)	
Compound	% Radical scavenging [a]	IC_{50} (μM) [b]
13a	38.41 ± 1.09	31.34 ± 0.45
13c	26.32 ± 1.13	65.98 ± 0.39
13f	30.49 ± 1.13	46.43 ± 0.29
13h	23.13 ± 1.17	61.52 ± 0.42
13i	32.41 ± 0.92	62.40 ± 0.45
13k	40.23 ± 1.21	26.58 ± 0.24
13l	23.14 ± 0.98	51.93 ± 0.41
18a	10.62 ± 0.96	95.59 ± 0.57
18b	21.28 ± 1.01	89.43 ± 0.46
18c	18.66 ± 0.96	84.21 ± 0.66
23a	38.55 ± 0.92	29.05 ± 0.32
23b	51.92 ± 1.12	20.25 ± 0.26
23c	47.27 ± 1.11	23.57 ± 0.29
FA[c]	33.11 ± 1.30	58.31 ± 0.61

[a] All the values were obtained at a compound concentration of 20 μM,

% Radical scavenging; means ± SD of three independent experiments

[b] IC_{50}: 50% inhibitory concentration (means ± SD of three independent experiments)

[c] **FA** (ferulic acid) = negative control

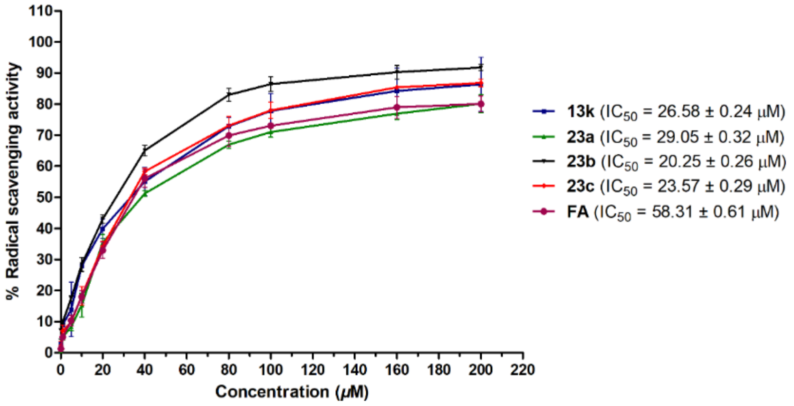

Figure 4.38. DPPH scavenging activity by **13k**, **23a**, **23b**, **23c,** and **FA**. Results are the means ± SD for the three-experiment performed in triplicate.

4.3.2.4. Kinetic studies of ChEs inhibition

Based on the enzymes inhibition and antioxidant properties, the mechanism of ChEs inhibition (AChE & BChE) was evaluated for two selected lead compounds (**13k** and **23b**) on both human AChE *(h*AChE) and *equine* BChE (*eq*BChE). In this experiment, the substrate [S] *vs* velocity [V] curves were plotted upon addition of different concentrations of **13k** (26, 13, and 6.5 μM), and **23b** (5.0, 1.0 and 0.5 μM) in the presence of five different substrate [S] concentrations (ATCI or BTCI) (0.5, 1.0, 1.5, 2.0 and 2.5 μM for *h*AChE, and 5, 10, 15, 20, and 25 μM for *eq*BChE) to probe into the mechanism of ChEs inhibition. As depicted in figure 4.39 by Lineweaver−Burk reciprocal plots, **13k** and **23b** displayed a mixed type of inhibition on both *h*AChE and *eq*BChE (Figure 4.39).

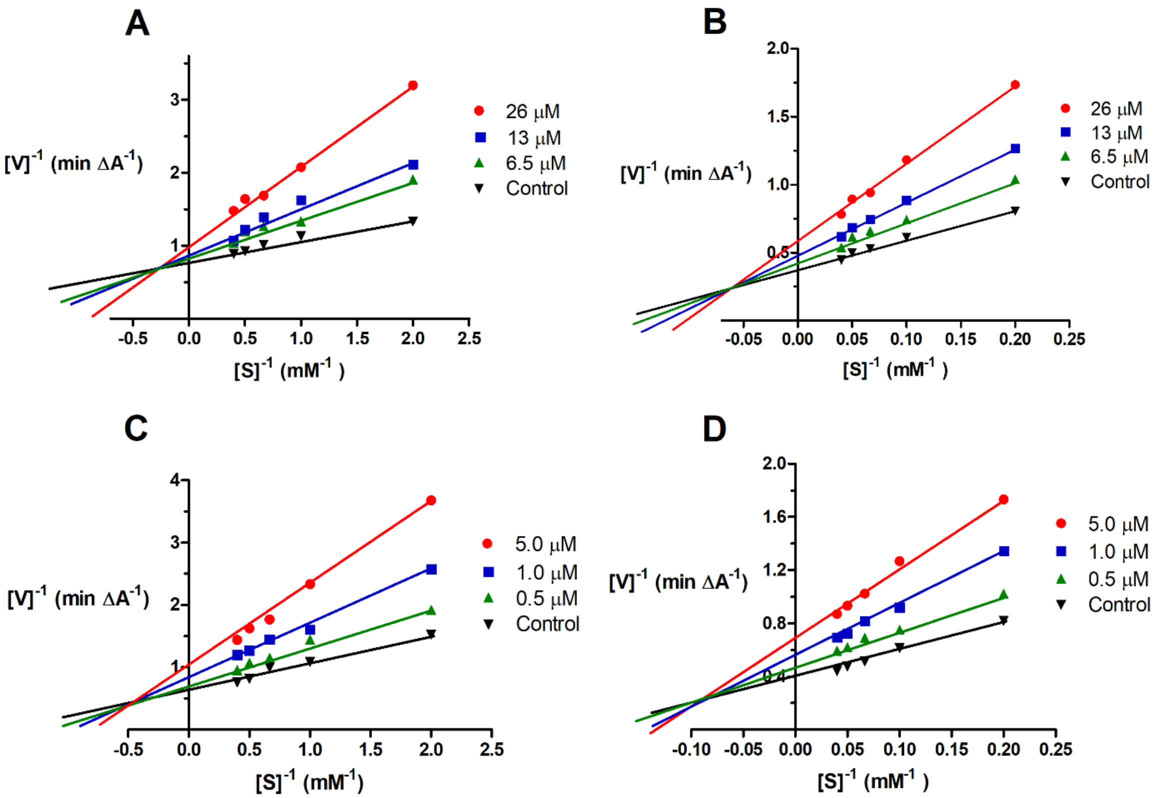

Figure 4.39. Lineweaver-Burk double reciprocal plot showing the mechanism of *h*AChE and *eq*BChE inhibition over a range of substrate concentrations; [**A** and **B**] *h*AChE and *eq*BChE inhibition by **13k**; [**C** and **D**] *h*AChE and *eq*BChE inhibition by **23b**. The experimental data are the means ± SD of two independent experiments.

4.3.2.5. Peripheral anionic site (PAS) binding study

Based on the potent cholinergic inhibitory (AChE, IC$_{50}$, **13k** = 13.13 ± 0.26, **23b** = 0.96 ± 0.14, and **23c** = 0.84 ± 0.12 μM, respectively) and antioxidant properties (IC$_{50}$, **13k** = 26.58 ± 0.24, **23b** = 20.25 ± 0.26, and **23c** = 23.57 ± 0.29, respectively) the lead molecules **13k**, **23b** and **23c** were selected for PAS binding studies. Next, to determine whether **13k, 23b,** and **23c** have an affinity towards the PAS of AChE, a propidium iodide-based competitive displacement assay was performed following our publications [112]. Propidium iodide is a commonly used PAS-specific ligand of AChE, which binds selectively at its PAS, which can be measured through the enhancement of the fluorescence intensity (~10-fold). In the presence of a ligand able to bind strongly with the PAS site, a decrease in the propidium iodide fluorescence is expected due to displacement of propidium from the PAS. **DPZ**, which is known to bind to the enzyme's PAS site, served as a reference drug in this assay. To perform this experiment, we incubated AChE (5.0 U/mL) with different concentrations of compounds (5, 10, 20, and 50 μM) followed by propidium iodide and recorded the change in fluorescence using Synergy^{TM} HT, Bio-Tek Instruments, Inc. The results mentioned in table 4.11 indicated that **23b** and **23c** were found to be more efficient in displacing propidium iodide in a concentration-dependent manner compared to DPZ. While **13k** represented weak propidium iodide displacement compared to DPZ and other tested compounds (Table 4.11**)**.

Table 4.11. Displacement of propidium iodide from the peripheral anionic site of AChE by **13k**, **23b**, **23c,** and DPZ at the indicated concentrations.

Compd.	5 μM	10 μM	20 μM	50 μM
13k	3.34 ± 0.12	8.32 ± 0.16	14.83 ± 0.24	20.32 ± 0.31
23b	10.36 ± 0.23	13.96 ± 0.29	21.85 ± 0.39	33.14 ± 0.43
23c	8.39 ± 0.26	13.64 ± 0.32	19.79 ± 0.42	30.17 ± 0.45
DPZ	8.87 ± 0.18	11.65 ± 0.22	19.10 ± 0.34	27.96 ± 0.41

^{a}Results are the mean ± SD for two independent experiments. Displacement is presented in %.

4.3.2.6. Molecular modeling studies

4.3.2.6.1. Molecular docking

Molecular docking of selected ligands **13a**, **13c**, **13g-13h**, **13j-13k**, **13m**, **18a**, **18c**, and **23b-** were performed against the AChE and BChE using the Glide in extra precision (XP) mode. Before performing the final docking study of all above-mentioned molecules, the co-crystallized ligands *i.e.* DPZ and tacrine were redocked to the crystal structures of AChE and BChE, respectively. The RMSD difference between the redocked and co-crystallized ligands were found to be less than 1Å. Table 4.12 and table 4.13 depict the docking score, XP GScore, glide gscore, glide emodel, and important interactions (hydrogen bonds, hydrophobic interactions, and salt bridges) between residues of proteins (*i.e.* AChE and BChE) and small molecules.

Table 4.12. Docking results (in terms of docking score, XP GScore, glide gscore, and glide emodel) and interaction details between the *h*AChE and different **FA** analogs.

Ligand	Docking score	XP GScore	glide gscore	glide emodel	Interactions			
					Hydrogen Bonds	π-π Interaction	π-Cation Interaction	Salt Bridge
13a	-11.7	-12.50	-12.50	-75.919	Ser203	Phe338, His447	Trp286	
13c	-14.075	-14.88	-14.88	-82.7		Trp86, Trp286	Trp86, Tyr337, Phe338	
13g	-10.669	-11.47	-11.47	-77.57	Phe295	Trp286, Tyr337	Tyr337, Tyr341	Asp74
13h	-12.476	-13.28	-13.28	-83.90	Tyr133, Gly120			Asp74
13j	-13.203	-14.01	-14.01	-81.085		Trp86	Trp86, Tyr337	
13k	-14.924	-15.73	-15.73	-78.454	Arg296	Trp86	Trp86	
13m	-11.537	-12.34	-12.34	-83.712	Phe295	Trp286	Tyr341	Asp74
18a	-8.91	-9.087	-9.087	-83.023	Phe295, Tyr124	Trp286, Tyr337, His447		
18c	-9.125	-9.301	-9.301	-83.96	Tyr124	Trp86, Trp286		
23b	-9.93	-10.10	-10.10	-107.676	His447, Phe295, Tyr124	Trp86, Trp286		
23c	-10.241	-10.41	-10.41	-107.715	Asp74, Tyr124, Phe295	Trp286		
DPZ	-17.209	-17.20	-17.20	-88.707	Phe295	Trp286, Trp86	Trp86, Tyr337, Phe338	

Table 4.13. Docking results (in terms of docking score, XP GScore, glide gscore, and glide emodel) and interaction details between the BChE and different **FA** analogs.

Ligand	Docking score	XP GScore	glide gscore	glide emodel	Interactions			
					Hydrogen Bonds	π-π Interaction	π-Cation Interaction	Salt Bridge

13a	-7.241	-7.652	-7.652	-64.519	Glu197	Trp82		
13c	-7.833	-8.243	-8.243	-70.212	Tyr128, Glu197	Trp82		
13g	-7.212	-7.622	-7.622	-65.298	Glu115, Tyr128	Trp82		
13h	-7.392	-7.803	-7.803	-67.349	Glu115, Tyr128			
13j	-7.538	-7.949	-7.949	-67.667	Glu197	Trp82		
13k	-7.63	-8.04	-8.04	-71.31	Gly115, Tyr128, Gly197	Trp82		
13m	-6.544	-7.353	-7.353	-73.072	Glu197,	Trp82, Tr332	Tyr332	Asp70
18a	-7.563	-7.74	-7.74	-72.726	Tyr128	Trp231		
18c	-7.781	-7.958	-7.958	-77.148	His438	Trp82		
23b	-7.817	-7.989	-7.989	-90.314	Glu197	Trp82		
23c	-9.053	-9.226	-9.226	-89.187	Glu197	Trp82		
Tacrine	-7.032	-7.032	-7.032	-48.53	His438, Ser79	Trp82	Trp82	

4.3.2.6.2. Interaction of ligands 13k and 23b with *h*AChE

Figures 4.40A and 4.40B show the 2D interaction diagram of **13k** and **23b** with *h*AChE. During the MD simulations, it was observed that phenyl ring of **FA** moiety of ligand **13k** interacts with Trp286 *via* π- π stacking interaction, and this residue is considered as one of the principal components of PAS. This hydrophobic interaction between the Trp286 and **13k** was consistent and maintained during the entire simulation run, as shown in protein-ligand contact (Figure 4.41B). Similarly, the carbonyl moiety of **FA** exhibited water-mediated hydrogen bond with Asp74 (PAS residue) and Thr75. In short, the whole **FA** fragment present in the ligand **13k** mainly interacts with residues belonging to PAS of AChE *via* hydrophobic and hydrogen bond interactions. Similarly, the piperazine ring of **13k** interacts with one of the important CAS residues Tyr337 via both direct and water-mediated hydrogen bonds. This stable interaction of piperazine ring with CAS was maintained during the whole period of simulation *via* the water bridges and direct hydrogen bond (Figure 4.41 and Figure 4.42**)**. Apart from this, one more important interaction between the 3-fluorobenzylpiperazine fragment and CAS residue Trp86 was observed, which was maintained for 74% of the total simulation time. Further, the residue Tyr341 makes π-cation interaction while the Phe 338 makes π- π stacking with the 3-Fluorobenzylpiperazine moiety, respectively.

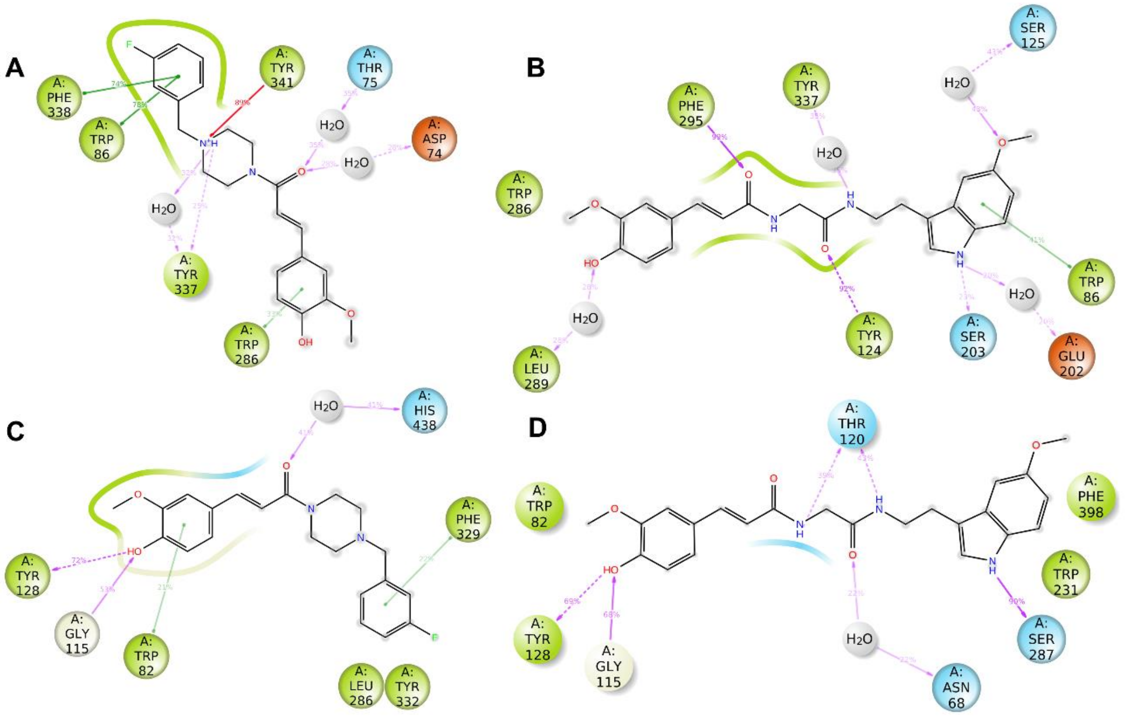

Figure 4.40. 2D interaction diagram of (**A**) **13k** with AChE; (**B**) **23b** with AChE, (**C**) **13k** with BChE, and (**D**) **23b** with BChE. Whereas green, red, and violet-colored arrows represent the π-π stacking, π-cation interactions, and hydrogen bonds, respectively.

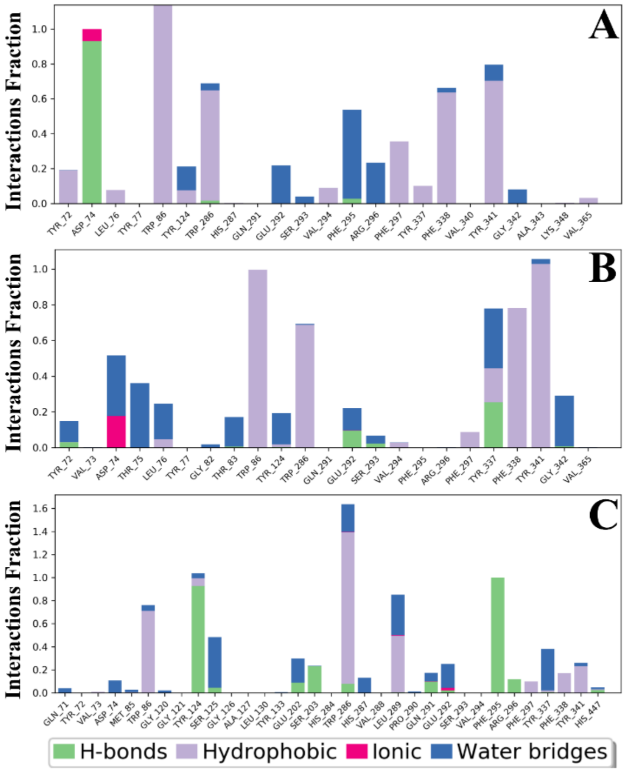

Figure 4.41. Interactions fraction histogram of (**A**) **DPZ**, (**B**) **13k** and (**C**) **23b** with *h*AChE.

The ligand **23b** is mainly composed of 3 moieties i.e. 5-methoxytryptamine, **FA** and a linker glycinamide (Figure 4.40B). The 5-methoxytryptamine moiety of ligand **23b** mainly interacts with three CAS residues Trp86 (π- π stacking), Glu202 and Tyr337 (via water-mediated hydrogen bond). The protein-ligand contact timeline representation depicts that all of these interactions *i.e.* hydrogen bond and hydrophobic interactions between the tryptamine moiety and CAS residues, were maintained throughout the simulation (Figure 4.41 and Figure 4.42). Further, a stable and consistent water-mediated hydrogen bond between the 5-Methoxytryptamine of **23b** and Ser125 was also observed. One important and interesting interaction (hydrogen bond) between the carbonyl oxygen of **FA** moiety and residue Phe295 was also observed. Further, the protein-ligand contact histogram and timeline (Figure 4.41 and Figure 4.42) depicts that the interaction between Phe295 and **FA** moiety was one of the most consistent and stable interactions since it was maintained for 99% of the total simulation time.

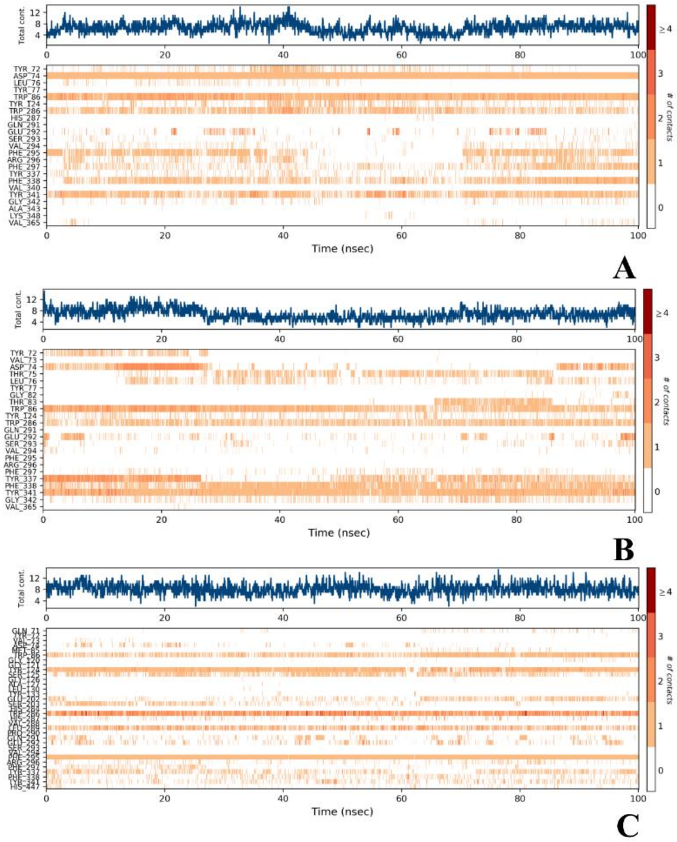

Figure 4.42. Top panel shows the total number of specific contacts the *h*AChE makes with the (**A**) DPZ, (**B**) **13k** and (**C**) **23b** over the course of the trajectory and the bottom panel shows the interaction of particular residues with the ligands in each trajectory frame.

4.3.2.6.3. Interaction of ligands 13k and 23b to *h*BChE

Figures 4.40C and 4.40D show the 2D interaction diagrams of **13k** and **23b** with *h*BChE. The **FA** moiety interacts with residues Tyr128, Gly115 via a hydrogen bond, and Trp82 interacts via π- π stacking interaction. Further, the π-π stacking interaction between the fluorobenzyl moiety of **13k** and Phe329 was also observed. The tryptamine moiety of **23b** makes a stable hydrogen bond with Ser287, and this interaction was maintained for 90% of the total simulation time. Similarly, the **FA** moiety of makes a couple of hydrogen bonds with residues Gly115 and Tyr128. The protein-ligand contact histogram and timeline (Figure 4.43 and Figure 4.44) show that the interaction between the **FA** moiety of **23b** and Tyr128 was found to be stable and maintained during the entire simulation run. Apart from these interactions, the linker present between tryptamine and **FA** makes two hydrogen bonds with Thr120, and one water-mediated hydrogen bond with Asn68.

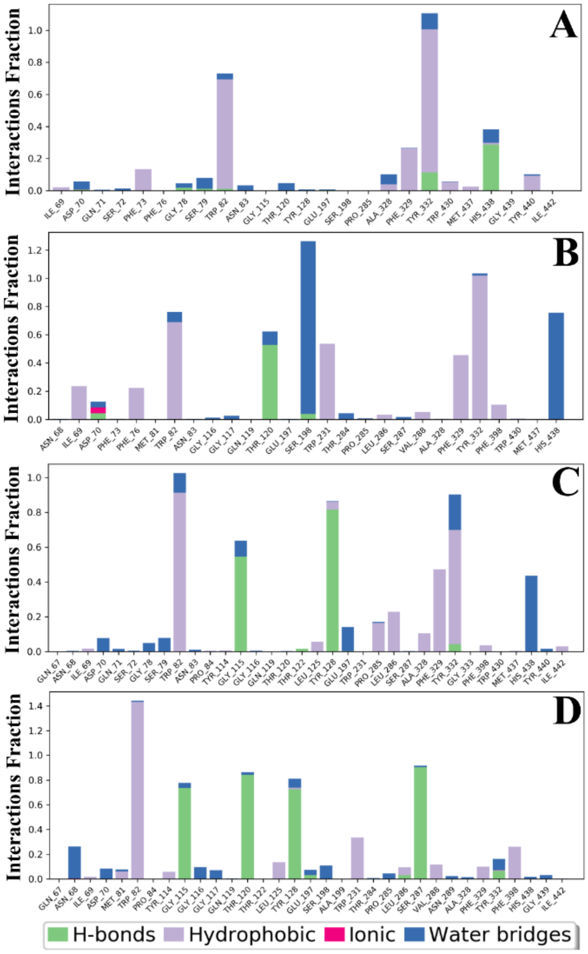

Figure 4.43. Interactions fraction histogram of (**A**) Tacrine, (**B**) DPZ (**C**) **13k** and (**D**) **23b** with *h*BChE.

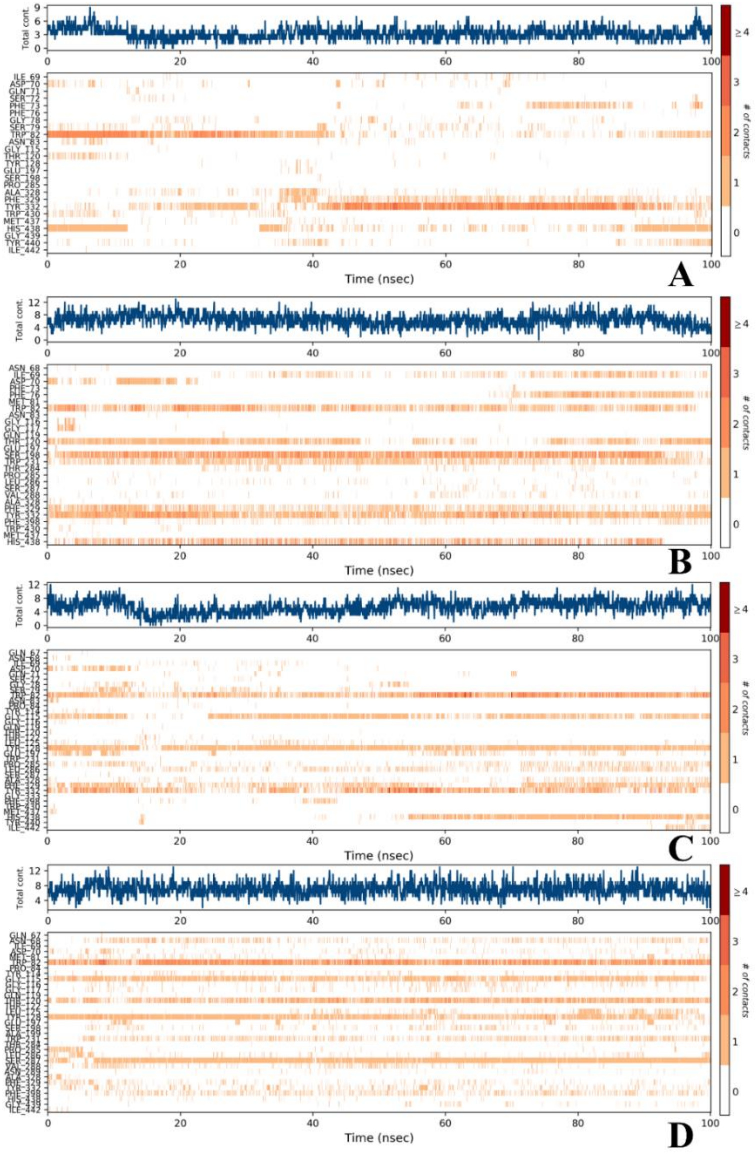

Figure 4.44. The top panel shows the total number of specific contacts the *h*BChE makes with the (**A**) Tacrine, (**B**) DPZ (**C**) **13k**, and (**D**) **23b** over the course of the trajectory and the bottom panel shows the interaction of particular residues with the ligands in each trajectory frame.

4.3.2.6.4. Analysis of binding free energy

The binding free energy of complexes AChE_**13k**, AChE_**23b**, BChE_**13k** and BChE_**23b** were calculated from the last 25 ns of trajectory at an interval of 50 ps using Prime/MM-GBSA (molecular mechanics/generalized born surface area) method. Figure 4.45 shows the fluctuation in binding free energy of all four complexes with respect to simulation time. Table 4.14 shows the average binding free energy and its different contributing terms for all four complexes. The figure 4.45A shows that the binding free energy of complex *h*AChE_**23b** fluctuates at higher values as compared to *h*AChE_**13k**. The average binding free energy of *h*AChE_**13k** complex in the last 25 ns was found to be -58.46 kcal/mol, while the complex *h*AChE_**23b** was found to have -82.17 kcal/mol.

Similarly, the BChE_**23b** complex was found to fluctuate with higher binding free energy as compared to BChE_**13k** complex (Figure 4.45B**)**. The average binding free energy of BChE_**13k** complex was found to be -61.63 kcal/mol, while BChE_**23b** complex has higher binding energy -75.03 kcal/mol. The calculated binding free energy for both ligands **13k** and **23b** with AChE and BChE are in line with observed experimental results.

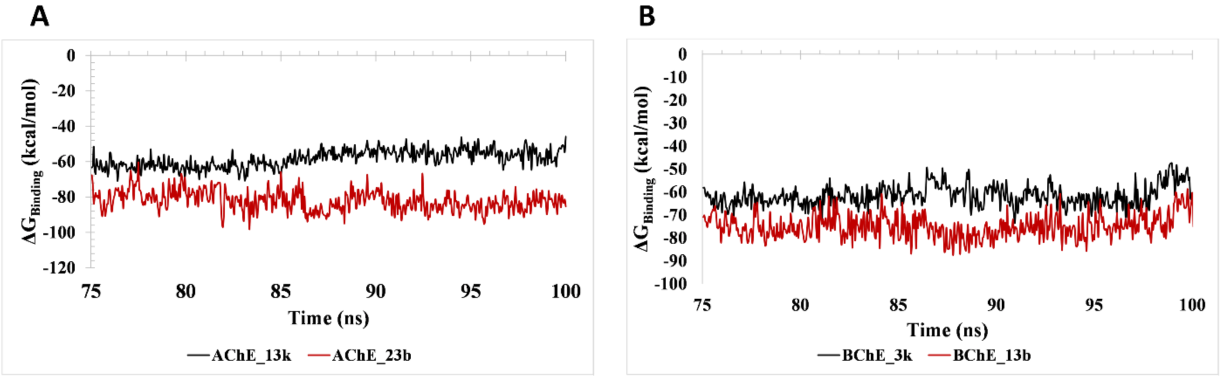

Figure 4.45. Binding free energy of (**A**) AChE with ligands **13k** and **23b,** and (**B**) BChE with ligands **13k** and **23b**, with respect to simulation time calculated using the MM-GBSA method from the last 25 ns of MD simulations.

Table 4.14. The average ΔG_{bind} and its different contributing energy terms for **13k** and **23b** against *h*AChE and *h*BChE calculated from MD trajectories (last 25) ns.

Complex	Avg. ΔG_{bind} Coulomb^{a}	Avg. ΔG_{bind} Covalent^{b}	Avg. ΔG_{bind} Hbond^{c}	Avg. ΔG_{bind} Lipo^{d}	Avg. ΔG_{bind} Packing^{e}	Avg. ΔG_{bind} solv GB^{f}	Avg. ΔG_{bind} vdW^{g}	ΔG_{bind} Total^{h}
AChE_1**3k**	-22.50	1.81	-0.27	-27.69	-3.78	42.70	-48.73	-58.46
AChE_**23b**	-29.76	1.11	-1.44	-31.27	-7.39	46.70	-60.12	-82.17
BChE_1**3k**	-12.35	2.81	-1.10	-31.02	-3.15	33.17	-50.01	-61.63
BChE_**23b**	-27.70	6.48	-2.21	-26.81	-2.02	38.12	-60.89	-75.03

[a]Coulomb energy, [b]Covalent binding energy, [c]Hydrogen bonding correction, [d]Lipophilic energy, [e]Pi-pi packing correction, [f]Generalized Born electrostatic solvation energy, [g]Van der Waals energy and [h]Total binding free energy.

4.3.2.6.5. Analysis of structural stability, compactness, and solvent accessibility surface area

The structural stability of AChE and BChE and its complex with different ligands can be explained by analyzing the RMSD and radius of gyration (Rg) (Figure 4.46 and Figure 4.47**)**. The changes in RMSD values with respect to simulation time for all complexes (AChE/BChE) suggest that the simulation is converged. It was observed that the RMSD fluctuates at lower values in the presence of almost all ligands with respect to simulation time for both AChE and BChE (Figure 4.46**)**. This indicates that the binding of ligands stabilizes the AChE/BChE. The decrease in RMSD and Rg values of AChE with respect to simulation time in the presence of ligands **13k**, **23b**, and DPZ are more significant as compared to BChE. It is very little or no considerable changes in Rg value of BChE in presence of all four ligands as compared to apo form of the enzyme (Figure 4.47**)**.

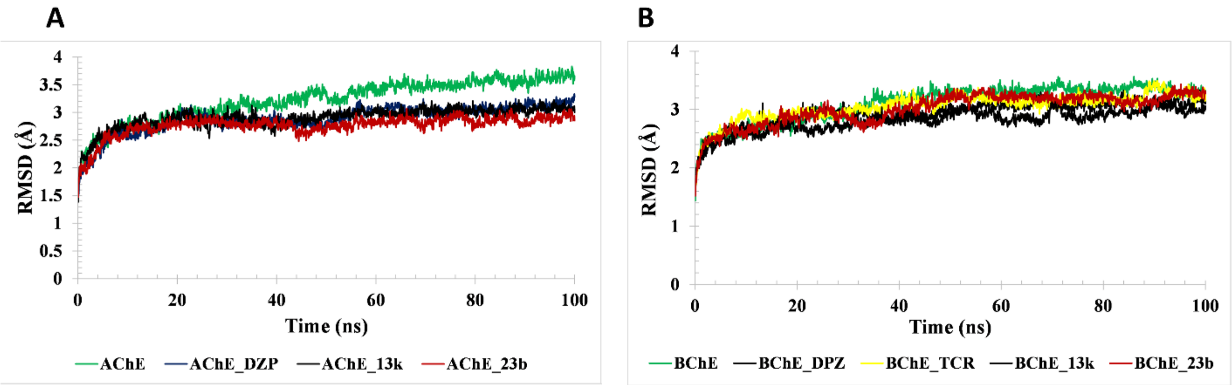

Figure 4.46. Backbone RMSD plot for (**A**) apo-AChE in comparison with AChE-DPZ, AChE-**13k**, and AChE-**23b**, (**B**) apo-BChE in comparison with BChE-DPZ, BChE-Tacrine, BChE-**13k**, and BChE-**23b** with respect to simulation time.

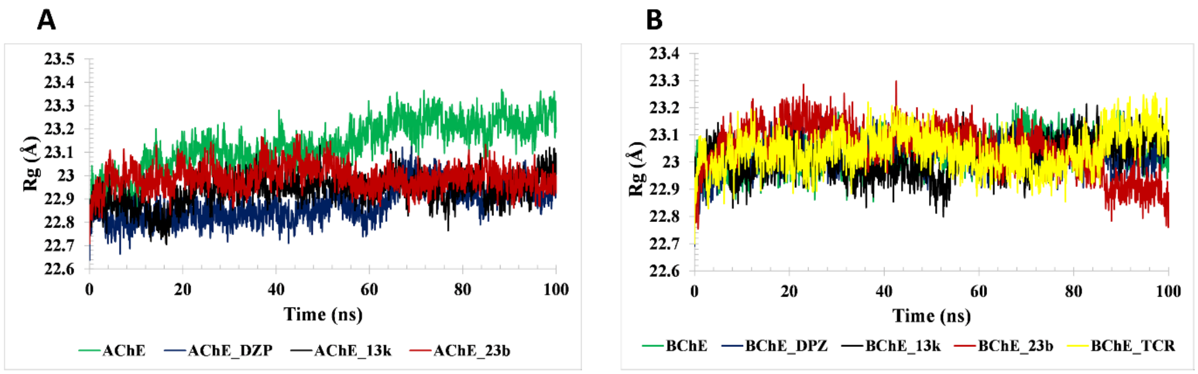

Figure 4.47. The radius of gyration plot for (**A**) apo-AChE in comparison with AChE-DPZ, AChE-**13k**, and AChE-**23b**, and (**B**) apo-BChE in comparison with BChE-DPZ, BChE-Tacrine, BChE-**13k**, and BChE-**23b** with respect to simulation time.

The percentage change in SASA of the residues presents 20 Å away from the binding pocket was also calculated for both AChE and BChE in the presence and absence of ligands. It was found that there was a considerable decrease in SASA of active site residues of both AChE and BChE in the presence of **13k** and **23b**. The figure 4.48A and figure 4.48B represents the percentage decrease in SASA of AChE and BChE in the presence of **13k**, **23b,** and crystallized ligands (DPZ and Tacrine) with respect to simulation time.

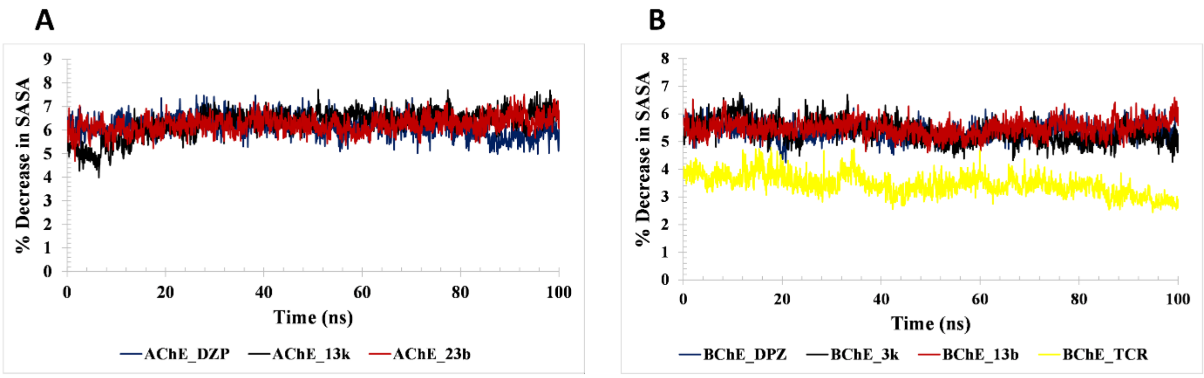

Figure 4.48. Percentage decrease in SASA of active site residues (20 Å away from the bound ligand) of (**A**) AChE and (**B**) BChE with respect to simulation time in the presence of different ligands.

The overall analysis shows that there was an average 6% decrease in SASA values of AChE in the presence of **13k**, **23b,** and DPZ. Similarly, an average of around 5% decrease in SASA value was observed for BChE in the presence of **13k**, **23b,** and DPZ, while it was only a 3.45% decrease in presence of co-crystallized ligand tacrine (Figure 4.48 (B), and Figure 4.49A-4.49C).

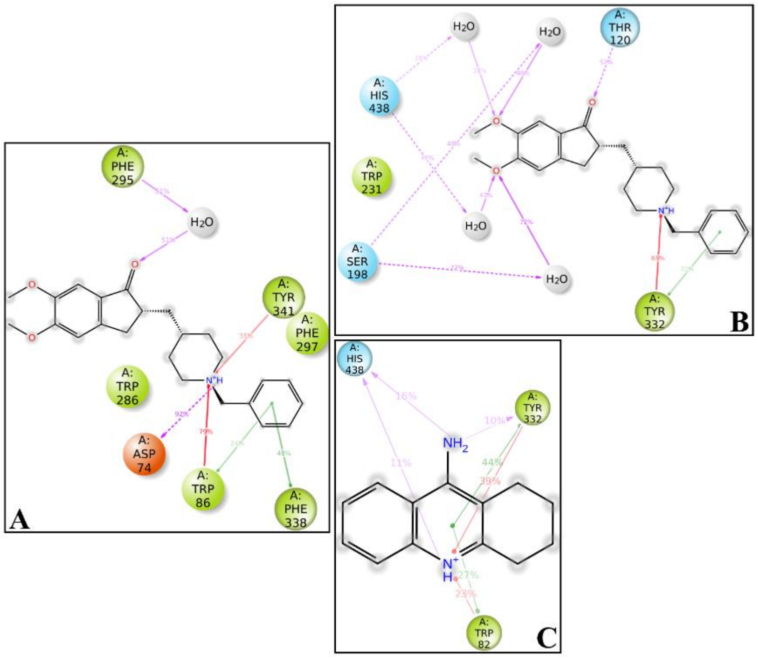

Figure 4.49. 2D interaction diagram of (**A**) *h*AChE with DPZ (**B**) *h*BChE with DPZ and (C) *h*BChE with Tacrine, where green, red and violet colored arrows represent the π-πstacking, π-cation interactions and hydrogen bonds, respectively.

4.3.2.7. Calculation of physicochemical parameters

Physicochemical properties such as molecular weight (MW), the number of hydrogen acceptors (HBA), the number of hydrogen donors (HBD), the number of rotatable bonds (RB), and logBB were estimated using admetSAR software [179]. The values obtained were in range with the reported limits of CNS+ drugs (Table 4.15). Overall, these results collectively suggest that all the developed compounds follow Lipinski's rule and exhibited significant brain permeability.

Table 4.15. Calculation of physicochemical parameters of the developed molecules.

Compd.	**MW**^{a}	**cLogP**^{b}	**tPSA**^{c}	**HBA**^{d}	**HBD**^{e}	**RB**^{f}	**BBB**^{g}	**Caco-2**
13a	352.43	3.22	53.01	4	1	5	+	+
13b	366.46	3.72	53.01	4	1	5	+	+
13c	366.46	3.72	53.01	4	1	5	+	+
13d	366.46	3.72	53.01	4	1	5	+	+

13e	382.46	3.14	62.24	5	1	6	+	+
13f	382.46	3.14	62.24	5	1	6	+	+
13g	386.88	3.94	53.01	4	1	5	+	+
13h	386.88	3.94	53.01	4	1	5	+	+
13i	386.88	3.94	53.01	4	1	5	+	+
13j	370.42	3.37	53.01	4	1	5	+	+
13k	370.42	3.37	53.01	4	1	5	+	+
13l	370.42	3.37	53.01	4	1	5	+	+
13m	377.44	2.80	76.8	5	1	5	+	+
13n	377.44	2.80	76.8	5	1	5	+	+
13o	377.44	2.80	76.8	5	1	5	+	+
13p	397.43	2.97	104.82	6	1	6	+	+
18a	340.38	2.26	87.66	4	3	7	+	-
18b	370.41	2.34	96.89	4	3	7	+	-
18c	374.82	3.23	87.66	5	3	8	+	-
23a	393.44	2.15	99.69	4	4	8	+	-
23b	423.47	2.17	108.92	5	4	9	+	-
23c	427.89	3.03	99.69	4	4	8	+	-
FA	194.19	1.42	66.76	3	2	3	+	-
DPZ	379.50	4.59	38.77	4	0	6	+	+

All values were calculated using online software admetSAR. ^{a}MW: molecular weight; ^{b}cLogP: partition coefficient; ^{c}tPSA: topological polar surface area; ^{d}HBA: number of H-bond acceptor atoms; ^{e}HBD: number of H-bond donor atoms; ^{f}RB: rotatable bonds; ^{g}BBB: blood brain barrier permeability.

4.3.2.8. Metal chelation study

Literature studies revealed that the dyshomeostasis of biometals, especially iron (Fe) and copper (Cu), plays a crucial role in AD's pathogenesis. The extracellular accumulation of bio-metals induces the OS and leads to highly toxic reactive free radical species. Therefore, AD treatment through modulation of these bio-metals has been considered a viable therapeutic approach. Therefore, based on the AChE/BChE inhibition and antioxidant property, **23b** was selected for the iron-chelating ability. The metal chelating ability of representative compound **23b** was performed by UV-vis spectroscopy assay, and the results are presented in figure 4.50. To perform this experiment, an equimolar concentration of **23b** and $FeCl_3.6H_2O$ were mixed together, and a complexation study was conducted. As depicted in figure 4.50, **23b** in the presence of $FeCl_3.6H_2O$ presented different absorption spectra compared to absorption of the compound **23b** alone. The absorption spectra of the solution at pH 7.4 exhibited higher intensity at 511 nm than the spectra at lower pH values (4.2). This is a clear indication of a complex formation between **23b** and Fe^{3+} ion. The binding stoichiometry of **23b** with Fe^{3+} was examined by measuring the changes in absorption at 511 nm when **23b** was titrated with $FeCl_3.6H_2O$ in a different molar ratio, as depicted in figure 4.50C. Finally, we plotted the absorbance value against the mole fraction of **23b**. We observed a breakage point in the plot where the mole fraction of **23b** was 50%, which reveals 1:1 binding of **23b** toward Fe^{3+} (Figure 4.50D).

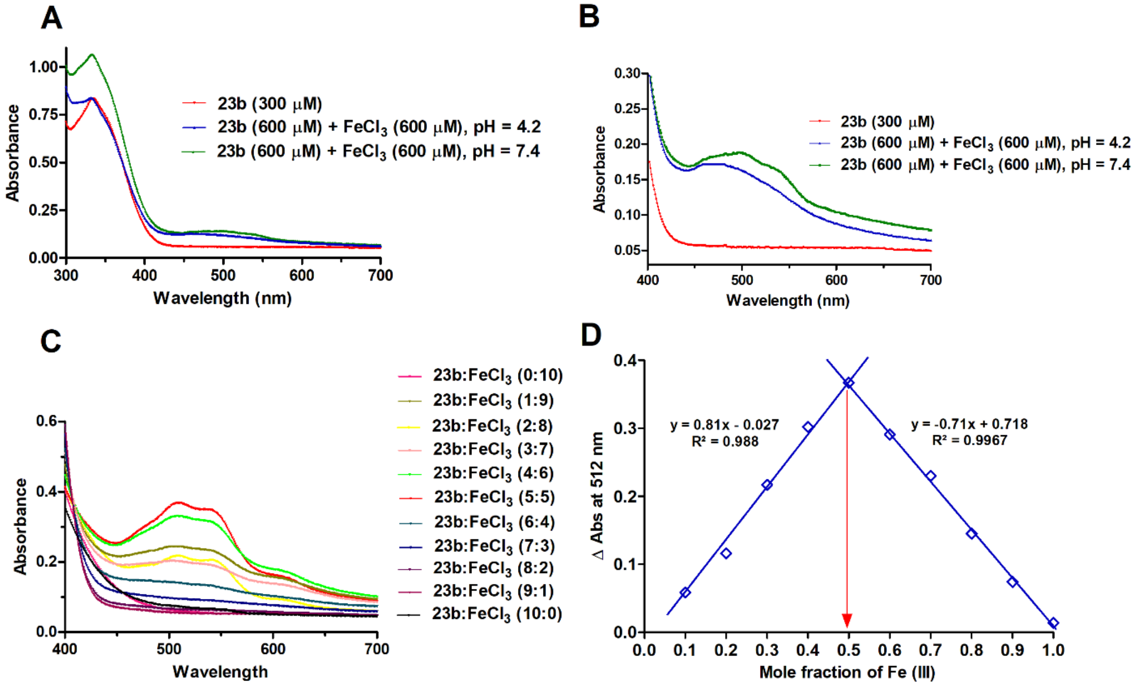

Figure 4.50. (**A**) UV absorbance spectra of **23b** (300 μM) alone or in the presence of $FeCl_3$ (600 μM) in methanol (pH 4.2 and 7.4) from 300-700 nM. (**B**) UV absorbance spectra of **23b** (300 μM) alone or in the presence of $FeCl_3$ (1 equiv.) in methanol (pH 4.2 and 7.4) from 400-700 nm (*dd*-transition). (**C**) Metal ion titration of **23b** with $FeCl_3$ in different molar ratio (0-10 ratio). (**D**) Job's

plot for determining the stoichiometry of the complex between **23b** and $FeCl_3$. Results are the means for the experiment performed in duplicate.

4.3.2.9. ***In-vitro*** evaluation of cytotoxicity of compound 23b

Cytotoxicity studies are one of the important criteria in the drug development process. The cytotoxicity studies were carried out prior to the *in-vivo* studies. The lead identified molecule **23b** with potent AChE/BChE inhibitory activity, antioxidant, and metal chelation properties was selected to evaluate the potential for cytotoxic effect on N2a cells, a widely used neuronal cell line. The cells were treated with different concentrations of **23b** for 24 hrs, and cell death was quantitatively analyzed by 3-(4,5-dimethylthiazol-2-yl)-2,5-diphenyltetrazolium bromide (MTT) assay. The dose-dependent effect of **23b** (Figure 4.51**)** on cell viability indicated that the compound had no significant effect on cell viability and was well tolerated by neuronal cells at all the tested concentrations.

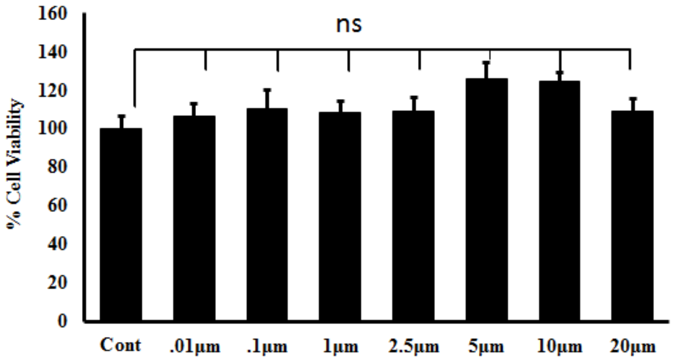

Figure 4.51. Effect of **23b** on cell viability. Cells were treated with different concentrations of **23b** (0.01, 0.1, 1, 2.5, 5, 10 and 20 μM) for 24 hours. Cell viability in % was analyzed using MTT assay. Data presented as mean ± SE of three independent experiments done in three replicates.

4.3.2.10. Neuroprotective effect on H_2O_2 induced N2a cell injury

In our previous experiment, **23b** has shown promising free radical quenching ability in 2,2-diphenyl-1-picrylhydrazyl (DPPH) assay, which strongly suggested that **23b** is a potent antioxidant with a potency approximately three times ($IC_{50} = 20.25 \pm 0.26$ μM) compared to parent natural compound **FA** ($IC_{50} = 58.18 \pm 0.52\ \mu M$). In our present study, we carried out experiments to evaluate the effect of treatment with **23b** on protecting the neuronal N2a cells from toxicity induced by H_2O_2. In this experiment, we have employed various concentrations (100 to 800 μM) of the pro-oxidant H_2O_2 (widely acceptable neurotoxin) and found that 600 μM of H_2O_2 can cause ~50 % cell death in N2a cells (Figure 4.52). After optimizing the concentration of H_2O_2 and the incubation time, we next assessed the neuroprotection ability of **23b**, to alter cytotoxicity after co-incubating with H_2O_2. The cells were incubated with various concentrations (1, 2.5, 5, 10, and 20 μM) of **23b** for 24 h followed by co-treatment with 600 μM H_2O_2 for an additional 24 h. As shown in figure 4.52 the MTT assay indicated that **23b** could significantly (*$P < 0.05$, ***$P < 0.001$) protect N2a cells from H_2O_2 induced neurotoxicity. The significant protection conferred by **23b** was exhibited in all tested concentration ranges of 1−20 μM of the drugs. However, no significant difference was observed at a concentration above 2.5 μM. This suggests that 2.5 μM of **23b** is able to negate the oxidative stress caused by 600 μM of H_2O_2 in cells.

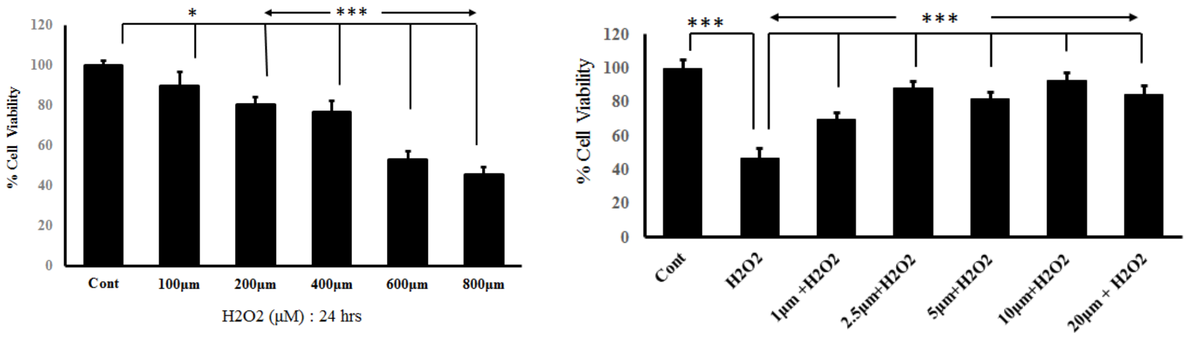

Figure 4.52. Effect of **23b** against H_2O_2 mediated cell death. (**A**) Cell death induced by H_2O_2 at 100, 200, 400, 600, and 800 µM for 24 h. (**B**) Neuroprotective effect of treatment **23b** against H_2O_2 mediated N2a cell death. Cells were pre-incubated with **23b** at 1, 2.5, 5, 10, or 20 µM for 24 h and then further co-incubated with 600 µM H_2O_2 for another 24 h. Cell death was assessed by MTT assay. The data represent the mean of three independent experiments. *$P < 0.05$, ***$P < 0.001$, compared with untreated control cells only, data expressed as mean ± SEM.

4.3.2.11. *In-vitro* blood-brain barrier permeation assay

Blood-brain barrier (BBB) permeability is the necessary requirement for developing anti-AD drugs. A parallel artificial membrane permeation assay of the blood−brain barrier (PAMPA-BBB) was performed to check the probable BBB permeability of **13k** and **23b**. For this experiment, firstly, we compared three commercial drugs' permeability with their reported values to validate the experiment (Table 4.16). The P_e values of **13k** and **23b** are listed in table 4.16. According to the limit established by Di *et al.* for BBB permeation, we concluded that compounds with $P_e > 4.0$ could be considered to show high BBB permeability (CNS+), compounds with $P_e < 2$ is expected to show low BBB permeability (CNS-). Analysis of the developed compounds in the PAMPA-BBB assay revealed P_e>4.0 for **13k,** and **23b** showed (Table 4.16), demonstrating that compound ability to cross the BBB and can potentially reach their biological targets within the brain.

Table 4.16. Permeability in the PAMPA-BBB assay for **13k**, **23b**, DPZ, testosterone, corticosterone, and hydrocortisone with their predictive BBB penetration.

S.No.	compound	P_e (exp)^a	Reference value^b	Prediction^c
1.	Testosterone	18.91 ± 1.42	17.0	CNS (+)
2.	Corticosterone	10.19 ± 1.39	5.1	CNS (+)
3.	Hydrocortisone	2.94 ± 1.12	1.9	CNS (-)
4.	**13k**	9.57 ± 0.27	------	CNS (+)
5.	**23b**	8.51 ± 0.31	------	CNS (+)
6.	DPZ	15.57 ± 0.18	------	CNS (+)

^{a}Data are the mean ± SD of two independent experiments. ^{b} Reference values were taken from Di Li *et al.*[171] ^{c}CNS (+), $P_e > 4.0$, high permeability; CNS (-), Pe < 2.0, low permeability; CNS (±), $4.0 > P_e > 2.0$, uncertain permeability. ^{d}DPZ (donepezil) reference AChE inhibitor. The data represent the mean ± SD of two independent experiments.

4.3.2.12. 23b ameliorates scopolamine-induced cognitive impairment in the Morris water maze test

The improvement in cognitive impairment is the essential criteria for the successful development of anti-AD agents. The MWM permits the accurate and reproducible study of reference memory, cognitive maps, place learning, spatial learning, and working memory. MWM is highly sensitive in the assessment of damage to the hippocampus. The robustness and reliability make this paradigm as one of the "gold standards" of behavioral neuroscience. Therefore, in the present study, we evaluated the *in-vivo* efficacy of **23b** in the MWM experiment to assess mice's spatial working memory (Figure 4.53A and 4.53B). The respective drug doses of **23b** (5 and 10 mg/kg) orally and DPZ (0.5 mg/kg) were administered intraperitoneally 30 min prior to the administration of scopolamine (1 mg/kg, *i.p.*) to the respective group of animals for consecutively fourteen days. During the last 5 days of the treatment period, ELTs were recorded for the animals of different experimental groups. The escape latencies time for the first four days of the training period are shown in figure 4.54. Scopolamine treatment caused cognitive impairment, and an increase in the escape latency time compared to the control group was observed, which indicated the development of amnesia in the mice (Figure 4.55A). While DPZ significantly reduced ELT from 33.58 ± 3.54 to 16.37 ± 5.11 s, $p < 0.01$, Figure 4.55A) as compared to the scopolamine-treated group. Treatment with **23b** at a dose of 10 mg/kg significantly reduced ELT from 50.11 ± 5.91 to 32.28 ± 6.37 s (Figure 4.55A, $p < 0.05$), which indicates significant attenuation in the memory impairment. Additionally, the recorded tracks of the mice from all groups clearly further confirmed these results (Figure 4.55C). These outcomes collectively suggested that the animals could retain the previous memory in the MWM experiment. The mechanism of the spontaneous alternation stimulation in the scopolamine model is likely mediated by the anti- AChE activity of the compound **23b**, suggesting that **23b** is a potent cholinesterase inhibitor that can cross the blood-brain barrier effectively. The results suggested that the molecule is orally active and significant changes in the compound treated group in comparison with the control and the scopolamine group.

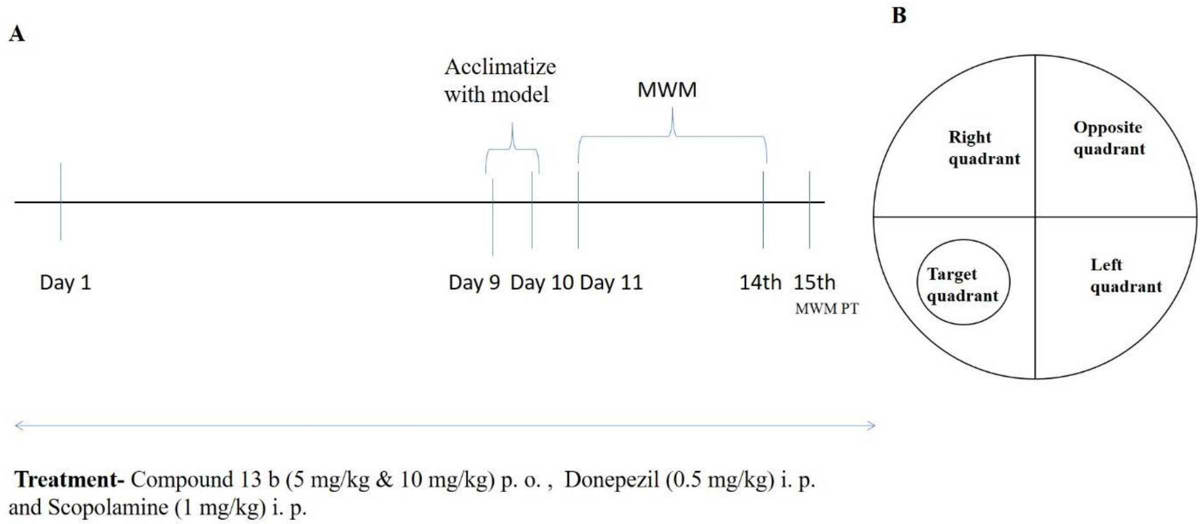

Figure 4.53. (**A**) Schematic schedule of experimental design to study the anti-amnestic effect of compound **23b**. (**B**) Outline of the Morris water maze model experiment. I.P.; intraperitoneal, P.O; per os (orally), MWM PT-probe trial of Morris water maze test; MWM- Morris water maze.

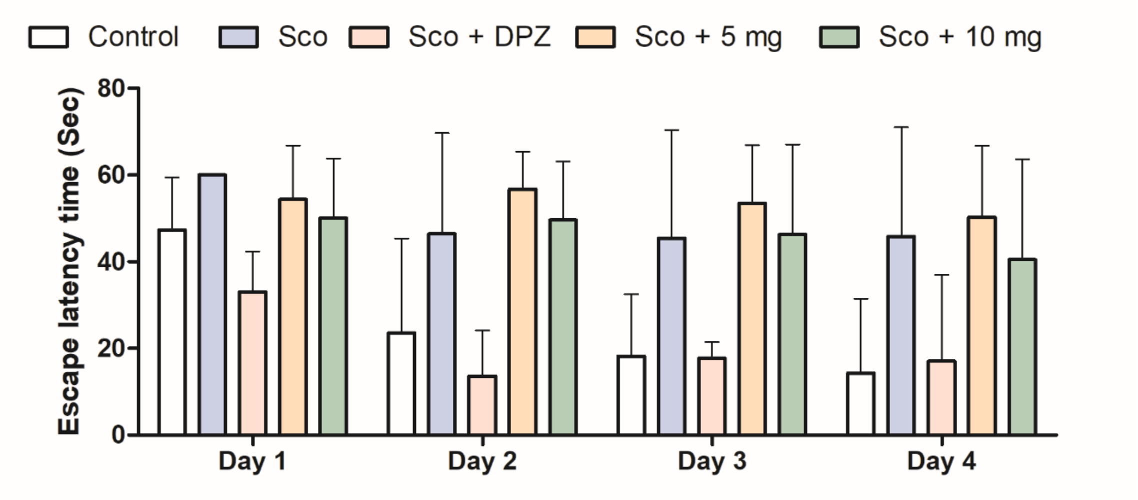

Figure 4.54. Escape latency time (in second) from Day 1 to Day 4.

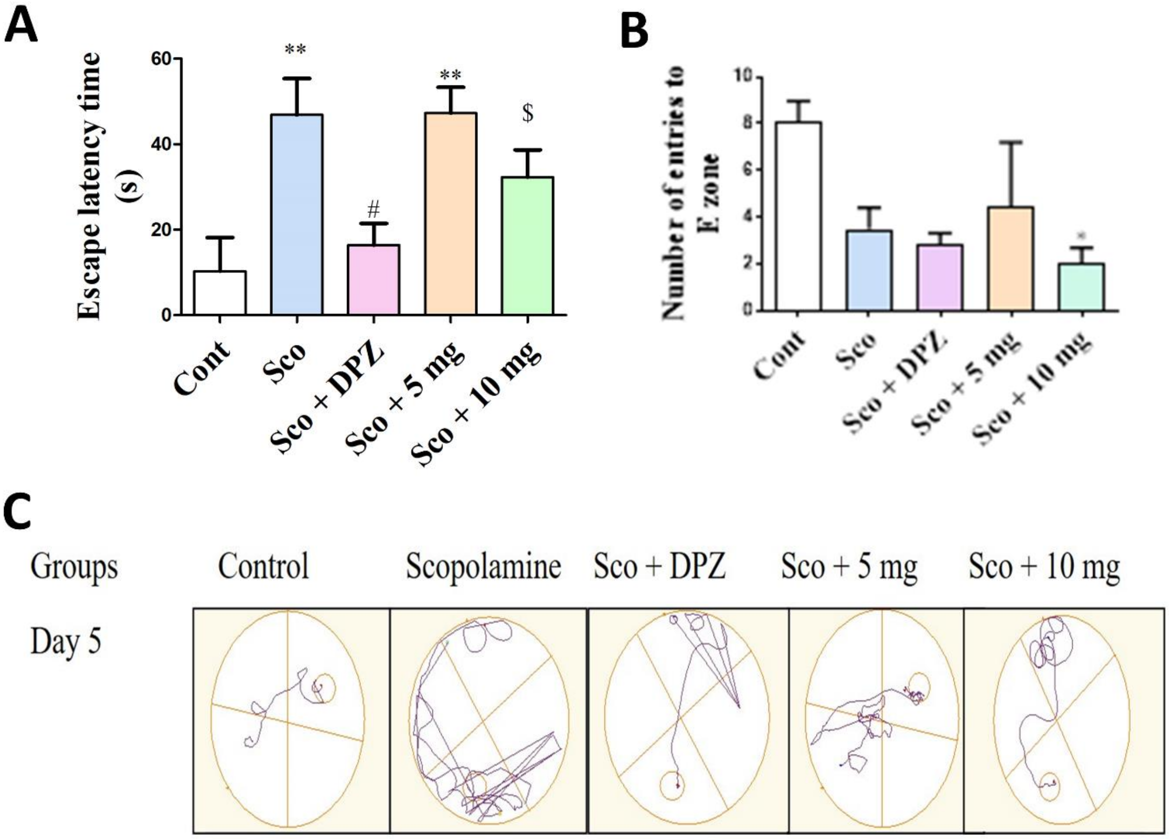

Figure 4.55. Scopolamine-induced memory deficit mice model study. (**A**) Escape latency time on Day 5 (**B**) No. of entries in E zone. (**C**) Track diagram on Day 5. Data are expressed as mean ± SEM (n = 7). ** $p < 0.01$, * $p < 0.05$ versus corresponding value in the control in Fig A and vs scopolamine in Fig. B, #$p < 0.01$ vs. scopolamine (Sco) group, \$$p < 0.05$ vs Sco group. (Data recorded through Any Maze software). (Data recorded through Any Maze software).